Study on Effect of Energy Fluxes in relation to the Movement and Intensity of Tropical Cyclones in the Bay of Bengal

M. Sc. Thesis

BY

KANIZ FATEMA

DEPARTMENT OF PHYSICS

KHULNA UNIVERSITY OF ENGINEERING & TECHNOLOGY

KHULNA-9203, BANGLADESH

FEBUARY-2017

Study on Effect of Energy Fluxes in relation to the Movement and Intensity of Tropical Cyclones in the Bay of Bengal

M. Sc. Thesis

BY

KANIZ FATEMA

ROLL NO: 1555556

SESSION: JULY-2015

A thesis submitted in partial fulfillment of the requirements for the degree of Master of Science in the Department of Physics, Khulna University of Engineering & Technology, Khulna-9203

DEPARTMENT OF PHYSICS

KHULNA UNIVERSITY OF ENGINEERING & TECHNOLOGY
KHULNA-9203, BANGLADESH

FEBUARY-2017

DECLARATION

This is to certify that the thesis work entitled "***Study on Effect of Energy Fluxes in relation to the Movement and Intensity of Tropical Cyclones in the Bay of Bengal"*** has been carried out by KANIZ FATEMA in the Department of Physics, Khulna University of Engineering & Technology, Khulna, Bangladesh. The above thesis work or any part of this work has not been submitted anywhere for the award of any degree or diploma.

Signature of Supervisor

(Professor Dr. Md. Mahbub Alam)

Signature of Candidate

KANIZ FATEMA

DEDICATED TO
MY HUSBAND, FAMILY and FRIENDS

Acknowledgements

With my great manner it is a pleasure for me to express my deepest sense of gratitude and indebtedness to my reverend supervisor Dr. Md. Mahbub Alam, Professor, Department of Physics, Khulna University of Engineering & Technology, Khulna, for his kind guidance and supervision and for his constant encouragement throughout the research work. His inspiration and friendly cooperation has accelerated my works.

I am indebted to Professor Dr. Shibendra Shekher Sikder, Head, Department of Physics, Khulna University of Engineering & Technology for his strong support in various ways during the entire period of my study in this department. I express my heartfelt gratitude and thanks to Professor Dr. Md. Abdullah Elias Akhter and Professor Dr. Jolly Sultana Department of Physics, Khulna University of Engineering & Technology. Many thanks for their inspiration and advices from the beginning of my study. I gratefully acknowledge Mr. Md. Kamrul Hasan Reza, Mr. Sujit Kumar Shil, Md. Alamgir Hossain, Assistant Professors and Mr. Sumon Halder, Sumon Deb Nath, Lecturer, Department of Physics, KUET for their cooperation regarding writing the thesis.

My personal thankful greetings are to my good friends and well wishers for their help and cooperation. There are numerous people who could not be mentioned individually but their interesting discussions have prompted much thought on various aspects, I would also like to thank them. I would like to express my heart full thanks to my parents, husband, sisters and nearest relatives for their inspiration, encouragement and multifaceted supports to carry out this thesis work.

I am grateful to the KUET authority for approval of the project in the 33rd meeting of CASR, agenda no. 33/5/10 and providing me the relevant facilities to complete this research work. The Author is grateful to National Centre for Atmospheric Research (NCAR), USA for making the WRF (WRF-ARW) model available to modeling community. The Grid Analysis and Display System software (GrADS) was used for analytical purposes and displaying Figs. India Meteorological Department (IMD) is acknowledging for providing necessary data over India. Finally, I want to express my gratitude to almighty Creator for his mercy.

Kaniz Fatema

CONTENTS

List of Figures

List of Table

Nomenclature

ARW	:	Advanced Research WRF
AFWA	:	Air force weather agency
AOGCMs	:	Atmospheric-oceanic general circulation models
BMJ	:	Betts-Miller-Janjic
CP	:	Cumulus Parameterization
CAPE	:	Convective available potential energy
CIN	:	Convective inhibition
CSLP	:	Central sea level pressure
DLHF	:	Downward long wave heat flux
DSHF	:	Downward shortwave heat flux
DSSF	:	Down-welling surface shortwave radiation flux
FE	:	Ferrier scheme
FNL	:	Final Reanalysis
FSL	:	The Forecast Systems Laboratory
FAA	:	The Federal Aviation Administration
GrADS	:	Grid Analysis and Display System
GD	:	Grell-Devenyi ensemble
HFX	:	upward heat flux
IMD	:	India Meteorological Department
ITCZ	:	Inter-tropical convergence zone
JTWC	:	Join typhoon warning center
KF	:	Kain-Fritch
KS	:	Kessler
LH	:	latent heat flux
MP	:	Microphysics
MRF	:	The Medium Range Forecast
NCAR	:	National Center for Atmospheric Research
NWP	:	Numerical weather prediction
NCEP	:	National Center for Environmental Prediction
OLR	:	Outgoing long wave radiation
PBL	:	Planetary Boundary Layer
QFX	:	moisture heat flux
RRTM	:	Rapid radiative transfer model
SST	:	Sea surface temperature
TC	:	Tropical Cyclones
TH	:	Thomson
UTC	:	Universal Time Co-ordinate
VSCS	:	Very severe cyclonic storm
WSM6	:	WRF Single-moment 6-class
YSU	:	Yonsei University Scheme

ABSTRACT

Comprehensive sensitivity analysis on physical parameterization schemes of Weather Research and Forecasting model (WRF v3.2.1) have been carried out for the effects of energy fluxes on the prediction of track and intensity of Tropical Cyclone Roanu, Hudhud and Mala those formed in the Bay of Bengal and crossed Bangladesh, Visakhapatnam of India and Myanmar coast during May 2016, October 2014 and April 2006 respectively. The initial and boundary conditions of tropical cyclone (TC) are drawn from the global operational analysis and forecast products of National Center for Environmental Prediction (NCEP-GFS) available for the public at 1°×1° resolution. The model was run by using Kessler (KS), Lin *et al*. (Lin), WSM3-class simple ice, Ferrier (FE), WSM6-class graupel and Thomson (TH) graupel microphysics (MP) schemes coupling with different cumulus parameterization (CP) schemes and different initial conditions. Kain-Fritsch (KF) and Betts-Miller-Janjic (BMJ) schemes have been used to study the effects of energy fluxes on the track of TC. The model domain consists of 8-24°N and 77-96°E and has 12 km horizontal resolution with 28 vertical sigma levels. The model was run for 96 and 72-h using initial conditions at 0000 UTC of 18 and 19 May 2016 for TC Roanu, 120 and 96-h using initial conditions of 0000 UTC of 8 and 9 October 2014 for TC Hudhud, and 120 and 96-h using initial conditions of 0000 UTC of 26 and 27 April 2006 for TC Mala. To examine the effect of energy fluxes on the movement of TC we have considered five different regions inside the model domain. The regions are R1 (22-26°N & 87-93°E), R2 (18-22°N & 81-85°E), R3 (14-18°N & 78-84°E), R4 (12-22°N & 85-94°E) and R5 (17-22°N & 94-97°E). In this research the Convective available potential energy (CAPE), Convective inhibition (CIN), Downward long wave heat flux (DLHF), Downward shortwave heat flux (DSHF), Ground heat flux (GHF), latent heat flux (LH), moisture heat flux (QFX), Outgoing long wave radiation (OLR), and upward heat flux (HFX) have been analyzed in R1, R2, R3, R4 and R5 to observe the impact of these parameters for the movement of TC. The vertically integrated space averaged CAPE, CIN, DLHF, DSHF, OLR have found to decrease continuously for all MPs in combination with KF and BMJ schemes in a region where TC moves. These parameters have decreased for TC Roanu in R1, for TC Mala in R5 and TC Hudhud in R2. The QFX and LH have been increased in a region where TC moves.

Chapter I

Introduction

Tropical cyclones are known to cause enormous damage and destruction in the coastal regions. The cyclones formed over the Bay of Bengal generally move in the northwest direction and crossed Bangladesh, Myanmar and eastern coast of India. Cyclones generally form over the Bay of Bengal in the pre-monsoon and post-monsoon seasons have the tendency to cross Bangladesh coast. The prediction of these cyclones is very difficult tropical cyclone is very much essential. Tropical cyclone is a system of rapidly rotating storm with low pressure center, strong winds and spiral arrangement that produce significant natural disaster. For this reason, coastal regions are particularly vulnerable to damage from a tropical cyclone as compared to inland regions. Heavy rain, significant flooding inland, and storm surges can produce extensive coastal flooding up to 40 km from the coastline. The importance of the sea surface temperature (SST) in the genesis and intensity of tropical cyclones has become well established. It is known that tropical cyclones usually develop over waters in which the SST is 26°C or higher.

Emanuel (1983) and Chang (1979) confirm the sensitivity of storm intensity to the SST in the vicinity of storms. Tuleya and Kurihara (1982) observed the SST anomalies induced by the tropical cyclone have been observed to vary from 1-6°C. Black (1983) showed the cooling of the sea surface results in reduction in the total heat flux into the atmosphere leading to a decrease in storm intensity. Chang and Anthes (1978) represented a negative feedback mechanism and a number of numerical simulation studies have been made in order to understand and to evaluate various aspects of the ocean response to moving tropical cyclones.

Raju *et al.,* (2011) have shown that the error in landfall time and intensity are decreasing with the delayed initial condition, suggesting that the model forecast is more dependable on the initial and boundary conditions. Davis and Bosart (2002) considered the effects of cumulus Parameterization on tropical storm track. They found that the Betts-Miller-Janjic (BMJ) and Grell schemes produced more westward deviated track than Kain-Fritsch (KF) scheme. The KF scheme tended to intensify the storm too rapidly but produced the best track compared with observations. Andreas *et al*., (1979) have shown that the surface latent flux is high around the cyclone, where strong winds blow near the surface. The large latent heat flux (>

100 W m^{-2}) is maintained around the southern coast of Japan. The magnitude of the sea-surface sensible heat flux is much smaller than that of the latent heat flux. Fairal *et al.,*(1996) computing bulk flux algorithm sensible and latent heat fluxes is based on the interfacial fluxes scale differently than spray fluxes with wind speed,

Decosmo *et al*., (1996) showed no obvious dependence of the exchange coefficients of sensible and latent heat with wind speed up to roughly 20ms^{-1}. Decosmo and Andreas (2002) showed that the lack of wind speed dependence of the bulk moisture and sensible heat transfer. coefficients does not imply the absence of spray effects at these wind speeds; rather, they conclude that the HEXOS data showed that spray contributes up to 40% of the total latent heat flux at wind speeds as low as 15–18ms^{-1}. The standard error is much smaller than the mean mixing ratio although the error in the upward surface latent heat flux is large. Tropical cyclones derive the energy as latent heat from surface evaporation of warm ocean water, and, tend to diminish over land. Mountainous terrain changes the circulation, and alters the deep convection that releases the latent energy, changing the intensity and track of the tropical cyclone.

The model simulation, by using direct numerical simulations of turbulent Couette flow coupled with Lagrangian point particles to investigate the changes inertial particles induce in momentum flux by altering near-surface turbulent motions, the presence of a dispersed phase such as sea spray may, at sufficiently high concentrations, change the turbulent flux of momentum. The momentum carried by the dispersed phase becomes a significant fraction of the total momentum flux to the surface, compensating for losses in the turbulent flux. The total flux of momentum that is nearly unchanged despite an observed reduction in the turbulent flux. In practice, this implies that eddy flux measurements of the turbulent flux taken in regions of high spray concentration may underestimate the total flux of momentum. The presence of spray is seen to decrease the flux of one of these quantities at the expense of the other, and this depends strongly on atmospheric stability.

Tao *et al.,* (1990) Showed that the dominant microphysical processes were quite different between the convective and stratiform regions and between the mature and decaying stages. Willoughby and Lord *et al*., (1984) studied the impact of cloud microphysics on tropical cyclone structure and intensity using 2D axi-symmetric non-hydrostatic model. Their results show that the ice-phase microphysical scheme can produce a lower mean sea level pressure (MSLP) than the case without the ice-phase. Fovell and Su (2007) simulate Hurricane Rita (2005) and compared the effects of Kessler, Lin *et al*., and WSM3 microphysics (MP)

schemes, coupled with the effects of KF, Grell-Devenyi ensemble (GD), and BMJ cumulus parameterization schemes. The hurricane Rita's track was simulated best when the WSM3 scheme was paired with BMJ convection. The worst simulated track was when Kessler was paired with KF convection, which produced a weaker storm that tracked well west of the actual storm. Rosenfeld *et al.,* (2007) noted in their simulations that the suppression of warm rain through the addition of large amounts of aerosols will cause the tropical cyclone to divert eastward. Zhu and Zhang (2006) informed that the hurricane track was not sensitive to cloud microphysical processes except for very weak storms. Bianco *et al.,* (2011) considered the heat, moisture, and momentum flux contributions from spray within a one-dimensional surface layer model and find enhancements of sensible and latent heat flux at sufficiently high wind speeds.

Sobel and Camargo (2005) have found that TCs spread out a wide area at low outgoing long wave radiation (OLR). Pattanaik and Rama Rao (2009) simulated the characteristic of movement on a very severe cyclone Nargis using WRF-ARW model in the Bay of Bengal and have found that the tropical cyclone move towards the minimum OLR. Evans and Waters (2012) build up a relation between sea surface temperatures (SST) and OLR by using atmospheric-oceanic general circulation models (AOGCMs). They found that the OLR generally increases with increases SST until a threshold ocean temperature. Choi and Byun (2010) have shown that higher TC passage frequency during the high-Arctic Oscillation (AO) years have a negative OLR. Choi and Moon (2012) have also observed that the TCs occurred in the western region of negative OLR. The OLR field shows a significant negative anomaly in the region over the North Indian Ocean (Yuan and Cao 2013). Camargo *et al.,* (2007) have found that OLR minima at first TC positions and maxima at the position of maximum intensity.

Xu and Wang (2010) Conducted many experiments and have shown that the removal of surface entropy fluxes outside the eyewall reduces the CAPE and suppresses the activity of spiral rainbands. Bogner *et al.,* (1999) showed that CAPE value maximum at larger radii and lower near the eyewall. Smith and Montgomery (2012) have found that CAPE values are generally largest on the first day of observation and its decreased day by day. They also established an idea that CAPE varies inversely with CIN. Colon-Pagan (2009) found that the CAPE value is very low in their ARW model simulation near the center of tropical cyclone. They worked on the Hurricane Jeanne in combination with four microphysics schemes and found that CAPE is associated with conditionally unstable airstreams and around the

prominent feeder bands CAPE is very low. Molinari and Vollaro (2009) using the more than 2000 dropsonde sounding by the NOAA Gulfstream-IV aircraft for observing the changing pattern of CAPE and found that the mean CAPE raises from center to outer region. Fang *et al.,* (2009) perform by the numerical experiment using the non hydrostatic, axisymmetric TC model and suggest that cyclone has increasing trend at first and decreasing trend when it is strengthen. Nolan *et al.,* (2007) study on tropical cyclone using WRF v2.1.2 combination of WSM6 class microphysics and Yonsei University (YSU) scheme which detected temperature effect on CAPE correspond with Coriolis force and showed that CAPE were proportional relation with sea surface temperature (SST).

Pattnaik and Krishnamurti (2007a, b) have shown that the impact of cloud microphysical processes on hurricane intensity and track were investigated by many authors the microphysical parameters have minimal impact on the hurricane track forecast and also suggested that robust impact on the structural characteristics of hurricane eye-wall and its intensity. Wang (2002) demonstrated that the intensification rate and intensity are not sensitive to the cloud microphysical parameterizations. Wang (2001) noted that cloud structures and aerial coverage of and the peak precipitation in the tropical cyclone were quite sensitive to details of the cloud microphysical parameterization in their TCM3 model.

In this research we have been conducted 24 experiments for each of tropical cyclone Roanu (2016), Hudhud (2014) and Mala (2006) that formed in the Bay of Bengal and crossed Bangladesh, the eastern coast of India and Myanmar by using six different (Kessler, Lin et al, WSM3, Ferrier, WSM6 and Thompson) microphysics (MP) schemes in combination with Kain-Fritsch (KF) and Betts-Miller-Janjic (BMJ) cumulus parameterization (CP) schemes considering different initial conditions. We have studied the following parameters to see the effect of these parameters on the track and intensity of tropical cyclones. The parameters are Convective available potential energy (CAPE), Convective inhibition (CIN), Downward long wave heat flux (DLHF), Downward shortwave heat flux (DSHF), Ground heat flux (GHF), latent heat flux (LH), moisture heat flux (QFX), outgoing long wave radiation (OLR), and upward heat flux (HFX). The aim of this research is to investigate the effects of above mentioned parameters for the movements and intensification of tropical cyclones in the Bay of Bengal. It is also our interest to identify the suitable MP and CP schemes to address the above mentioned parameters.

Chapter II

Literature Review

2.1 Tropical Cyclone (TC)

TC is defined as a non-frontal low pressure system of synoptic scale that is developing over warm waters having organized convection and a maximum wind speed of 34 knots (gale force) or greater extending more than half-way around near the centre and persisting for at least six hours. The gale force winds can extend hundreds of kilometers from the cyclone centre. If the sustained winds around the centre reach 118 km/h (gusts in excess 165 km/h), then the system is called a severe tropical cyclone. These are referred to as hurricanes in Atlantic Ocean and typhoons in Pacific Ocean. The circular eye or centre of a TC is an area characterized by light winds and often by clear skies. Eye diameters are typically 40 km but can range from under 10 km to over 100 km. The eye is surrounded by a dense ring of cloud about 16 km high known as the eye wall which marks the belt of strongest winds and heaviest rainfall. In addition to strong winds and rain, TCs are capable of generating high waves, damaging storm surge, and tornadoes. They typically weaken rapidly over land where they are cut off from their primary energy source. For this reason, coastal regions are particularly vulnerable to damage from a TC as compared to inland regions. Heavy rains, however, can cause significant flooding inland, and storm surges can produce extensive coastal flooding up to 40 kilometers from the coastline. Though their effects on human populations are often devastating, TCs can relieve drought conditions. They also carry heat energy away from the tropics and transport it toward temperate latitudes, which may play an important role in modulating regional and global climate.

2.2 Classification of Tropical Cyclone

Cyclonic disturbances in the North Indian Ocean are classified according to their intensity. The following nomenclature is in use:

i. Low: Wind Speed < 31 km/hr.
ii. Well marked low: Wind Speed equals to 31 km/hr.
iii. Depression: Wind Speed ranges from 32 - 48 km/hr.
iv. Deep Depression: Wind Speed ranges from 49 - 62 km/hr.
v. Cyclonic Storm: Wind Speed ranges from 63 - 88 km/hr.
vi. Severe Cyclonic Storm: Wind Speed ranges from 89 - 117 km/hr.
vii. SCS with a core of hurricane intensity: Winds $\geq$ 118km/hr.

2.3 Life Cycle of Tropical Cyclones

The life span of tropical cyclones with full cyclonic intensity averages at about 6 days from the time they form until the time they enter land or recurve into the Temperate Zone. Some storms last only a few hours; a few as long as two weeks. The evolution of the average storm from birth to death has been divided into four stages (Tarakanov, 1982).

i. **Formative Stage:** Tropical storms form only in near pre-existing weather systems. Deepening can be a slow process, requiring days for the organisation of a large area with diffuse winds. It can also produce a well-formed eye within 12 hours. Wind speed usually remains below hurricane force in the formative stage. Unusual fall of pressure over 24 hours by 2 - 3 hPa or more takes place in the center of the vortices concentration.

ii. **Immature Stage:** A large number of formative cyclones die within 24 hours. Others travel long distances as shallow depressions. Wind of cyclonic force forms a tight band around the center. The cloud and rain pattern changes from disorganized squalls to narrow organized bands, spiraling inward. Only a small area is as yet involved, though there may be a large outer envelope. The eye is usually visible but ragged and irregular in shape.

iii. **Mature Stage:** The force of cyclonic winds may blow within a 30 - 50 km radius during immature stage. This radius can increase to over 300 km in mature storms. On an average the mature stage occupies the longest part of the cycle and most often lasts several days. The eye is prominent and circular and the cloud pattern is almost circular and smooth. The surface pressure at the center is no longer falling and the maximum wind speeds no longer increasing. At this stage, heating from convective clouds furnishes the largest amount of energy for cyclone maintenance. Pressure gradient is largest at the surface. Wind speed range is between 128 - 322 km/hr.

iv. **Terminal Stage:** Nearly, all cyclones weaken substantially upon entering land, because they lose the energy source furnished by the underlying ocean surface. The decay is especially rapid where the land is mountainous. Movement of a cyclone over land cuts off the surface energy source and increased the surface friction, especially when the land is mountainous. Some cyclones die out over sea and this event can be related to their moving over a cold ocean current or being invaded by a surface cold air mass behind a cold front or by a cold center at high levels moving over their top.

2.4 Energy and Fluxes of Tropical Cyclone

2.4.1 Convective Available Potential Energy (CAPE)

Convective available potential energy (CAPE), sometimes, simply, available potential energy (APE) is the amount of energy of a parcel of air would have if lifted a certain distance vertically through the atmosphere. CAPE is effectively the positive buoyancy of an air parcel and is an indicator of atmospheric instability, which makes it very valuable in predicting severe weather. It is a form of fluid instability found in thermally stratified atmospheres in which a colder fluid overlies a warmer one. When an air mass is unstable, the element of the air mass that is displaced upwards is accelerated by the pressure difference between the displaced air and the ambient air at the higher altitude to which it was displaced. This usually creates vertically developed clouds from convection, due to the rising motion, which can eventually lead to thunderstorms. It could also be created in other phenomenon, such as a cold front. Even if the air is cooler on the surface, there is still warmer air in the mid-levels that can rise into the upper-levels. However, if there is not enough water vapor present, there is no ability for condensation, thus storms, clouds, and rain will not form.

CAPE exists within the conditionally unstable layer of the troposphere, the free convective level (FCL), where an ascending air parcel is warmer than the ambient air. CAPE is measured in joules per kilogram of air (J/kg). Any value greater than 0 J/kg indicates instability and the possibility of thunderstorms. CAPE is calculated by integrating vertically the local buoyancy of a parcel from the level of free convection (LFC) to the equilibrium level (EL):

$$CAPE = \int_{EL}^{LFC} \left(\frac{T_v - T_{ve}}{T_{ve}} \right) g dz \qquad (1)$$

Where T_v the virtual temperature of the parcel is T_{ve} is the virtual temperature of the environment and g is the gravitational acceleration. On a sounding diagram, CAPE is the positive area above the LFC, the area between the parcel's virtual temperature line and the environmental virtual temperature line where the ascending parcel is warmer than the environment. When a parcel is unstable, it will continue to move vertically, in either direction dependent on whether it receives upward or downward forcing, until it reaches a stable layer. There are multiple types of CAPE, downdraft CAPE (DCAPE), estimates the potential strength of rain and evaporative cooled downdrafts. Other examples are surface based CAPE (SBCAPE), mixed layer or mean layer CAPE (MLCAPE), most unstable or maximum usable CAPE (MUCAPE), and normalized CAPE (NCAPE).

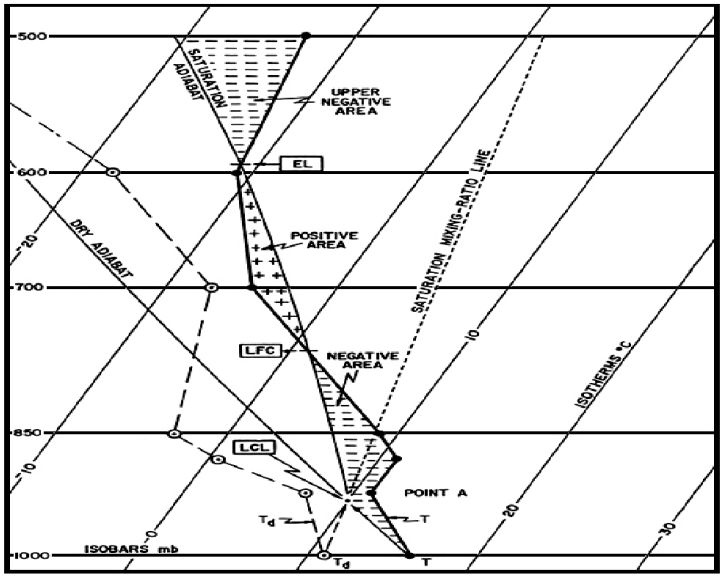

Fig. 2.1: A Skew-T diagram with important features labeled

On the other hand, if adiabatic decrease or increase in density is greater than in the ambient fluid, the upwards or downwards displacement will be met with an additional force in the same direction exerted by the ambient fluid. In these circumstances, small deviations from the initial state will become amplified. This condition is referred to as convective instability. Convective instability is also termed static instability, because the instability does not depend on the existing motion of the air; this contrasts with dynamic instability where instability is dependent on the motion of air and its associated effects such as dynamic lifting.

The amount of and shape of the positive area modulates the speed of updrafts, extreme CAPE can result in explosive thunderstorm development; such rapid development usually occurs when CAPE stored by a capping inversion is released when the "lid" is broken by heating or mechanical lift. The amount of CAPE also modulates how low-level vortices is entrained and then stretched in the updraft, with importance to storm do genesis. The most important CAPE for tornadoes is within the lowest 1 to 3 km, whilst deep layer CAPE and the width of CAPE at mid-levels are important for super cells. Tornado outbreaks tend to occur within high CAPE environments. Large CAPE is required for the production of very large hail, owing to updraft strength, although a rotating updraft may be stronger with less CAPE. Large CAPE also promotes lightning activity.

CAPE for different stability regimes are given as follows:

CAPE < 1000 J/Kg : Instability is weak

CAPE > 1000 < 2500 J/Kg : Moderately unstable

CAPE > 2500 J/Kg : Extremely unstable

2.4.2 Convective Inhibition (CIN)

Convective Inhibition (CIN) is a numerical measure in meteorology that indicates the amount of energy that will prevent an air parcel from rising from the surface to the level of free convection. It is the amount of energy required to overcome the negatively buoyant energy. For the most case, when CIN exists, it covers a layer from the ground to the LFC. The negatively buoyant energy exerted on an air parcel is a result of the air parcel being cooler (denser) than the air which surrounds it, which causes the air parcel to accelerate downward. The layer of air dominated by CIN is warmer and more stable than the layers above or below it.

The situation in which convective inhibition is measured is when layers of warmer air are above a particular region of air. The effect of having warm air above a cooler air parcel is to prevent the cooler air parcel from rising into the atmosphere. This creates a stable region of air. Convective inhibition indicates the amount of energy that will be required to force the cooler packet of air to rise. This energy comes from fronts, heating, moistening, or mesoscale convergence boundaries such as outflow and sea breeze boundaries. Typically, an area with a high convection inhibition number is considered stable and has very little likelihood of developing a thunderstorm. Conceptually, it is the opposite of CAPE. CIN hinders updrafts necessary to produce convective weather, such as thunderstorms. Although, when large amounts of CIN are reduced by heating and moistening during a convective storm, the storm will be more severe than in the case when no CIN was present. (Colby and Frank 1984)

CIN is calculated by measurements recorded electronically by a rawinsonde which measure weather parameters, such as air temperature and pressure. A single value for CIN is calculated from balloon ascent by using the equation:

$$CIN = \int_{Z_{bottom}}^{Z_{top}} \left(\frac{T_{v,parcel} - T_{v,env}}{T_{v,env}} \right) g dz \qquad (2)$$

The Z_{bottom} and Z_{top} limits of integration in the equation represent the bottom and top altitudes of a single CIN layer, is the virtual temperature of the specific parcel and is the virtual temperature of the environment. In many cases, the Z_{bottom} value is the ground and

the Z_{top} value is the LFC. CIN is expressed as a negative energy value. CIN values greater than 200 J/kg are sufficient enough to prevent convection the atmosphere. In fact, CIN is sometimes referred to as negative buoyant energy. It is a good indicator of general stability, and convection tends to be less vigorous with higher values.

CIN	< 100	Potential Instability.
CIN	100 to 200	Marginally stable.
CIN	200 to 300	Moderately stable.
CIN	>400	Very stable.

2.4.3 Upward Heat Flux

Heat flux or thermal flux is the rate of heat energy transfer through a given surface and is measured in (W/m^2). Heat rate is a scalar quantity, while heat flux is a vector quantity. To define the heat flux at a certain point in space, one takes the limiting case where the size of the surface becomes infinitesimally small. The measurement of heat flux is most often done by measuring a temperature difference over a piece of material with known thermal conductivity. This method is analogous to a standard way to measure an electric current, where one measures the voltage drop over a known resistor.

One of the tools in a scientist's or engineer's toolbox is the energy balance. Such a balance can be set up for any physical system, from chemical reactors to living organisms, and generally takes the following form

$$\frac{\partial E_{in}}{\partial t} - \frac{\partial E_{out}}{\partial t} - \frac{\partial E_{accumulated}}{\partial t} = 0 \qquad (3)$$

Where, the three terms stand for the time rate of change of the total amount of incoming energy, the total amount of outgoing energy and the total amount of accumulated energy respectively. Now, if the only way the system exchanges energy with its surroundings is through heat transfer, the heat rate can be used to calculate the energy balance, since

$$\frac{\partial E_{in}}{\partial t} - \frac{\partial E_{out}}{\partial t} = \oint s \, \Phi_q . ds \qquad (4)$$

Where, we have integrated the heat flux density over the surface S of the system. In real-world applications one cannot know the exact heat flux at every point on the surface, but approximation schemes can be used to calculate the integral, for example Monte Carlo

integration.

2.4.4 Latent Heat Flux

Latent heat is the energy released or absorbed by a body or a thermodynamic system during a constant-temperature process. A typical example is a change of state of matter meaning a phase transition such as the melting of ice or the boiling of water. In meteorology, latent heat flux is the flux of heat from the Earth's surface to the atmosphere that is associated with evaporation or transpiration of water at the surface and subsequent condensation of water vapor in the troposphere. It is an important component of Earth's surface energy budget. Latent heat flux has been commonly measured with the Bowen ratio technique. A specific latent heat (L) expresses the amount of energy in the form of heat (Q) required to completely effect a phase change of a unit of mass (m), usually 1kg, of a substance as an intensive property.

$$L=Q/m \tag{5}$$

Where Q is the amount of energy released (kJ) or absorbed during the change of phase of the substance m is the mass of the substance (kg), and L is the specific latent heat for a particular substance ($kJ\text{-}kg^{-1}$)

2.4.5 Upward Moisture Heat Flux

Moisture refers to the presence of a liquid, especially water, often in trace amounts. Moisture also refers to the amount of water vapor present in the air. Moisture advection is the horizontal transport of water vapor by the wind. Measurement and knowledge of atmospheric water vapor, or moisture, is crucial in the prediction. Of all weather elements, especially clouds, fog, temperature, humidity thermal comfort indices and precipitation. The classical definition of advection, moisture advection is defined as

$$Adv(\rho_m) = -V.\nabla\rho_m \tag{6}$$

In which V is the horizontal wind vector, and ρ is the density of water vapor. However, water vapor content is usually measured in terms of mixing ratio in re-analyses or dew point (temperature to partial vapor pressure saturation i.e. relative humidity to 100%) in operational forecasting. The advection of dew point itself can be thought as moisture advection:

$$Adv(T_d) = V.\nabla T_d \tag{7}$$

In terms of mixing ratio, horizontal transport/advection can be represented in terms moisture flux:

$$F = qV$$

The value can integrated throughout the atmosphere to total transport of moisture through the vertical:

$$F = \int_0^\infty \rho f dz = -\int_p^0 \frac{f}{g} dp \tag{8}$$

Where, ρ is the density of air, p is the pressure at the ground surface. For the far right definition, we have used hydrostatic equilibrium approximation. And its divergence (convergence) implies net evapotranspiration (precipitation) is adding (removing) moisture from the column:

$$P - E - \frac{\partial}{\partial t}\left(\int_0^\infty \rho q dz\right) = -\nabla . F \tag{9}$$

Where P, E, and the integral term are precipitation, evapotranspiration, and time rate of change of perceptible water all represented in terms of mass per unit area.

2.4.6 Radiation Flux

Radiation flux is a measure of the amount of radiation received by an object from a given source. This can be any type of radiation, including electromagnetic, sound, and particles from a radioactive source. $\Phi = L/4\pi r^2$ is the radiation flux, L is the luminosity, or total power output of the source, and r is the distance from the radiation source. The units of radiation flux are $W \cdot m^{-2}$, or $kg \cdot s^{-3}$. Radiation flux density is a related measure that takes into account the area the radiation flux passes through, and is defined as the flux divided by the area it passes through. The Radiation flux density is also known as Intensity where $I = L/4\pi r^2$.

2.4.7 Heat Flux

Heat flux or thermal flux is the rate of heat energy transfer through a given surface per unit time. The SI unit of heat rate is joule per second, or watt. Heat flux density is the heat rate per unit area. In SI units, heat flux density is measured in [W/m^2]. Heat rate is a scalar quantity, while heat flux is a vectorial quantity. To define the heat flux at a certain point in space, one

takes the limiting case where the size of the surface becomes infinitesimally small. Heat flux is often denoted $_q$, the subscript φ_q specifying heat rate, as opposed to mass or momentum rate.

2.4.8 Downward shortwave radiation flux

Shortwave flux is a result of spectacular and diffuse reflection of incident shortwave radiation by the underlying surface. This shortwave radiation, as solar radiation, can have a profound impact on certain biophysical processes of vegetation, such as canopy photosynthesis and land surface energy budgets, by being absorbed into the soil and canopies. The downward solar flux at the surface is an important component of the earth's climate system, being a major factor governing the surface temperature and hydrologic cycle. The availability of derived flux climatologist from both ground-based measurements and satellite-based estimates provide a reference for properly assessing general circulation model biases, not only in the surface irradiance, but in the atmospheric factors (aerosols, clouds, and water vapor) affecting it.

The down-welling surface shortwave radiation flux (DSSF) refers to the radiative energy in the wavelength interval [0.3μm, 4.0μm] reaching the Earth's surface per time and surface unit. It essentially depends on the solar zenith angle, on cloud coverage, and to a lesser extent on atmospheric absorption and surface albedo. The surface radiation budget is comprised of four different terms:

$$Q^* = SW^{\uparrow} + SW_{\downarrow} + LW^{\uparrow} + LW_{\downarrow} \quad (10)$$

Where, Q* is the net surface radiation (W m^{-2}), $SW^{\uparrow}$ up is the upwelling reflected shortwave solar radiation, $SW_{\downarrow}$ down is the down-welling shortwave radiation that is transmitted through the atmosphere, originating from the sun, $LW^{\uparrow}$ up is the upwelling long wave (IR) radiation emitted by the earth's surface, $LW_{\downarrow}$ down is the diffuse down welling radiation. Downward fluxes are negative, upward fluxes are positive.

2.4.9 Downward long wave radiation flux

Long wave radiation flux is an important part of the surface heat budget, is generally represented by $\varepsilon\sigma T_r^4$, where ε is the surface emissivity, σ is the Stefan–Boltzmann constant, and T_r is the measured radiometric temperature. *EσTr4* differs from hemispheric emission because the measured radiometric temperature is anisotropic for an uneven surface. The flux difference between $\varepsilon\sigma T_r^4$ and directly measured flux was up to 8% of the directly measured

flux, which could be greater than the typical error in measurement of turbulent heat flux over a building canopy. The flux difference increased as the temperature variation within the urban street canyon increased, and also with increasing difference between the incident solar radiation of the building walls and street canyon floors (pavement, roads, ground surface). Theoretical calculations indicate that the flux difference is due to the structure of the building canopy and the temperature difference between the walls and canopy floors. A numerical model of a building canopy heat budget shows that the flux difference increases as the street canyon aspect ratio increases.

2.4.10 Outgoing Long Wave Radiation (OLR)

Outgoing long wave radiation (OLR) is the emission to space of terrestrial radiation from the top of the earth's atmosphere. In physical terms it is strongly controlled by three main meteorological variables, namely the temperature of the earth and the atmosphere above it, the presence of water vapor in that atmosphere (which strongly absorbs infrared radiation attenuating the terrestrial signal) and the presence of clouds (which may completely block all outgoing infrared radiation from the surface). Thus, global maps of OLR averages and anomalies reveal information on the temperature, humidity and cloudiness of the atmosphere. The equation of outgoing long wave radiation can be written as,

$$L^{\uparrow} = \varepsilon_S \sigma T_S^4 \text{ (W m}^{-2)} \qquad (11)$$

Where ε_S is the emissivity of the surface in the long wave wavelength region, σ is the Stephan-Boltzmann constant $= \left(5.67 \times 10^{-8}\right)$ and T_s the absolute surface temperature. For most surface types ε_S is close to 1. Note that if $\varepsilon_S < 1$ a part of the incoming long wave radiation is reflected by the surface. Equation (1) now reads as:

$$L^{\uparrow} = \varepsilon_S \sigma T_S^4 + \left(1 - \varepsilon_S\right) L^{\uparrow} \text{ (W m}^{-2)} \qquad (12)$$

Where $L^{\downarrow}$ is the incoming long wave radiation. So OLR is a critical component of the Earth's energy budget that represents the total radiation going to space emitted by the atmosphere. Earth's radiation balance is quite closely achieved since the OLR very nearly equals the shortwave absorbed radiation received at high energy from the sun. Thus, the Earth's average temperature is very nearly stable. The OLR is affected by clouds and dust in the atmosphere, which tend to reduce it to below clear sky values. The minimum in OLR, or the longwave emitted flux near the equator is due to the high cloud tops associated with the inter-tropical

convergence zone (ITCZ), a region of persistent thunderstorms. This minimum migrates about the equator as seen in the monthly mean maps, and is also seen as a maximum in albedo.

2.4.11 Shortwave Radiation

Shortwave radiation is radiant energy with wavelengths in the visible, ultraviolet, and near-infrared spectra. There is no standard cut-off for the near-infrared range; therefore, the shortwave radiation range is also variously defined. It may be broadly defined to include all radiation with a wavelength between 0.1 and 5.0μm or narrowly defined so as to include only radiation between 0.2μm and 3.0μm. There is little radiation flux to the Earth's surface below 0.2μm or above 3.0μm, although photon flux remains significant as far as 6.0μm, compared to shorter wavelength fluxes.

2.5 Weather Research & Forecasting (WRF) Model

The Weather Research and Forecasting (WRF) Model is a next-generation mesoscale numerical weather prediction (NWP) system designed to serve both atmospheric research and operational forecasting needs. It features two dynamical cores, a data assimilation system, and a software architecture facilitating parallel computation and system extensibility. The model serves a wide range of meteorological applications across scales from tens of meters to thousands of kilometers. The effort to develop WRF began in the latter part of the 1990's and was a collaborative partnership principally among the National Center for Atmospheric Research (NCAR), the National Oceanic and Atmospheric Administration (NOAA) represented by the National Centers for Environmental Prediction (NCEP) and the Forecast Systems Laboratory (FSL) the Air Force Weather Agency (AFWA), the Naval Research Laboratory, the University of Oklahoma, and the Federal Aviation Administration (FAA).

The WRF model is an atmospheric simulation system which is designed for both operational and research use. WRF is currently in operational use at the NOAA national weather service as well as at the air force weather agency and meteorological services worldwide. Getting weather predictions in time using latest advances in atmospheric sciences is a challenge even on the fastest super computers. Timely weather predictions are particularly useful for severe weather events when lives and property are at risk. Microphysics is a crucial but computationally intensive part of WRF. WRF offers two dynamical solvers for its computation of the atmospheric governing equations, and the variants of the model are known as WRF-ARW and WRF-NMM. The Advanced Research WRF (ARW) is supported

to the community by the NCAR Mesoscale and Microscale Meteorology Division. The WRF-NMM solver variant was based on the Eta Model, and later Non hydrostatic Mesoscale Model, developed at NCEP. The WRF-NMM is supported to the community by the Developmental Test bed Center.

2.5.1 Microphysics Schemes in WRF-ARW Model

Microphysics includes explicitly resolved water vapor, cloud and precipitation processes. The model is general enough to accommodate any number of mass mixing-ratio variables, and other quantities such as number concentrations. Four-dimensional arrays with three spatial indices and one species index are used to carry such scalars. Memory, i.e., the size of the fourth dimension in these arrays, is allocated depending on the needs of the scheme chosen, and advection of the species also applies to all those required by the microphysics option. In the current version of the ARW, microphysics is carried out at the end of the time-step as an adjustment process, and so does not provide tendencies. The rationale for this is that condensation adjustment should be at the end of the time-step to guarantee that the final saturation balance is accurate for the updated temperature and moisture. However, it is also important to have the latent heating forcing for potential temperature during the dynamical sub-steps and this is done by saving the microphysical heating as an approximation for the next time-step as described.

2.5.1.1 Kessler Scheme

The Kessler scheme is a simple warm cloud scheme that includes water vapor, cloud water and rain. The microphysical process consists of the production, fall and evaporation of rain, the accumulation and auto conversion of cloud water and the production of cloud water from condensation. A warm-rain scheme has been used commonly in idealized cloud modeling studies. Kessler scheme is one moment scheme. The purpose of the scheme is to increase understanding of the roles of cloud conversion, accretion, evaporation, and entrainment processes in shaping the distributions of water vapor, cloud, and precipitation associated with tropical circulations. This scheme is idealized microphysics process without the consideration of ice phase and melting zone. Kessler scheme has been used widely in cloud modeling studies due to its simplicity. The equation represented the processes between cloud, vapor and rain are also much simplified compared with other scheme. Kessler scheme produced much heavier precipitation and can show unrealistic precipitation profiles in some studies (Kessler, 1969)

2.5.1.2 Lin *et al*., Scheme

A sophisticated scheme that has ice, snow and graupel processes, suitable for real-data high-resolution simulations. Lin *et al.* (1983) scheme includes six classes of hydrometeors are included: water vapor, cloud water, rain water, cloud ice, snow, and graupel. All parameterization production terms are based on Lin *et al*. (1983). This is a relatively sophisticated microphysics scheme in WRF, and it is more suitable for use in research studies. The scheme is taken from Purdue cloud model and the details can be found in Chen and Sun *et al*. (2002) 2-D microphysics scheme. This is one of the first schemes to parameterize snow, graupel, and mixed-phase processes. It has been used extensively in research studies and in mesoscale NWP Model. The scheme includes ice sedimentation and time-split fall terms.

2.5.1.3 WRF Single Moment 3 (WSM3) - Class Scheme

The combination of ice sedimentation and other new ice-phase parameterizations follows Hong *et al*., (2004) is called the WRF single-moment microphysics scheme. It is called simple ice scheme because it is predicts three categories of hydrometers: vapor, cloud water/ice and rain/snow. It is assuming cloud water and rain for temperatures above freezing, and cloud ice and snow for temperatures below freezing. A major difference from other approaches is that a diagnostic relation is used for ice number concentration that is based on ice mass content rather than temperature. The computational procedures of WSM3 explain by Hong and Lim (2006) it is computationally efficient for the inclusion of ice processes, but lacks super cooled water and gradual melting rates.

2.5.1.4 Ferrier Scheme

Ferrier scheme simulate the changes in water vapor and condensate in the forms of cloud water, rain, cloud ice, and precipitation ice. Local storage arrays retain first-guess information that extract contributions of cloud water, rain, cloud ice, and precipitation ice of variable density in the form of snow, graupel, or sleet. The density of precipitation ice is expected from a local array that stores information on the total growth of ice by vapor deposition and accretion of liquid water. Sedimentation is treated by partitioning the time averaged flux of precipitation into a grid box between local storage in the box and fall out through the bottom of the box.

2.5.1.5 WRF Single-Moment 6-class Microphysics Scheme (WSM6)

The WRF-single-moment-6-class (WSM6) microphysics scheme has been one of the options of microphysical process in the WRF model. This scheme predicts the mixing ratios for water vapor, cloud water, cloud ice, snow, rain, and graupel. We attempt to improve such existing deficiencies in the WSM6 scheme by incorporating the prediction of number concentrations for warm rain species. A new method for representing mixed-phase particle fall speeds for the snow and graupel by assigning a single fall speed to both that is weighted by the mixing ratios, and applying that fall speed to both sedimentation and accumulation processes is introduced of the three WSM schemes, the WSM6 scheme is the most suitable for cloud-resolving grids, considering the efficiency and theoretical backgrounds (Hong *et al*., 2006). The WSM6 scheme has been developed by adding additional process related to graupel to the WSM5 scheme (Hong and Lim, 2006).

2.5.1.6 Thompson *et al.,* Scheme

A bulk microphysical parameterization (BMP) developed for use with WRF or other mesoscale models. The snow size distribution depends on both ice water content and temperature and is represented as a sum of exponential and gamma distributions. Furthermore, snow assumes a non-spherical shape with a bulk density that varies inversely with diameter as found in observations. A new scheme with ice, snow and graupel processes suitable for high-resolution simulations. This adds rain number concentration and updates the scheme from the one in Version 3.0 New Thompson et al. scheme in V3.1. Replacement of Thompson *et al.,* (2007) scheme that was option 8 in V3.0 6-class microphysics with graupel, ice and rain number concentrations also predicted.

2.5.2 Cumulus Parameterization

These schemes are responsible for the sub-grid-scale effects of convective and/or shallow clouds. The schemes are intended to represent vertical fluxes due to unresolved updrafts and downdrafts and compensating motion outside the clouds. They operate only on individual columns where the scheme is triggered and provide vertical heating and moistening profiles. Some schemes provide cloud and precipitation field tendencies in the column, and future schemes may provide momentum tendencies due to convective transport of momentum. The schemes all provide the convective component of surface rainfall. Cumulus parameterizations are theoretically only valid for coarser grid sizes, (e.g., greater than 10 km), where they necessary to properly release latent heat on a realistic time scale in the convective columns.

Where the assumptions about the convective eddies being entirely sub-grid-scale break down for finer grid sizes, sometimes these schemes have been found to be helpful in triggering convection in 5-10 km grid applications. Generally they should not be used when the model can resolve the convective eddies itself. These schemes are responsible for the sub-grid-scale effects of convective and shallow clouds. The schemes are intended to represent vertical fluxes due to unresolved updrafts and downdrafts and compensating motion outside the clouds.

2.5.2.1 Kain - Fritsch (KF) Scheme

In the KF scheme the condensates in the updraft are converted into precipitation when their amount exceeds threshold value. In this scheme the convection consumes the convective available potential energy in a certain time scale. The KF scheme also includes the shallow convection other than deep convection. The shallow convection creates non-perceptible condensates and the shallowness of the convection is determined by a vertical extent of the cloud layer that is known by a function of temperature at LCL of rising air parcel. The KF scheme was derived from the Fritsch–Chappell, and its fundamental framework and closure assumptions are described by Fritsch and Chappell (1980). KF (1990) modified the updraft model in the scheme and later introduced numerous other changes, so that it eventually became distinctly different from the Fritsch–Chappell scheme. It was distinguished from its parent algorithm by referring to the more elaborate code as the KF scheme, beginning in the early 1990s. This is also deep and shallow convection sub-grid scheme using a mass flux approach with downdrafts and CAPE removal time scale. Updraft generates condensate and dump condensate into environment downdraft evaporates condensate at a rate that depends on RH and depth of downdraft leftover condensate accumulates at surface as precipitation.

2.5.2.2 Betts - Miller - Janjic (BMJ) Scheme

The BMJ cumulus parameterization scheme is a nudging type adjustment of temperature and humidity in grid scale. The scheme adjusts the sounding towards a pre-determined, post convective profile derived from climatology. This post convective profile has been defined by points at the cloud base, cloud top and freezing level. In this scheme there is no explicit updraft or downdraft and no cloud detrainment occur. Convection is initiated when soundings are moist through a deep layer and when CAPE and convective cloud depth thresholds are exceeded. Betts and Miller proposed a convective adjustment scheme that includes both deep and shallow convection. The deep convection in the Betts–Miller scheme is similar to the

other adjustment schemes except that it uses empirically based quasi-equilibrium thermodynamic profiles as a reference state rather than a moist adiabatic. The basic shape of these quasi-equilibrium reference profiles is based on the numerous observations. The construction of the reference profiles and the specification of the relaxation timescale are two major components of the Betts–Miller scheme (Janjic, 1994).

These points and thresholds can vary by season and between the tropics and extra tropics. Compared with the original sounding, the sounding modified to the post convective profile will note a net change in perceptible water as well as changes in net heating and cooling. Convection is initiated when soundings are moist through a deep layer and when CAPE and convective cloud depth thresholds are exceeded. Important vertical structures may be eliminated since the reference profiles are based on climatology. Convection only initiated for soundings with deep moisture profile. When convection is initiated the scheme often rains out to much water. This is because the reference profile is too dry for the forecast scenario or the transition to the reference profile was too rapid. Scheme does not account for the strength of CAPE inhibiting convective development. Scheme does not account for any changes below the cloud base.

2.5.3 Planetary Boundary Layer (PBL)

The PBL is the layer in the lower part of the troposphere with thickness ranging from a few hundred meters to a few kilometers within which the effects of the Earth's surface are felt by the atmosphere. The PBL processes represent a consequence of interaction between the lowest layer of air and the underlying surface. The interactions can significant impact on the dynamics of the upper air flows. The influences of the small-scale eddy on large scale atmospheric circulations may be included in the model equations. Accurate depiction of meteorological conditions, especially within the PBL, is important for air pollution modeling, and PBL parameterization schemes play a critical role in simulating the boundary layer. It is a very important portion of the atmosphere to correctly model to provide accurate forecasts, e.g., air pollution forecasts (Deardorff 1972; Pleim 2007). As important as the PBL is, it has one basic property whose accurate and realistic prediction is paramount to its correct modeling: its height. After all, the height of the top of the PBL defines its upper boundary. This is critical since PBL parameterizations schemes in WRF-ARW models need to know the extent through which to mix properties such as heavy rainfall, relative humidity, outgoing long wave flux, downward long wave flux.

PBL schemes were developed to help resolve the turbulent fluxes of heat, moisture, and momentum in the boundary layer. Another important issue is the interaction between the atmosphere and the surface. The PBL schemes handle the latent and sensible heat fluxes into the atmosphere, the frictional effects with the surface and the strong sub–grid–scale mixing which takes place in the lower levels due to these processes.

2.5.3.1 Yonsei University (YSU) Scheme

The Yonsei University (YSU) PBL is the next generation of the Medium Range Forecast (MRF), Non local-K scheme with explicit entrainment layer and parabolic K profile in unstable mixed layer. The YSU scheme is a bulk scheme that expresses non-local mixing by convective large eddies. Non-local mixing is achieved by adding a non-local gradient adjustment term to the local gradient. At the top of the PBL, the YSU scheme uses explicit treatment of the entrainment layer, which is proportional to the surface layer flux (Shin and Hong 2011; Hong *et al*. 2006).

2.5.3.2 Map Projection

Commonly, a map projection is a systematic transformation of the latitudes and longitudes of locations on the surface of a sphere or an ellipsoid into locations on a plane. Map projections are necessary for creating maps. All map projections distort the surface in some fashion. Depending on the purpose of the map, some distortions are acceptable and others are not; therefore, different map projections exist in order to preserve some properties of the sphere-like body at the expense of other properties. There is no limit to the number of possible map projections. More generally, the surfaces of planetary bodies can be mapped even if they are too irregular to be modeled well with a sphere or ellipsoid. Even more generally, projections are the subject of several pure mathematical fields, including differential geometry and projective geometry. However, map projection refers specifically to a cartographic projection (Snyder, 1989).

2.5.3.3 Mercator Projection

The Mercator projection is a cylindrical map projection presented by the Flemish geographer and cartographer Gerardus Mercator in 1569. It became the standard map projection for nautical purposes because of its ability to represent lines of constant course, known as rhumb lines_ loxodromes, as straight segments which conserve the angles with the meridians. While the linear scale is equal in all directions around any point, thus preserving the angles and the shapes of small objects, the Mercator projection distorts the size and shape of large objects,

as the scale increases from the Equator to the poles, where it becomes infinite. Although the Mercator projection is still used commonly for navigation, due to its unique properties, cartographers agree that it is not suited to general reference world maps due to its distortion of land area. Mercator himself used the equal-area sinusoidal projection to show relative areas. As a result of these criticisms, modern atlases no longer use the Mercator projection for world maps or for areas distant from the equator, preferring other cylindrical projection or forms of equal-area projection. The Mercator projection is still commonly used for areas near the equator, however, where distortion is minimal.

2.5.3.4 Arakawa Staggered C-grids

The Arakawa grid system depicts different ways to represent and compute orthogonal physical quantities on rectangular grids used for Earth system models for meteorology and oceanography. For example, the Weather Research and Forecasting Model use the Arakawa Staggered C-Grid in its atmospheric calculations when using the ARW core. The staggered Arakawa C-grid further separates evaluation of vector quantities compared to the Arakawa B-grid. E.g., instead of evaluating both east-west (u) and north-south (v) velocity components at the grid center, one might evaluate the u components at the centers of the left and right grid faces, and the v components at the centers of the upper and lower grid faces (Arakawa and Lamb1977)

Chapter III

Model Description and Methodology

In the present study the Weather Research and Forecast (WRF-ARW Version 3.2.1) model consists of fully compressible non-hydrostatic equations and different prognostic variables is utilized. The model vertical coordinate is terrain following hydrostatic pressure and the horizontal grid is Arakawa C-grid staggering. Third-order Runge-Kutta time integration is used in the model. The model description and methodology are given below:

3.1 Model Description

The model is configured in single domain, 12 km horizontal grid spacing with 186×196 grids in the west-east and north-south directions and 28 vertical levels. The six different microphysics schemes used are Kessler, Lin *et al*., and WSM3 for explicit moisture processes, Eta (Ferrier), WSM 6-class graupel and Thompson graupel schemes. The Lin *et al*., WSM6 and Thompson MP schemes contain prognostic equations for cloud water, rainwater, cloud ice, snow, and graupel mixing ratio. The Kessler, WSM3 and Ferrier MP schemes contain prognostic equations for cloud water and rainwater mixing ratios. The Ferrier scheme also contains prognostic equations for cloud water, rainwater and snow mixing ratio. Dudhia simple five-layer soil thermal diffusion scheme for soil processes, Rapid Radiative Transfer Model (RRTM) for long wave scheme for shortwave radiation and Yonsei University scheme planetary boundary layer (PBL) have been used for the simulation of TC Mala (2006), Roanu (2016) and Hudhud (2014) . Two different cumulus parameterization (CP) schemes have been used in WRF model are Kain-Fritsch (KF) (Kain and Fritsch, 1990, 1993; Kain, 2004) and Betts-Miller-Janjic (BMJ) (Janjic, 1994, 2000). The 5-layer thermal diffusion option with prognostic soil temperature and land-use-dependent soil-moisture availability represented the land surface. The RRTM scheme has been chosen for long-wave radiation with the Dudhia scheme for short wave radiation. The model domain is given in Fig. 1. The detail of the model and domain configuration is given in Table 1.

3.2 Model Domain and Configuration

In this study, the WRF–ARW model has been configured with single domain. For the analysis of energy and its fluxes, the model domain has been divided into 5 different regions. We have divided the model domain into different regions are R1 (22-26^{o}N & 87-93^{o}E), R2 (18-22^{o}N & 81-85^{o}E), R3 (14-18^{o}N & 78-84^{o}E), R4 (12-22^{o}N & 85-94^{o}E) and R5 (17-22^{o}N & 94-97^{o}E).

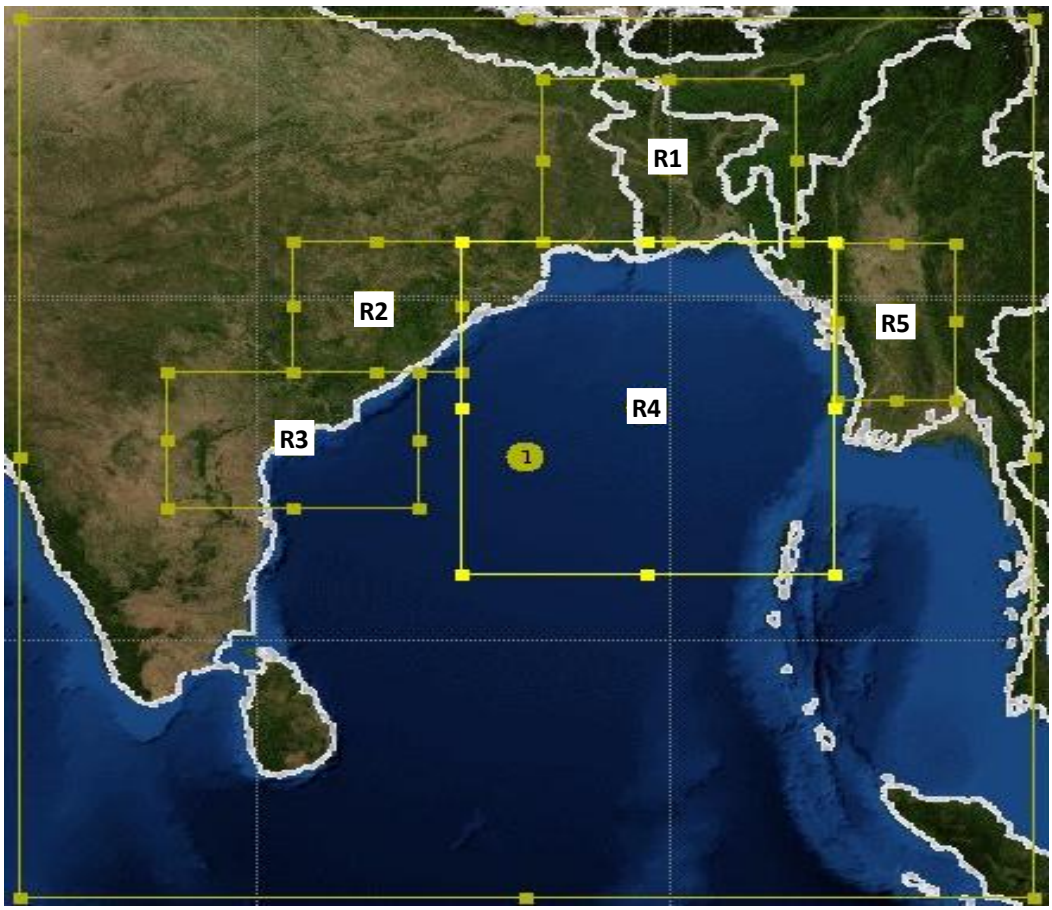

Fig. 1: The WRF–ARW domain set up for the study.

3.3 Data and Methodology

Final Reanalysis (FNL) data (1^{o} x1^{o}) collected from National Centre for Environment Prediction (NCEP) is used as initial and lateral boundary conditions (LBCs) which is updated at six hours interval i.e. the model is initialized with 0000, 0600, 1200 and 1800 UTC initial field of corresponding date. The GFS data is used for the simulation of Tropical Cyclone Roanu. The NCEP FNL data is interpolated to the model horizontal and vertical grids and the model was integrated for 96 and 72-h period for TC Roanu, Hudhud and Mala.

Table 1: WRF Model and Domain Configurations

Dynamics	Non-hydrostatic
Number of domain	1
Central points of the domain	Central Lat.: 16.5°N, Central Lon.: 86.5°E
Horizontal grid distance	12 km
Integration time step	60 s
Number of grid points	X-direction 186 points, Y-direction 196 points
Map projection	Mercator
Horizontal grid distribution	Arakawa C-grid
Nesting	One way
Vertical co-ordinate	Terrain-following hydrostatic-pressure co-ordinate (28 sigma levels up to 100 hPa)
Time integration	3rd order Runge-Kutta
Spatial differencing scheme	6th order centered differencing
Initial conditions	Three-dimensional real-data (FNL: 1° × 1°)
Lateral boundary condition	Specified options for real-data
Top boundary condition	Gravity wave absorbing
Bottom boundary condition	Physical or free-slip
Diffusion and Damping	Simple Diffusion
Microphysics	1) Kessler, (2) Lin *et al.,* (1983) scheme, (3) WSM3-class scheme, (4) Eta (Ferrier) scheme, (5) WSM 6-class graupel scheme (Hong, *et al.,* 2004) and (6) Thompson graupel scheme.
Radiation scheme	Dudhia (1989) for short wave radiation/ RRTM long wave Mlawer *et al.,*(1997)
Surface layer	Monin– Obukhov similarity theory scheme. (Hong and Pan, 1996)
Land surface parameterization	5 Layer Thermal diffusion scheme (Ek *et al.,* 2003)
Cumulus parameterization schemes	1) Kain-Fritsch scheme (KF), (Kain and Fritsch, 1993; Kain, 2004) Betts-Miller-Janjic (BMJ) (Janjic, 2000)
PBL parameterization	Yonsei University Scheme (YSU) (Hong *et al*., 2006) scheme

24 experiments have been conducted in each case by using different microphysics schemes (e.g., Kessler, Lin *et al*., WSM3-class simple ice scheme, Ferrier, WSM6-class graupel scheme and Thompson graupel) in combinations with Kain-Fritsch (KF) and Betts-Miller-Janjic (BMJ) CP schemes with different initial conditions. In this regard, the initial conditions of 0000 UTC of 18 and 19 May 2016 have been considered for TC Roanu, 0000 UTC of 08 and 09 October 2014 have been considered for TC Hudhud and 26 and 27 April 2006 have been considered for TC Mala. The different periods for different cyclones were characterized by the formation of tropical cyclone until dissipation.

Table 2: Observed information of Simulated Tropical Cyclones in the Bay of Bengal

Name of TC	Country of landfall	Date of Formation	Date and Time of landfall UTC	Minimum SLP, hPa	Maximum Sustained Wind Speed, km/h
Mala	Myanmar	24 April	0700 UTC 29 April 2006	954	220
Hudhud	Visakhapatnam	7 October	0630 and 0730 UTC of 12 October 2014	950	260
Roanu	Bangladesh	17 May	1000 UTC of 21 May 2016	983	100

The model simulated MSLP, maximum wind at 10 m level, track, Convective available potential energy (CAPE), Convective inhibition (CIN), Downward long wave heat flux (DLHF), Downward shortwave heat flux (DSHF), Ground heat flux (GHF), latent heat flux (LH), moisture heat flux (QFX), Outgoing long wave radiation (OLR), and upward heat flux (HFX) have been studied and analyzed for three different cyclones. Simulated track and intensity have also been compared with the IMD and JTWC observed results. We have divided the model domain into different regions R1 in the northern side of BoB, R2 in the northwestern side of BoB, R3 in the western side of BoB, R4 in the Oceanic area and R5 in the northeastern side of BoB.

We have calculated the energy and its fluxes in different regions by using the software Grid Analysis and Display Systems (GrADS). The Grid Analysis and Display System (GrADS) is an interactive desktop tool that is used for easy access, manipulation, and visualization of earth science data. GrADS have two data models for handling gridded and station data. GrADS supports many data file formats, including binary (stream or sequential), GRIB (version 1 and 2), NetCDF, HDF (version 4 and 5), and BUFR (for station data). GrADS have been implemented worldwide on a variety of commonly used operating systems. GrADS use a 5-Dimensional data environment: the four conventional dimensions (longitude, latitude, vertical level, and time) plus an optional 5th dimension for grids that is generally implemented but designed to be used for ensembles. Data sets are placed within the 5-D space by use of a data descriptor file. GrADS handles grids that are regular, non-linearly spaced, gaussian, or of variable resolution. Data from different data sets may be graphically overlaid, with correct spatial and time registration. Operations are executed interactively by entering FORTRAN-like expressions at the command line. A rich set of built-in functions are provided, but users may also add their own functions as external routines written in any programming language. Data may be displayed using a variety of graphical techniques: line and bar graphs, scatter plots, smoothed contours, shaded contours, streamlines, wind vectors, grid boxes, shaded grid boxes, and station model plots. Graphics may be output in PostScript or image formats. GrADS provides geo physically intuitive defaults, but the user has the option to control all aspects of graphics output. After getting txt data from grads we converted it into Excel sheet and plotted graph using Excel. We have plotted the data on Excel at every 12 hourly intervals for observing the changing scenario of energy and its fluxes for the movement of TCs. Paint (formerly Paintbrush for Windows) is a simple computer graphics program that has been included with all versions of Microsoft Windows. It is often referred to as MS Paint or Microsoft Paint. The program mainly opens and saves files as Windows bitmap (24-bit, 256 color, 16 color, and monochrome, all with the .bmp extension), JPEG, GIF. We have converted our Excel graph into Paint and then transferred to Word.

Chapter IV

Results and Discussions

The model has simulated MSLP, maximum wind at 10 m level, track, Convective available potential energy (CAPE), Convective inhibition (CIN), Downward long wave heat flux (DLHF), Downward shortwave heat flux (DSHF), Ground heat flux (GHF), latent heat flux (LH), moisture heat flux (QFX), Outgoing long wave radiation (OLR), and upward heat flux (HFX) have been studied and analyzed for three different cyclones. Simulated track and intensity have also been compared with the IMD and JTWC observed results. The results have been presented in the following sub sections.

4.1 Tropical Cyclone Roanu

4.1.1 Synoptic Situation Tropical Cyclone Roanu

A low pressure area developed over southwest Bay of Bengal (BoB) off Sri Lanka coast on 14 May 2016. In the morning of 15 May, it lay as a well marked low pressure area over southwest BoB and adjoining Sri Lanka and it moved northwestwards and in the morning of 16th its position was in southwest BoB. The low pressure area moved further north and concentrated into a depression (D) and its position was 11^{o}N and 81^{o}E in the morning of 17 May. The depression intensified into a deep depression (DD) and lay centered at 13.3^{o}N and 81^{o}E over west central and adjoining southwest BoB at 0300 UTC of 18 May. The system maintained its intensity of 83 km/h and crossed Bangladesh coast near 22.6^{o}N and 91.6^{o}E to the north of Chittagong around 1000 UTC of 21 May as a CS. After landfall, the system started weakening due to land interactions.

4.1.2 Intensity of TC Roanu

The storm intensity forecasts in terms of minimum CSLP and maximum wind speed (m/s) at 10 m level using different MP schemes for 84 and 60-h (every 3 hourly) are presented in Figs. 1(a-h). Figures 1(a-d) show the simulated CSLP for six different MP schemes in combination with two different CP schemes and two different initial conditions at 0000 UTC of 18 and 19 May 2016. The simulated CSLP for all MP schemes in combination with KF scheme is much higher than that of BMJ scheme with the initial conditions at 0000 UTC of 18 and 19 May. The simulated pressure fall and10m sustained wind with the 0000 UTC of 18 and 19 May initial conditions for all combination of MP schemes in combination with KF

and BMJ schemes are much higher than that of IMD observed results. The pressure departure is found minimum for Thompson scheme and maximum for WSM3 and Kessler schemes coupling with KF and BMJ schemes. The simulated pressure fall and 10m sustained wind speed for all MPs in combination with KF and BMJ schemes indicate that the system has attained severe cyclonic storm with core of hurricane intensity but the observation indicates that the system attained the intensity of cyclonic storm (983 hPa, 23 m s^{-1}).

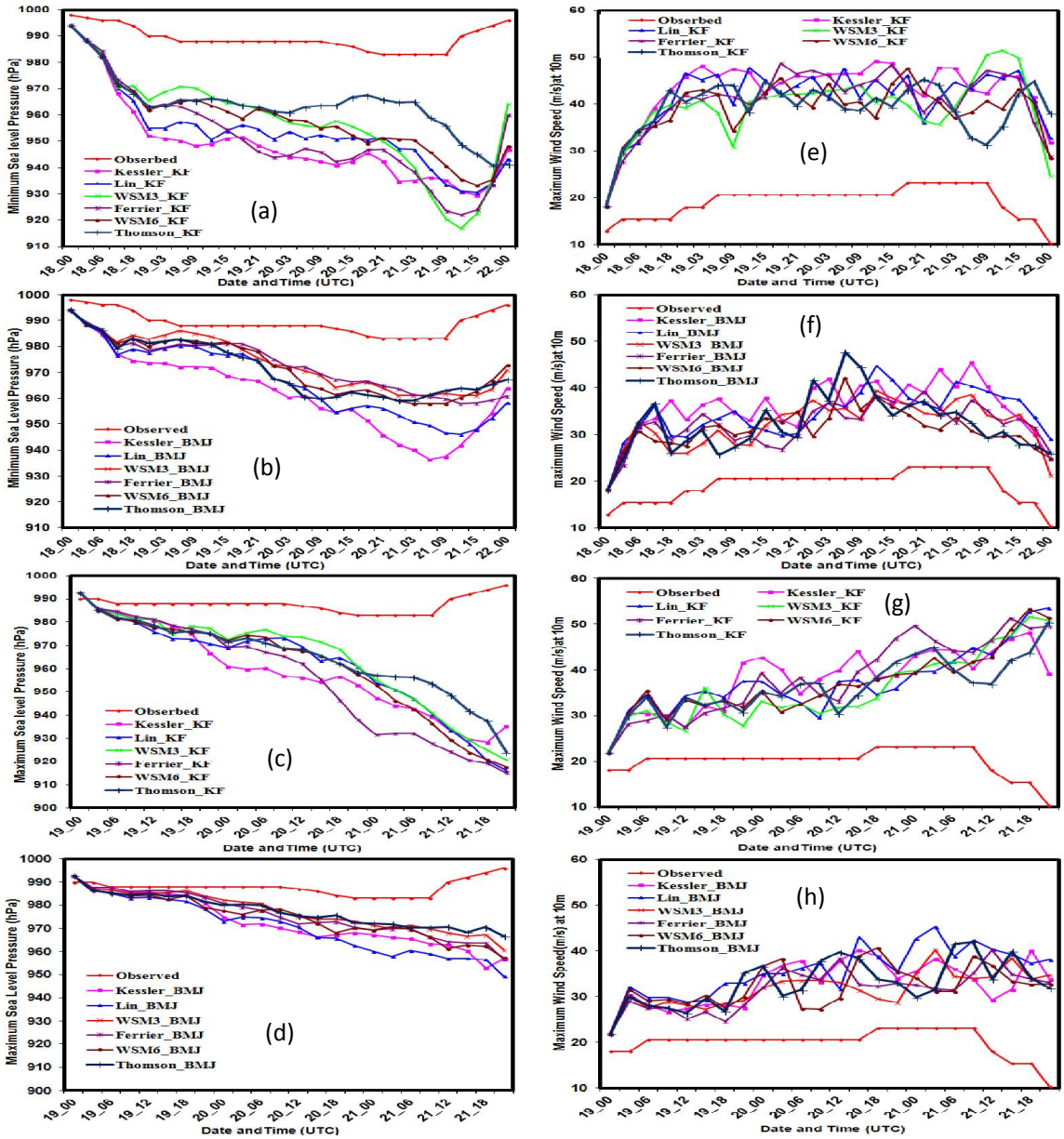

Fig. 2: Model simulated and IMD observed (a-d) minimum CSLP and (e-h) maximum sustained wind at 10m level of TC Roanu using six different MP schemes coupling with KF and BMJ schemes with the initial conditions at 0000 UTC of 18 and 19 May 2016.

The simulated intensities for different combination of MPs and CPs with the initial conditions of 0000 UTC of 18 May are (930 hPa, 49 m s^{-1}) for Kessler-KF, (931 hPa, 47 m s^{-1}) for Lin et al-KF, (917 hPa, 51 m s^{-1}) for WSM3-KF, (922 hPa, 48 m s^{-1}) for Ferrier-KF, (933 hPa, 48 m s^{-1}) for WSM6-KF and (941 hPa, 45 m s^{-1}) for Thompson-KF respectively.

4.1.3 Track of TC Roanu

The simulated tracks for 84 and 60-h and IMD observed track of TC Roanu for different cloud MP schemes are displayed in Fig. 3(a-d). It can be noted that roughly up to the landfall time (i.e., official landfall as on 1000 UTC of 21 May 2016), the track forecast for different sensitivity experiments have shown reasonably accurate prediction. All the simulations have captured the north-northeastward movement of TC Roanu with the initial conditions at 0000 UTC of 18 and 19 May 2016. The sensitivity test has shown significant difference in tracks among the different microphysical schemes in combination with KF and BMJ schemes with the initial conditions at 0000 UTC of 18 May. Lin-KF, WSM6-KF and Ferrier-KF combinations have simulated less deviated track and Kessler-KF and WSM3-KF combinations have simulated most deviated track with the initial conditions at 0000 UTC of 18 May 2016.

The simulated track has deviated towards left using Kessler-KF combination and towards right using WSM3-KF combinations from the IMD track. At the time of landfall, Lin and Ferrier schemes in combination with KF scheme and WSM6 and Thompson schemes in combination with BMJ scheme have simulated less deviated track with the initial conditions of 0000 UTC of 18 May. The simulated tracks for all MP schemes coupling with KF and BMJ schemes are found to move parallel to the observed track. After that the simulated track has followed the same path with the initial conditions at 0000 UTC of 18 May but the simulated track has moved towards left. The simulated landfall position for different MP schemes is very near to the observed landfall position with the initial conditions of 0000 UTC of 18 and 19 May. The observed landfall time for all MP schemes has almost matched with the model simulated landfall time by using the initial conditions of 0000 UTC of 18 and 19 May. The track deviation has increased for all MP schemes coupling with BMJ scheme with the initial conditions at 0000 UTC of 19 May. The landfall time has most deviated by WSM3, Ferrier, and WSM6 in combination with BMJ and Kessler-BMJ, Lin-BMJ and Thomson-BMJ combinations have simulated less deviated track with the initial conditions of 0000 UTC of 19 May.

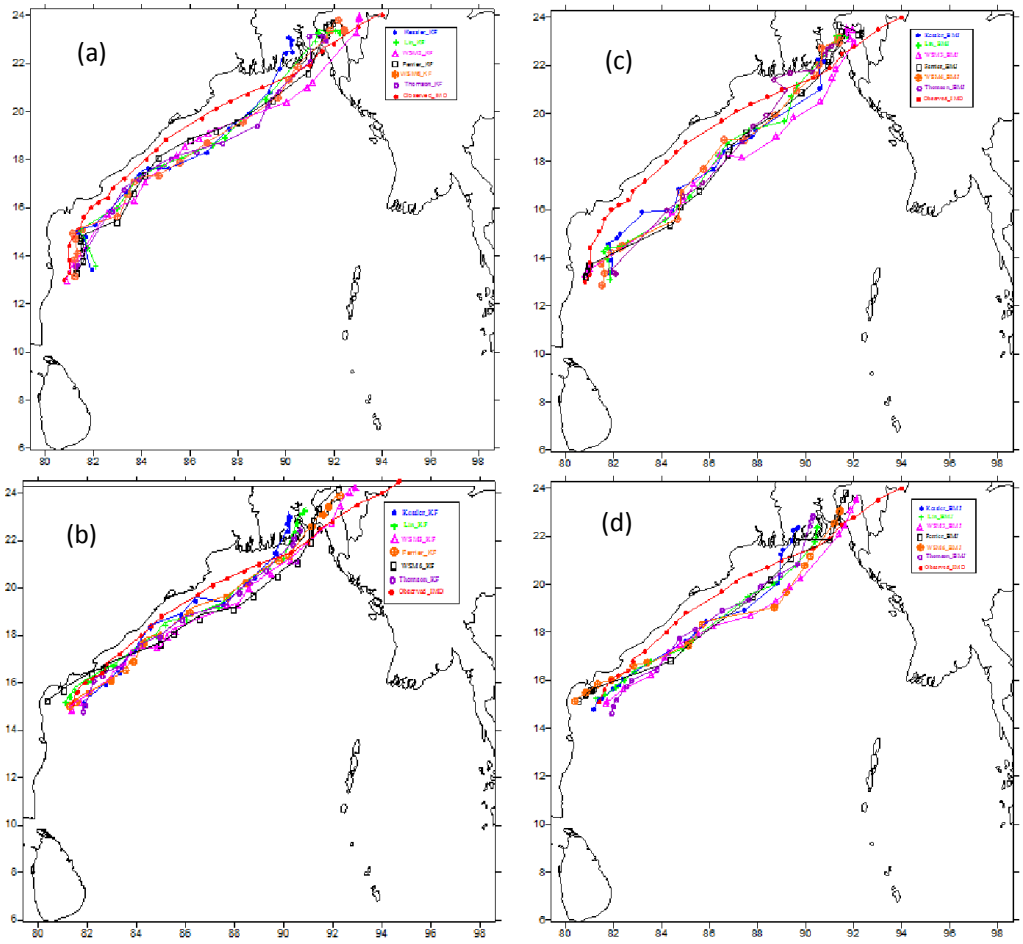

Fig. 3: Model simulated IMD Observed tracks of TC 'Roanu' using six different MP schemes coupling with (a-b) KF and (c-d) BMJ schemes with the initial conditions at 0000 UTC of 18 and 19 May.

4.1.4 Track Error of TC Roanu

The track error has been estimated on the basis of IMD observed track. The track error with respect to IMD observed tracks are presented in Fig. 4(a-d) respectively. The error was not systematic by using KF and BMJ schemes with the initial conditions at 0000 UTC of 18 and 19 May 2016 but the track error on 18 May is very much less compared to the initial conditions of 19 May. Ferrier-KF combination has simulated less deviated track and Thompson-BMJ has simulated the most deviated track with respect to observed track of IMD with the initial conditions at 0000 UTC of 18 May. Again Kessler-KF combination has simulated less deviated track and Ferrier-BMJ has simulated the most deviated track with the initial conditions at 0000 UTC of 19 May. The track error is minimum in comparison with IMD observed track at the time of landfall using WSM3 and Thompson schemes coupling

with KF scheme and WSM6 coupling with BMJ scheme with the initial conditions at 0000 UTC of 18 and 19 May 2016.

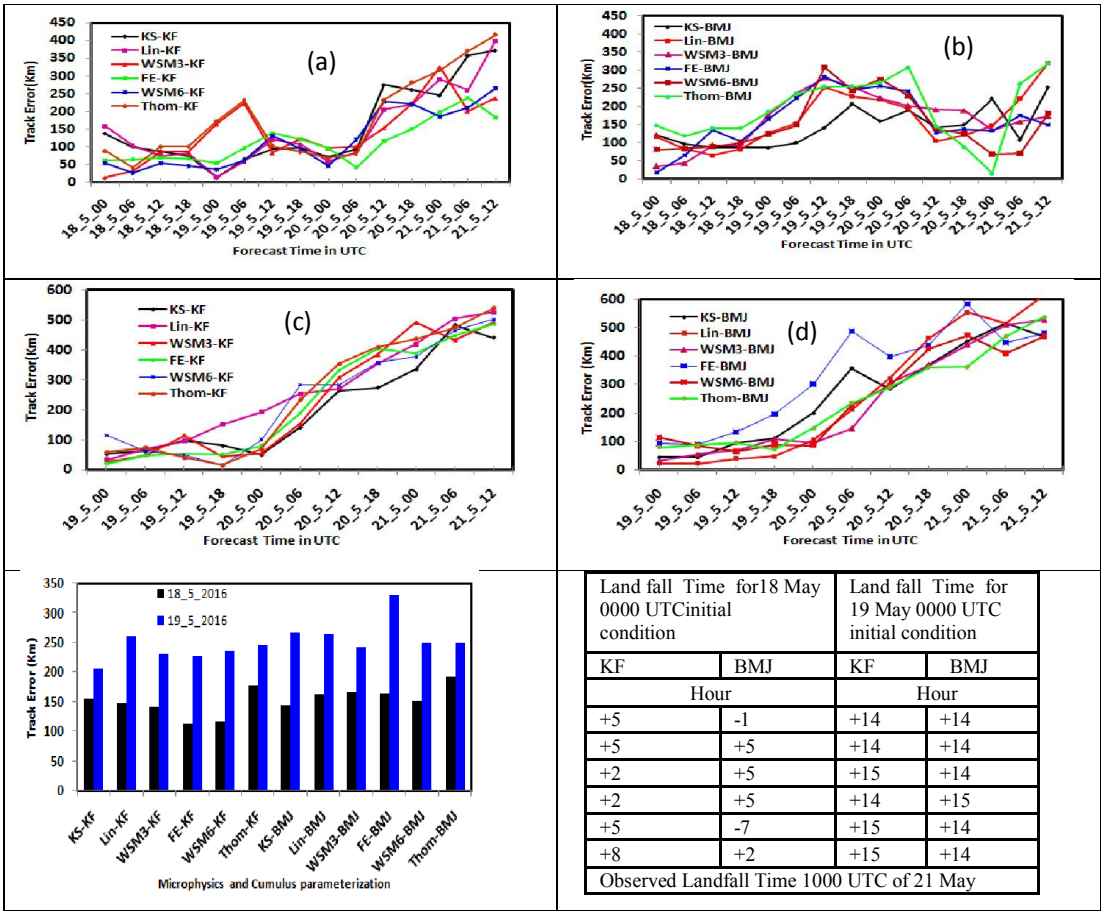

Land fall Time for18 May 0000 UTCinitial condition		Land fall Time for 19 May 0000 UTC initial condition	
KF	BMJ	KF	BMJ
Hour		Hour	
+5	-1	+14	+14
+5	+5	+14	+14
+2	+5	+15	+14
+2	+5	+14	+15
+5	-7	+15	+14
+8	+2	+15	+14
Observed Landfall Time 1000 UTC of 21 May			

Fig. 4: Model simulated track error of TC 'Roanu' with respect to IMD observed track using six different MP schemes coupling with (a-b) KF, (c-d) BMJ schemes (e) average with the initial conditions at 0000 UTC of 18 and 19 May in 2016.

The average track error (Fig. 4e) using 0000 UTC of 19 May initial conditions is higher than that with the initial conditions 0000 UTC of 18 May . KF scheme-gives the less track error than that of BMJ scheme for all MPs with the initial conditions at 0000 UTC of 18 May. The minimum average track error with respect to IMD observed results using Ferrier-KF and WSM6-KF combinations are 113 and 117 km respectively. The average track error is found maximum using Ferrier-BMJ schemes for all MPs with the initial conditions at 0000 UTC of 19 May.

4.1.5 Convective Available Potential Energy (CAPE)

The vertically integrated space averaged CAPE of region R1, R2, R3, R4 and R5 have been simulated using six different MP schemes in combination with KF and BMJ schemes and are presented in Figs.5(a-j). In R1 CAPE has shown oscillatory pattern (Fig. 5a) and is found maximum at day and minimum at night and decreased continuously for all MPs in combination with KF scheme. The simulated amount of CAPE is almost same for all MPs up to 0600 UTC of 19 May and after that WSM3 and Kessler schemes coupling with KF scheme have simulated maximum and minimum amount of CAPE all through the time of landfall of TC Roanu. The TC Roanu moved towards the Bangladesh coast due to the significant amount of CAPE has found on 20 May in R1**.**

The CAPE has found to decrease continuously in BMJ scheme coupling with all MPs up to 0000 UTC of 20 May and after that the simulated CAPE is almost zero. The vertically integrated space averaged CAPE is minimum and almost constant up to 2100 UTC of 20 May in region R2 and R3 as simulated by using KF and BMJ schemes coupling with all MPs (Fig.5(c-f)). After that the vertically integrated area averaged CAPE has increased for all MPs coupling with BMJ and KF schemes. It is observed that the maximum CAPE has been simulated for Thompson scheme and minimum for Kessler scheme in combination with KF and BMJ schemes. Significant amount of vertically integrated space averaged CAPE has been simulated in the oceanic region R4 for all MPs in combination with KF scheme (Fig.5g) and has increased with the progression of time up to 0600 UTC of 20 May. The CAPE has sharply decreased for short period of time and reached minimum at 0090 UTC of 20 May for all MPs in combination with KF scheme and after that it has increased for all combinations. In region R4 the CAPE is almost constant up to 0600 UTC of 19 May and after that it has increased for all MPs coupling with BMJ scheme (Figs.5h). WSM3 and Kessler schemes coupling with KF and BMJ schemes have simulated maximum and minimum area averaged CAPE at the oceanic region. Significant amount of vertically integrated space averaged CAPE has been simulated in the region R5 for all MPs in combination with KF scheme and has increased up to 0000 UTC of 20 May (Fig.5i) and after that it is found oscillatory in nature. It has found that maximum CAPE has been simulated at 0300 UTC of 20 May and after 1500 UTC it has decreasing trend. BMJ scheme coupling with all MPs has simulated minimum CAPE (Fig.5j) all through the simulation but they are oscillatory in nature.

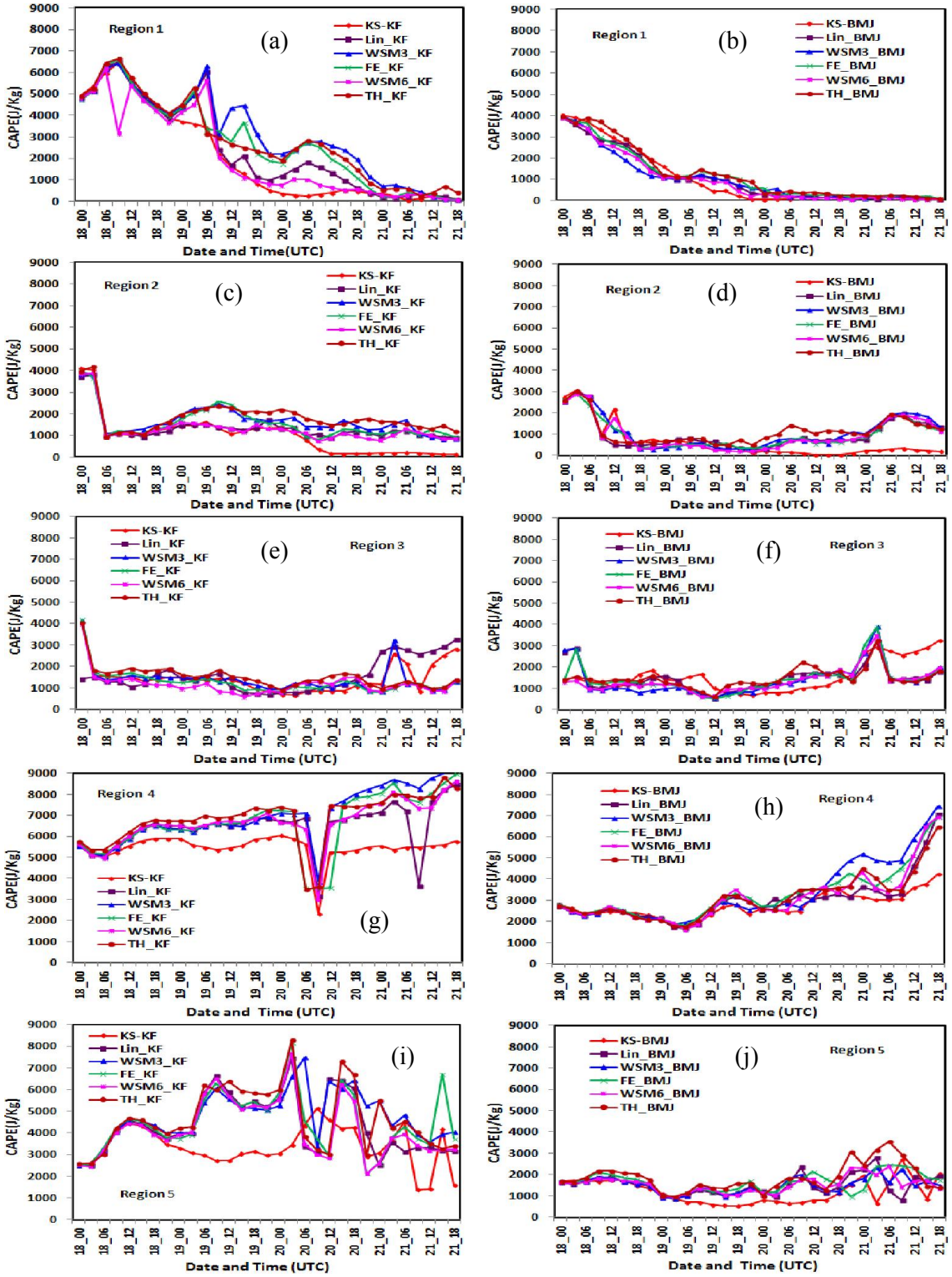

Fig.5: Model simulated CAPE of TC Mala simulated by six different MP schemes in region R1, R2, R3, R4 and R5 coupling with KF and BMJ schemes respectively.

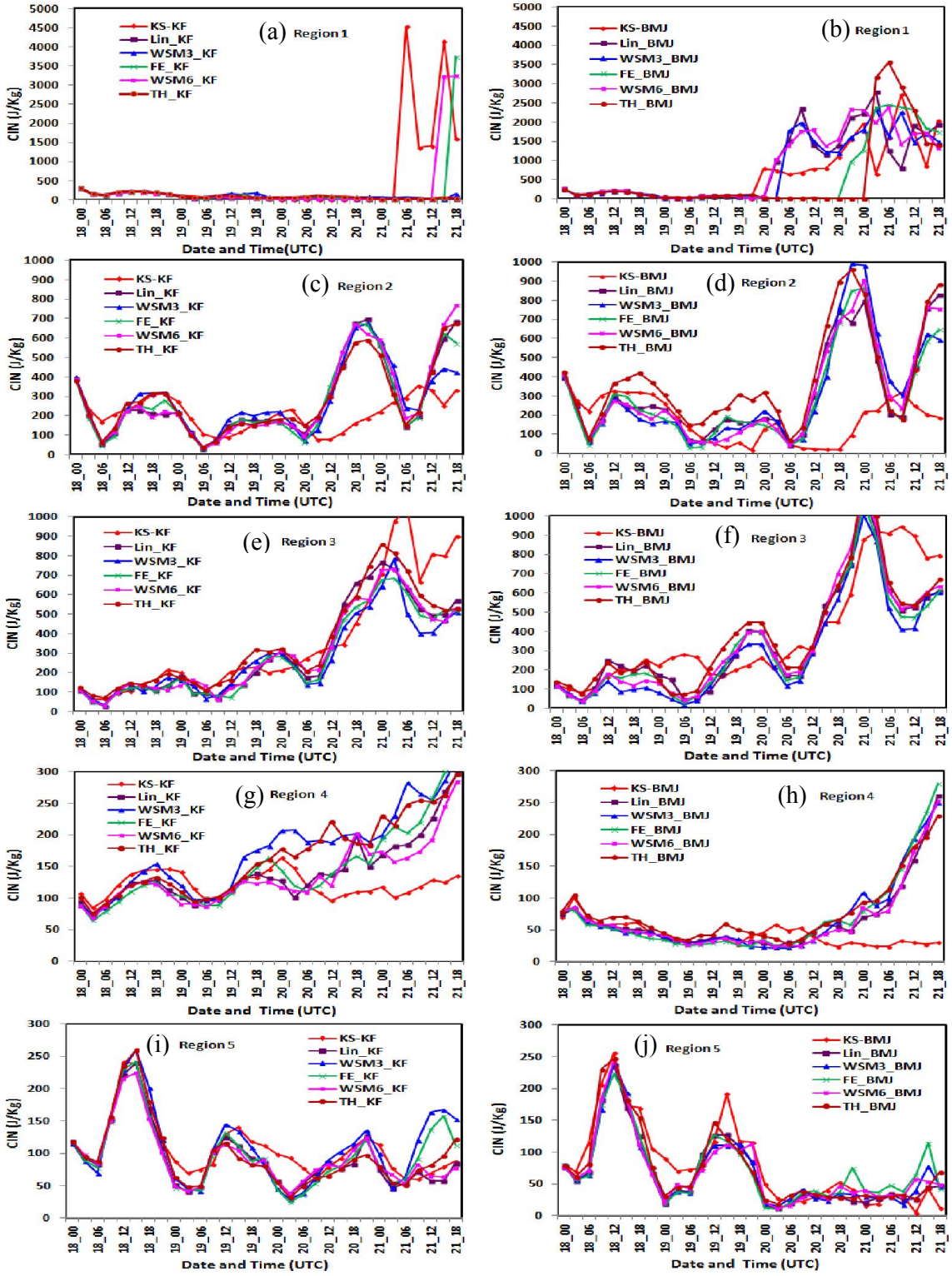

Fig 6: Vertically integrated space averaged CIN of TC Roanu in R1, R2, R3, R4 and R5 simulated by six different MP schemes coupling with KF and BMJ schemes.

4.1.6 Convective Inhibition Energy (CIN)

The vertically integrated space averaged CIN in region R1 has simulated almost zero for all MPs coupling with KF scheme up to 0300 UTC of 21 May and after that Lin et al, WSM3 and Thompson schemes have also simulated almost zero (Fig. 6a). Significant amount of CIN has been simulated by Kessler-KF, WSM6-KF and Ferrier-KF combinations after 0300, 1200 and 1500 UTC of 21 May respectively. The CIN has simulated almost zero (Fig.6b) in region R1 for all MPs coupling with BMJ scheme up to 2100 UTC of 19 May and after that significant amount of CIN is found for all MPs in combination with BMJ scheme.

The vertically integrated space averaged CIN in region R2 has been simulated at an oscillatory pattern (Figs. 6(c-d)) and maximum values are found at 1800 UTC of 18, 19 and 20 May for all MPs in combination with KF and BMJ schemes. But the peak is found minimum on 19 May when the system is nearby in region R2 and significant amount of CIN is found at 20 May i.e. the system is far from this region. The vertically integrated space averaged CIN in region R3 has been simulated at an oscillatory pattern (Figs. 6(e-f)) and maximum values are found at 1800 UTC of 18, 19 and 20 May and these values are increased with the progression of time for all MPs in combination with KF and BMJ schemes. The significant amount of vertically integrated space averaged CIN has been simulated in region R4 (Figs. 6(g-h)) by using KF and BMJ schemes but the pattern is decreasing trend for BMJ scheme up to 1200 UTC of 20 May. The CIN is found in oscillatory pattern for all MPs coupling with KF scheme up to 0000 UTC of 20 May and after that it has increased continuously in the oceanic region i.e. R4. In region R5, the area averaged CIN has been simulated to be an oscillatory for all MPs in combination with KF and BMJ schemes and crest is found at 1200 UTC of 18 19 and 20 May (Figs. 6(i-j)). The CIN is found to decrease from 18 May to 20 May for all MPs in combination with KF and BMJ schemes in R5. After 20 May, the CIN is found almost constant for all MPs coupling with BMJ schemes in R5. This decreasing tendency of CIN in R5 may be due to the intensification of TC Roanu.

4.1.7 Downward Long Wave Heat Flux (DLHF)

The vertically integrated space averaged DLHF for different MP schemes coupling with KF and BMJ schemes in different regions R1, R2, R3, R4 and R5 are presented as in Fig. 7(a-j) respectively. The space averaged DLHFs are oscillatory in nature and maximum amplitude of oscillation is positive and found at day time in different regions during the simulation period.

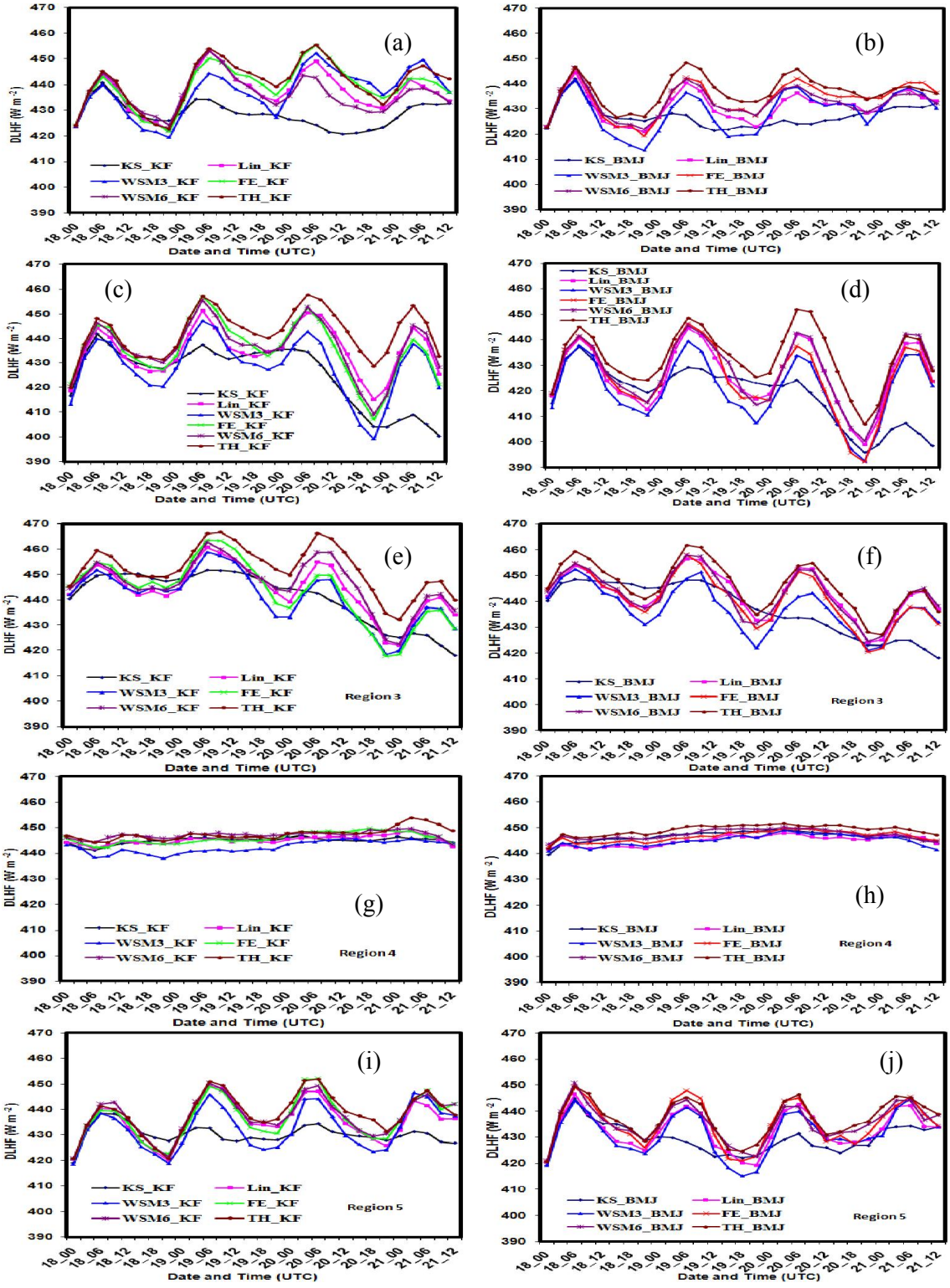

Fig.7: Model simulated DLHF of TC Roanu simulated by six different MP schemes in R1, R2, R3, R4 and R5 coupling with KF and BMJ schemes respectively.

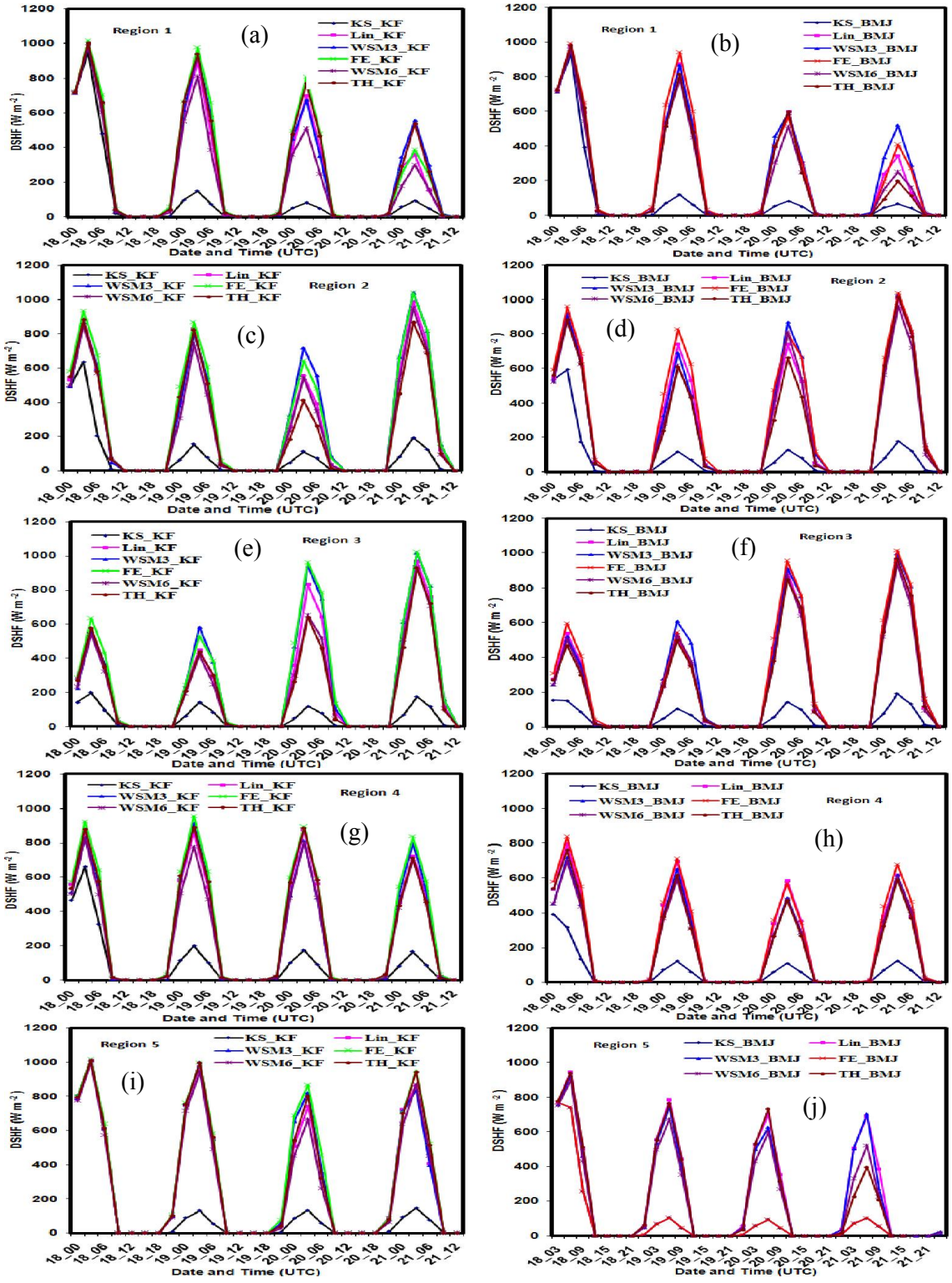

Fig. 8: Model simulated DSHF of TC Roanu simulated by six different MP schemes in R1, R2, R3, R4 and R5 coupling with KF and BMJ schemes respectively.

The Thompson and WSM3 schemes have simulated maximum and minimum DLHF respectively in all the regions. The crest and trough of DLHF in R1 (Figs. 7(a-b)) is almost similar during 18, 19 and 20 May and maximum DLHF has been simulated at 0600 – 1200 UTC and minimum is found at 1800-0000 UTC. The crest of oscillation is found to decrease on 21 May for all MPs coupling with KF and BMJ schemes. The area averaged DLHF in R2 (Figs. 7(c-d)) is almost similar on 20 May for all MP schemes in combination with KF and BMJ schemes but the trough is much stronger than that of R1. The area averaged DLHF in R3 (Figs. 7(e-f)) is almost similar during 18, 19 and 20 May and also in R1 and R2 but DLHF has decreased in R1 and T2 for all MP schemes in combination with KF and BMJ schemes but the trough is much stronger than that of R1. In the oceanic region (R4) the DLHF is almost constant during the simulated time for all MP schemes in combination with KF and BMJ schemes. Oscillation of DLHF is not found in the oceanic region. The crest and trough of DLHF in R5 (Figs. 7(i-j)) is almost similar during 18, 19 and 20 May and also same as R1. The crest of oscillation has been found to decrease on 21 May for all MPs coupling with KF and BMJ schemes.

4.1.8 Downward Short Wave Heat Flux (DSHF)

The vertically integrated space averaged DSHFs for six different MP schemes coupling with KF and BMJ schemes for regions R1, R2, R3, and R4 and R5 are presented in Figs. 8(a-j). The space averaged DSHFs are oscillatory in nature and maximum amplitude of oscillation is found at day time and minimum at night time. The oscillatory pattern is similar in nature for all MP schemes in combination with KF and BMJ schemes in all the regions. The crest of oscillation in region R1 is decreasing continuously (Fig. 8(a-b)) and minimum peak is found on 21 May in R1 for all MP schemes in combination with KF and BMJ schemes. The minimum crest is found on 20 May at R2 (Figs. 8(c-d)) and 19 May in R3 (Figs. 8(e-f)). It indicates that the DSHF is found minimum in the crossing area of TC Roanu. In the oceanic region R4, the peak is almost constant for KF but decreased in case of BMJ scheme on 20 May. The DSHF has also decreasing trend but minimum DSHF is found on 20 May.

4.1.9 Upward Moisture Heat Flux (QFX)

The vertically integrated space averaged QFXs for six different MP schemes coupling with KF and BMJ schemes for R1, R2, R3, R4 and R5 are presented in Figs. 9(a-j) and found oscillatory in nature. The crest and trough of oscillation are found at 0300 and 1800 UTC

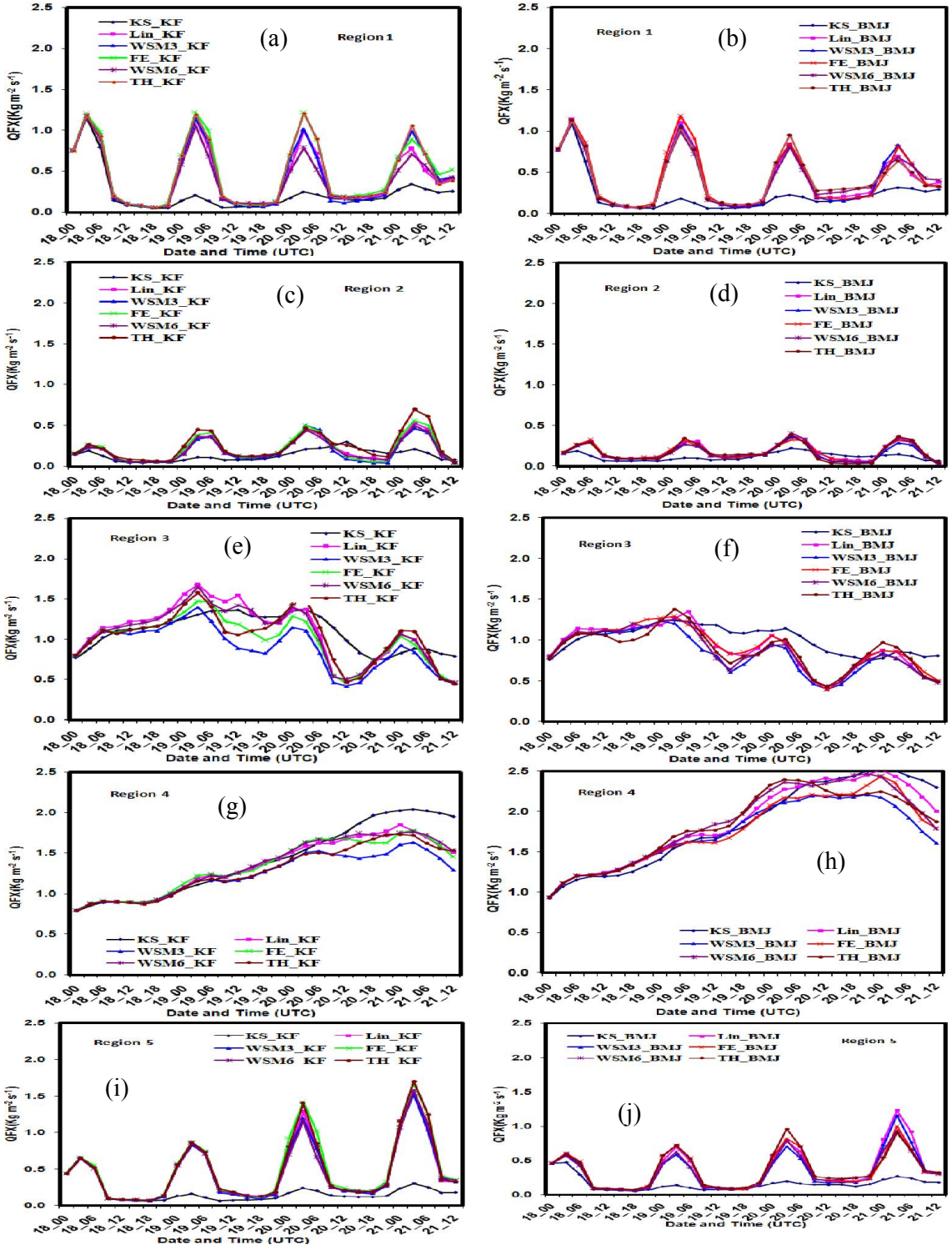

Fig. 9: Vertically integrated space averaged QFX of TC Roanu at (a-b) R1, (c-d) R2, (e-f) R3, (g-h) R4 and (i-j) R5 simulated for different MP schemes coupling with KF and BMJ schemes.

respectively in all regions and for all combination of MPs and CPs. The maximum QFX is simulated at 0300 UTC of 19 May for all MP schemes in combination with CP schemes. With the progression of time, the maximum value of QFX is decreased (Fig. 9(a-b)) and minimum value of QFX is increased for all MPs in combination with CP schemes. Kessler MP Scheme has simulated minimum QFX out of all MP schemes, but the pattern is similar. The crest of QFX for all MPs in combination with KF scheme has increased in R2 (Fig. 9(c-d)) with the progress of time. The QFX in region R3 (Fig. 9(e-f)) is found to be increased up to 19 May after that the pattern is oscillatory and has decreasing trend for all MPs in combination with KF and BMJ scheme. It is found in the oceanic region (R4) that the space averaged QFX increases continuously up to 0000 UTC of 21 May and after that it has decreased (Fig. 9(g-h)). The intensity of cyclone increased due to the increase of QFX in the oceanic region. When the cyclone crossed the coast, the QFX has decreased. In R5, the QFX is found to be oscillatory and the crest of oscillation is found to increase as shown in Fig. 9(i-j). This increase is significant for KF cumulus parameterization scheme. It is also observed that the distribution pattern of area averaged upward moisture heat flux and latent heat flux is similar in R1, R2, R3, R4 and R5 but the latent heat flux is 250 times greater than that of upward moisture heat flux.

4.1.10 Outgoing long wave radiation (OLR)

The area averaged OLR for six different MP schemes coupling with KF and BMJ schemes in R1, R2, R3, R4 and R5 is presented in Figs. 10(a-j). The Kessler scheme in combination with KF and BMJ schemes have simulated almost constant and minimum amount of OLR in R1, R2, R3, R4 and R5. It is also observed that WSM3 and Thompson schemes coupling with KF and BMJ schemes have simulated maximum and minimum amount of OLR in R1, R2, R3, R4 and R5. The simulated OLR has decreasing trend with little anomalies for all MPs except Kessler scheme coupling with KF and BMJ schemes in R1 (Figs. 10(a-b)). Due to the advancement of tropical cyclone Roanu towards Bangladesh, the amount of OLR has decreasing trend in R1.

The simulated OLR has decreasing trend with little anomalies for all MPs coupling with KF and BMJ schemes in R2 (Figs. 10(c-d)) up to 0600 UTC of 20 May and after that the OLR has increasing trend. The decreasing trend of OLR up to 0600 UTC of 20 May suggests that the TC Roanu moves towards R2 but after that it has increased in R2. The simulated OLR has decreasing trend with little anomalies for all MPs coupling with KF and BMJ schemes in R2 (Figs. 10(e-f)) up to 0000 UTC of 19 May and after that the OLR has been increased.

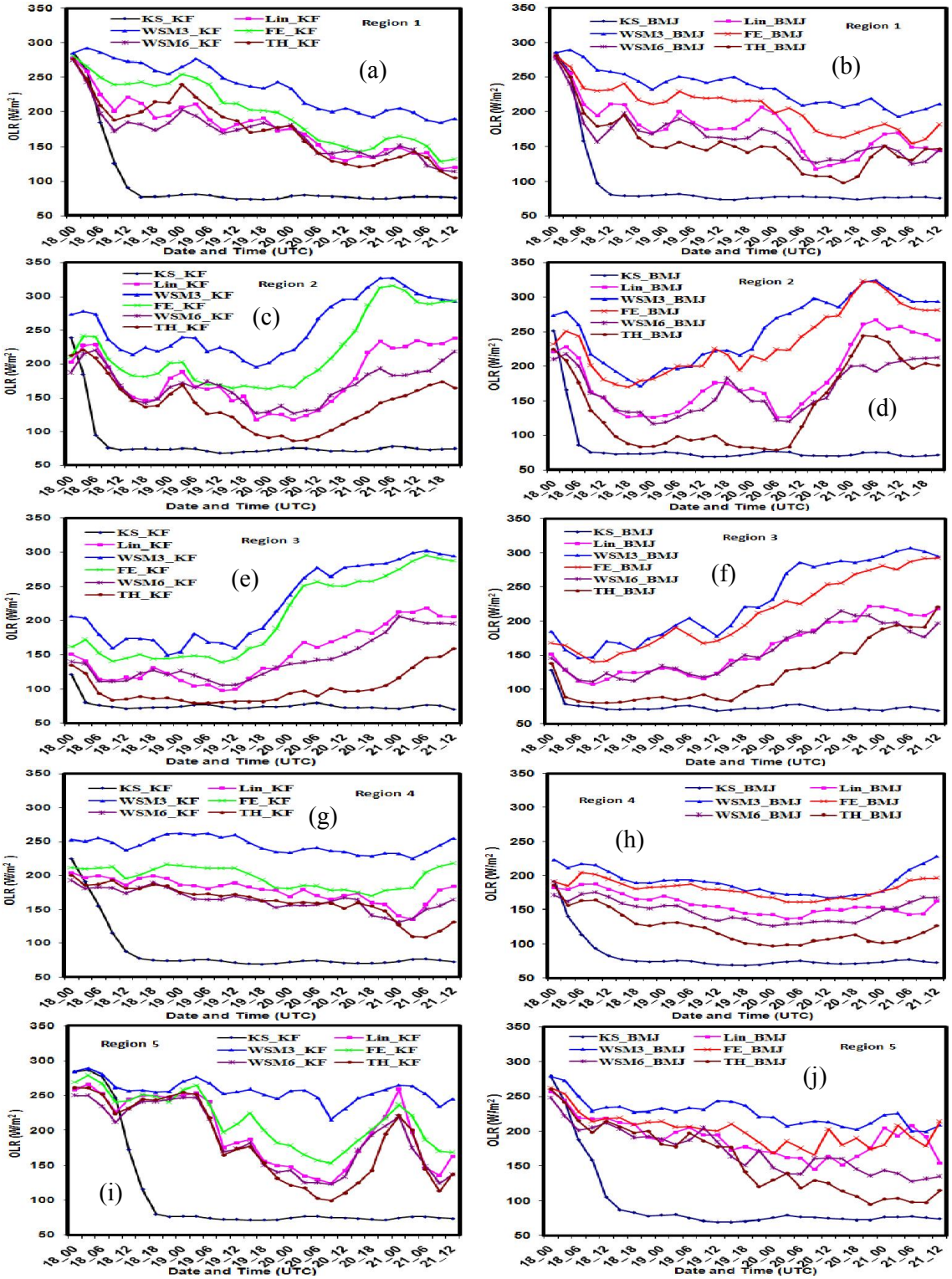

Fig. 10: Simulated OLR of TC Roanu at (a-b) R1, (c-d) R2, (e-f) R3, (g-h) R4 and (i-j) R5 for six different MP schemes coupling with KF and BMJ schemes respectively.

The decreasing trend of OLR up to 0000 UTC of 19 May suggests that the TC Roanu moves towards R3 but after that it has been increased in R3. Due to moving away of TC from R3, the OLR increases in R3. The area averaged of OLR in region R4 (Figs. 10(g-h)) has almost constant with little anomalies up to 0000 UTC of 21 May for all MPs in combination with KF and BMJ schemes. The simulated OLR is found to increase in the oceanic region when the TC Roanu is in nearby the Bangladesh coast i.e. R4. The area averaged of OLR in region R5 (Figs. 10(i-j)) has almost constant with little anomalies up to 0600 UTC of 19 May for all MPs in combination with KF and BMJ schemes. After that the OLR has decreased significantly for all MPs in combination with KF scheme up to 1200 UTC of 20 May.

4.1.11 Ground Heat Flux (GHF)

The vertically integrated space averaged GHF for six different MP schemes coupling with KF and BMJ schemes are presented for R1, R2, R3, R4 and R5 as in Figs. 11(a-j). The space averaged GHF are found to be oscillatory in nature and crest of oscillation has found at night time and trough at day time. The GHF is found to be negative in R1, R2, R3, R4 and R5 during the day time at 0000 to 1200 UTC and positive during the night time at 1500 to 0000 UTC. Kessler scheme coupling with KF and BMJ schemes have simulated positive GHF all through the simulation period except at 0300 UTC where it is found to be little negative in R1, R2, R3, R4 and R5. From Figs. 11(a-b), it is observed that the vertically integrated space averaged GHF has decreased at night time and increased during day time i.e. positive and negative values decreased at night and day respectively in R1 and R5 (Figs. 11(i-j)) during the simulation time for all MPs coupling with KF and BMJ schemes. It is observed that the vertically integrated space averaged GHF has decreased at night time and increased during day time up to 20 May in R2 (Figs. 11(c-d)) and 19 May in R3 (Figs. 11(e-f)) i.e. positive and negative values decreased at night and day respectively for all MPs coupling with KF and BMJ schemes. The amplitude of oscillation of GHF has increased on 21 May in R2 and 20-21 May in R3. This suggests that the amplitude of oscillation of GHF has increased in R2 and R3 after passing the TC Roanu in those regions.

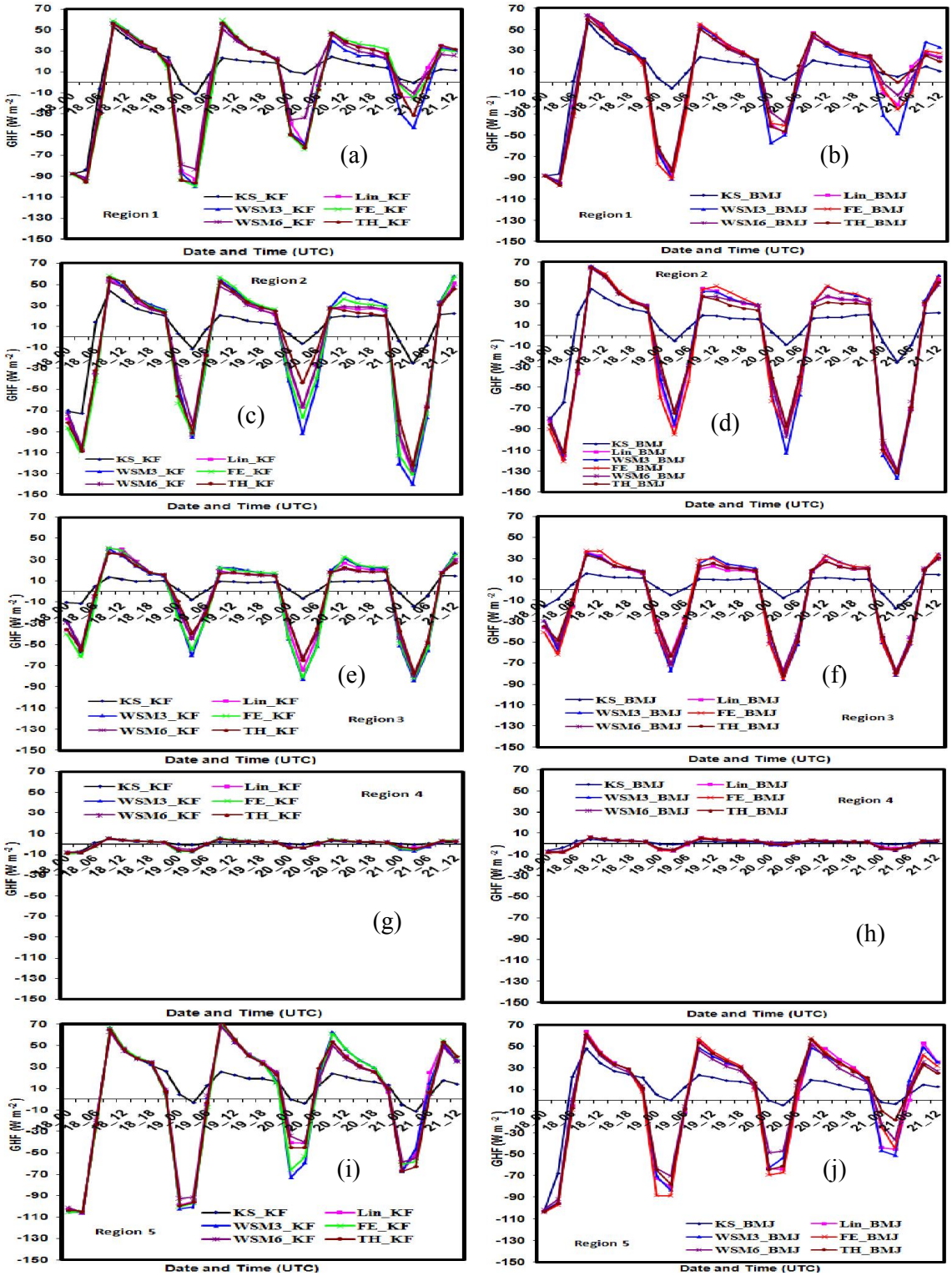

Fig. 11: Model simulated GHF of TC Roanu for six different MP schemes at (a-b) R1, (c-d) R2, (e-f) R3, (g-h) R4 and (i-j) R5 coupling with KF and BMJ schemes respectively.

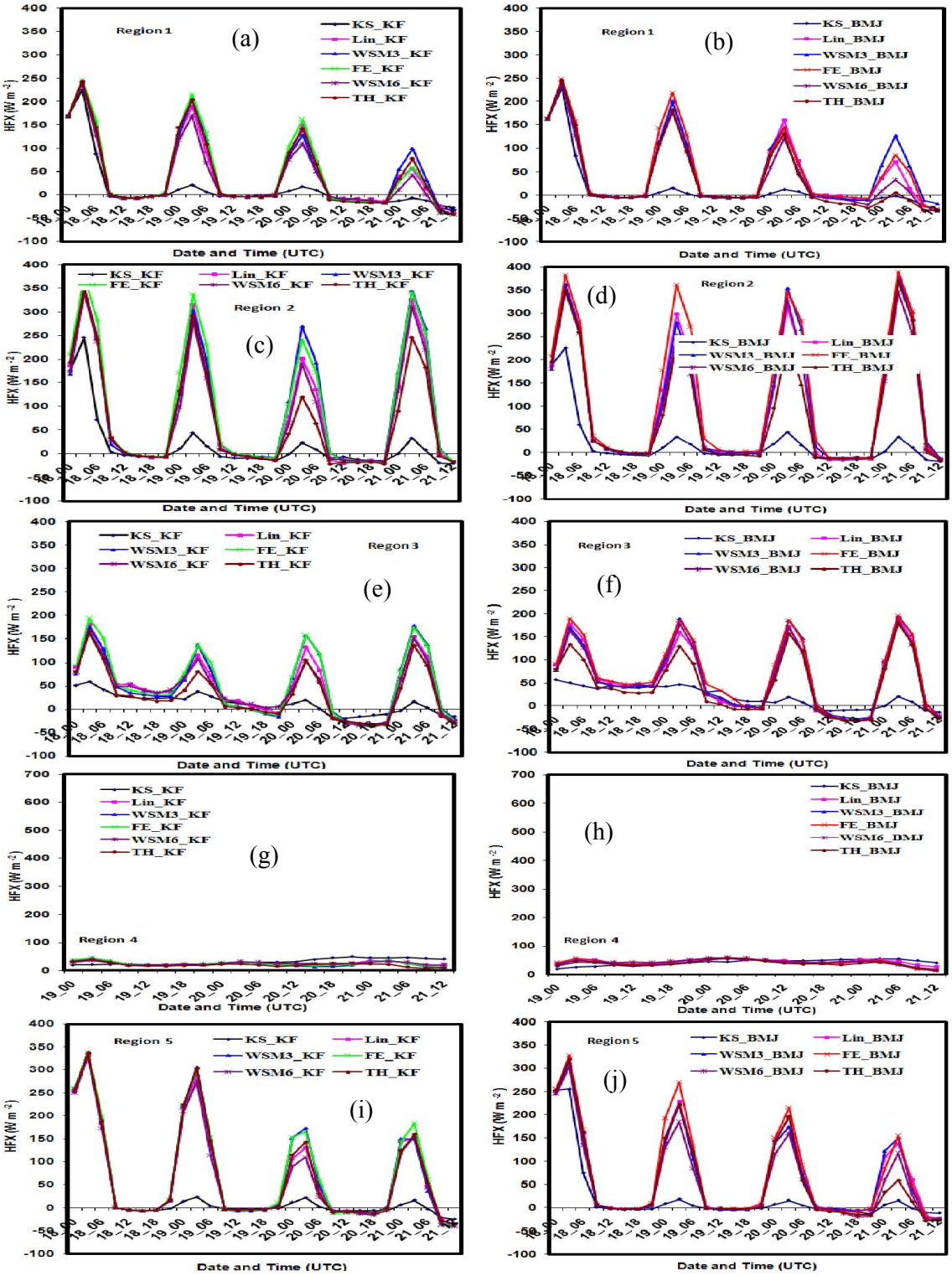

Fig. 12: Vertically integrated space averaged upward heat flux of TC Roanu simulated for six different MPs at (a-b) R1, (c-d) R2, (e-f) R3 , (g-h) R4 and (i-j) R5 coupling with KF and BMJ schemes respectively.

This suggests that the amplitude of oscillation of GHF has decreased as the TC Roanu moves towards R1. The amplitude of oscillation of GHF has almost zero for all MPs coupling with KF and BMJ schemes in the oceanic region i.e. R4 (Figs. 11(g-h)).

4.1. 12 Upward Heat flux

The vertically integrated space averaged upward heat fluxes for six different MP schemes coupling with KF and BMJ schemes for R1, R2, R3, R4 and R5 are presented as in Figs. 12(a-j). The space averaged upward heat flux is oscillatory in nature and maximum amplitude of oscillation has found at day time and minimum at night time. The oscillatory pattern is similar in nature for all MP schemes in combination with KF and BMJ schemes in all the regions except oceanic region i.e. R4. The crest of oscillations in R1 (Figs. 12(a-b)) and R5 (Figs. 12(i-j)) has decreased continuously and minimum peak is found on 21 May for all MPs in combination with KF and BMJ schemes. The upward heat flux has decreased and reached minimum on 20 May at R2 (Figs. 12(c-d)) and 19 May in R3 (Figs. 12(e-f)) after that it increased in both the regions. It suggests that the upward heat flux has decreasing tendency in an area where the TC Roanu has crossed. In the oceanic region i.e. R4 (Figs. 12(g-h)), the space averaged upward heat flux is almost constant for KF and BMJ schemes during the cyclonic period.

4.2 Tropical Cyclone Mala

4.2.1 Synoptic situation of Tropical Cyclone Mala

A low pressure area formed over Southeast Bay of Bengal and adjoining south Andaman Sea on 23 April 2006. It moved west-northwesterly direction initially and intensified into a well-marked low over the same area. It intensified further into a depression at 0300 UTC of 24 April 2006 over Southeast Bay when its central location was at about 9.5°N and 90.5°E. The system moved slightly westwards and intensified into a deep depression (DD) at 0900 UTC of 24 April 2006 over Southeast Bay and adjoining areas and located at about 9.5°N and 90.0°E. The DD then moved slightly northwestwards and intensified into a cyclonic storm (CS) 'Mala' at 1200 UTC of 25 April 2006 over Southeast Bay and adjoining areas. At this stage, the estimated central mean sea level pressure (MSLP) of the system was about 996 hPa, the maximum estimated wind speed was about 18 m/s and the central location was about 10.0°N and 89.5°E. The CS 'Mala' then moved further north-northwestwards, intensified further and its central MSLP lowered to 994 hPa, the maximum wind speed increased to 23 m/s and the centre located to about 11.0°N and 89.0°E at 0000 UTC of 26 April. Then, it moved north-northeastwards and intensified into a severe cyclonic storm (SCS) 'Mala' at 0300 UTC of 27 April over East-central Bay and adjoining areas with the central MSLP of 990 hPa and the maximum wind speed of 28 m/s. At 1200 UTC of 27 April, the system attained into a very severe cyclonic storm (VSCS) with the central MSLP of 984 hPa, the MWS of 33 m/s and the central location at about 13.0°N and 90.5°E. The VSCS 'Mala' moved in the same direction and intensified further and at 0900 UTC of 28 April its central MSLP lowered to 954 hPa, the MWS increased to 51 m/s when its central location was at about 15.0°N and 92.3°E. Then, the VSCS 'Mala' moved continuously northeastwards afterwards without changing intensification and finally crossed Arakan coast of Myanmar about 100 km south of Sandoway near to 19.0°N and 96.0°E at 0700 UTC of 29 April. After landfall the system weakened gradually by giving precipitation over Arakan coast and adjoining land areas of Myanmar.

4.2.2 Intensity of TC Mala

The intensity prediction of TC Mala considering 3-hourly central sea level pressure (CSLP) and (e-h) associated MWS at 10 m level using different MP schemes coupling with CP schemes is presented in Fig. 13(a-d). Fig. 13(a-b) shows the simulated CSLP for six different MP schemes in combination with two different CP schemes and two different initial

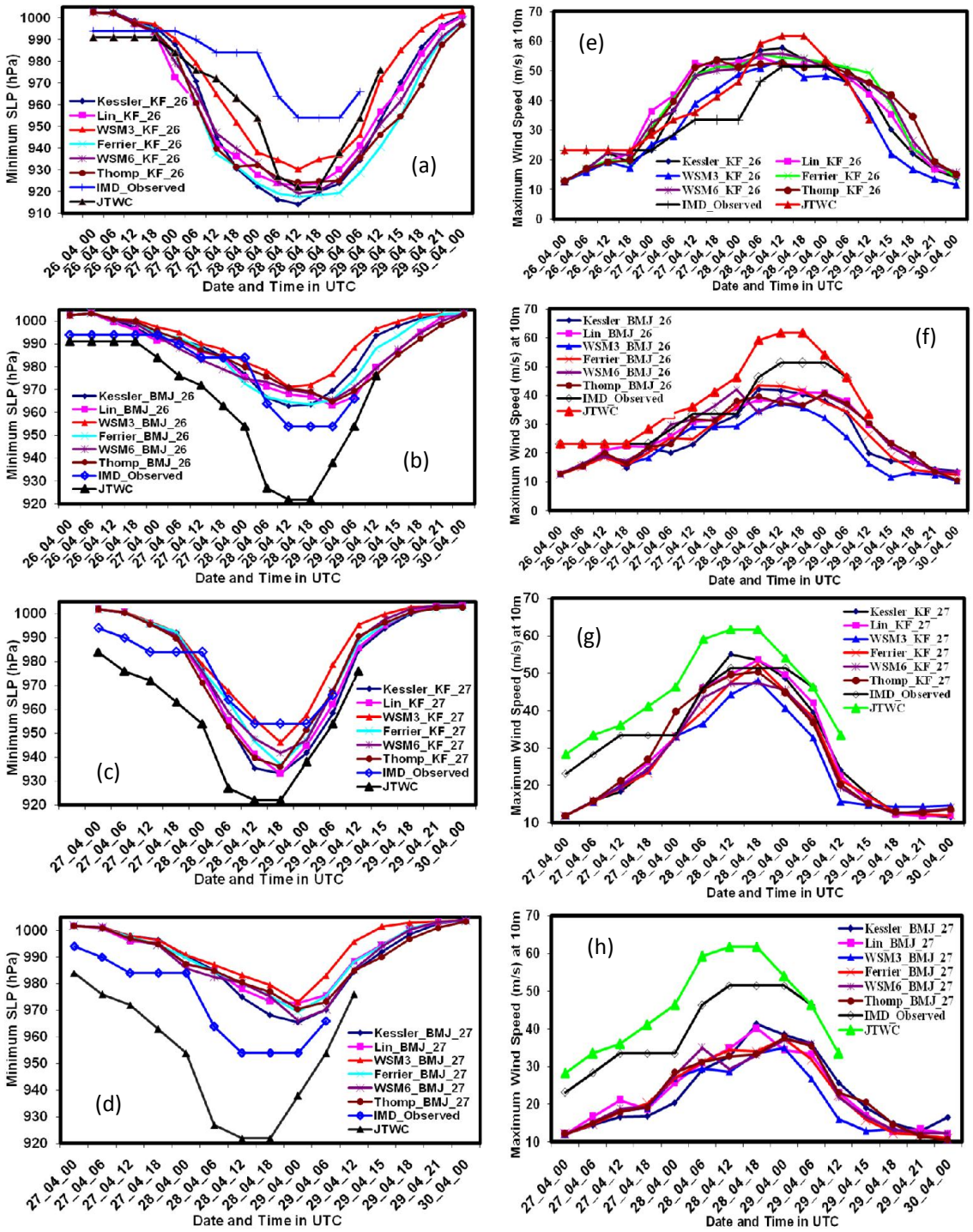

Fig. 13: Model simulated and IMD observed (a-d) minimum CSLP (hPa) and (e-h) maximum sustained wind at 10m level of TC Mala using six different MP schemes coupling with KF and BMJ schemes with 0000 UTC of 26 and 27 April 2006 initial conditions.

Conditions at 0000 UTC of 26 and 27 April 2006. The simulated intensity in terms of CSLP for all MP schemes in combination with KF scheme are much higher than that of BMJ

scheme with the initial condition at 0000 UTC of 26 and 27 April. IMD observed intensity (954 hPa, 51.44 m s^{-1}) is much lower than that of JTWC intensity (922 hPa, 61.73 m s^{-1}) in terms of pressure fall and 10 m level sustained wind. The simulated pressure fall with the 0000 UTC of 26 April initial condition for all MP schemes in combination with KF scheme are close to JTWC observed results but higher than that of IMD observed results. The simulated CSLP for all MP schemes in combination with KF scheme lies between IMD and JTWC observed results with the initial conditions 0000 UTC of 27 April. BMJ scheme simulated pressure drop and wind speed in combination with all MP schemes are much lower than that of IMD and JTWC observed pressure and MWS with the initial conditions of 0000 UTC of 26 & 27 April. The wind speed simulated at 10 m level for all MP schemes coupling with KF scheme with the initial conditions of 0000 UTC of 26 and 27 April are lower than that of JTWC observed wind speed and higher than that of IMD observed wind speed. BMJ scheme coupling with all MP schemes have simulated wind speed at 10 m level are much lower than that of IMD and JTWC observed wind with the initial condition at 0000 UTC of 26 and 27 April. The simulated wind speeds for all MP schemes in combination of KF scheme at 10 m level are almost equal to IMD observed wind speed.

4.2.3 Track of TC Mala

The observed and simulated track for the period of 96-h and 72-h of TC Mala for different MP schemes are displayed in Fig. 14(a-d). The track forecasts have shown reasonably accurate for different experiments i.e., up to the landfall time (0700 UTC of 29 April 2006). For all combination of MP and CP schemes the model captured the N-NE movement with the initial conditions at 0000 UTC of 26 and 27 April 2006. The significant deviations in tracks are observed among different microphysical schemes in combination with KF scheme with the initial condition of 0000 UTC of 26 April. Kessler and WSM3 schemes in combination with KF and BMJ schemes provide most deviated track with the initial condition of 0000 UTC of 26 April. Kessler scheme deviated towards left and WSM3 deviated towards right from the IMD and JTWC track. At the time of landfall Ferrier and Thompson schemes in combination with KF scheme and Lin *et al.* and WSM6 scheme in combination with BMJ schemes simulate less deviated track with the initial condition of 0000 UTC of 27 April. All MPs coupling with KF and BMJ schemes captured the eastward movement of TC Mala for the initial condition of 0000 UTC of 27 April. The landfall time was delayed by 4-9 h by using the initial condition of 0000 UTC 26 April.

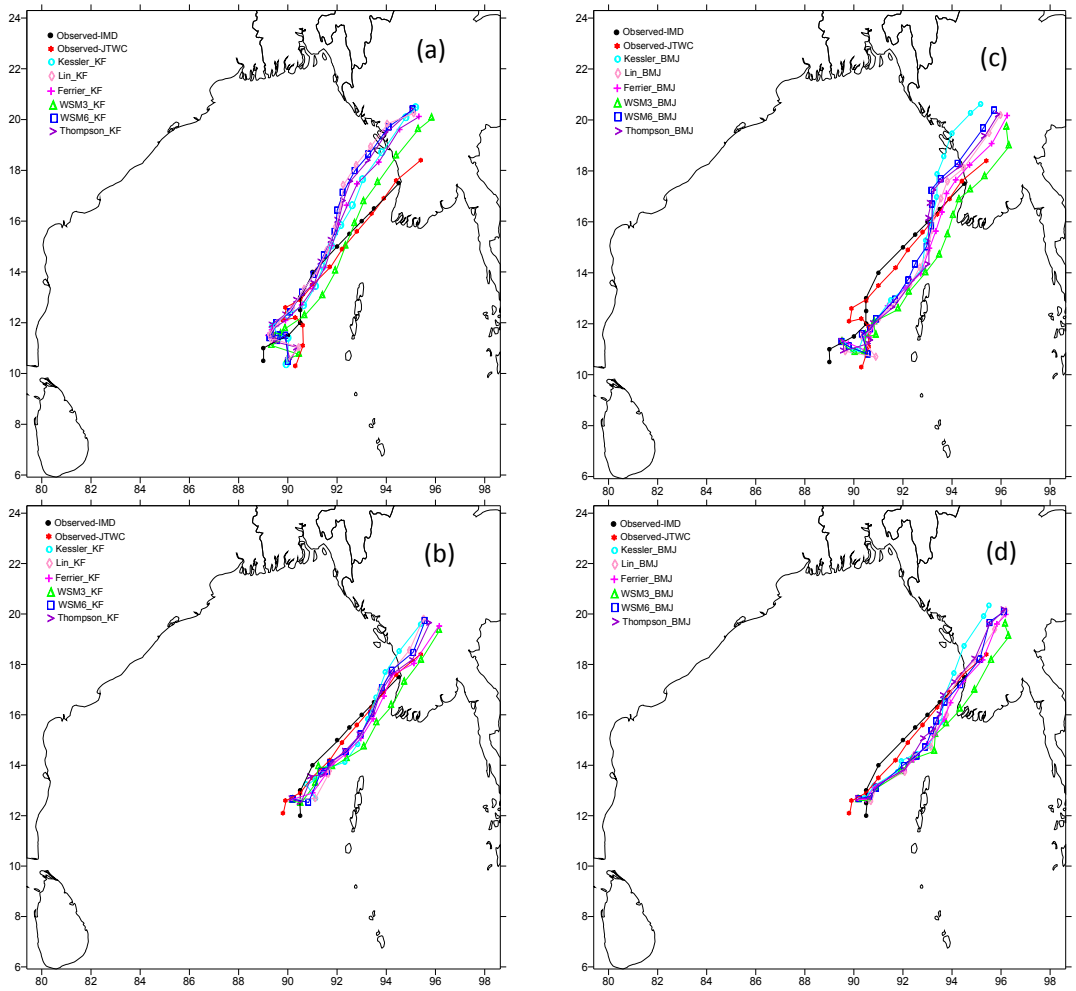

Fig. 14: Model simulated, IMD and JTWC observed tracks of TC Mala using six different MP schemes coupling with (a-b) KF and (c-d) BMJ schemes with the initial conditions at 0000 UTC of 26 and 27 April 2006.

The simulated landfall time by using six different MP schemes coupling with KF scheme are 1200, 1300, 1000, 1300, 1400 and 1500 UTC respectively but when coupling with BMJ scheme are 0700, 1000, 0300, 0900, 1200 and 1200 UTC respectively. The observed landfall time almost match with the model simulated landfall time with the initial condition at 0000 UTC of 27 April. Simulated landfall time by using Kessler, Lin *et al*., WSM3, Ferrier, WSM6 and Thompson schemes coupling with KF scheme are 0900, 0700, 0400, 0700, 0700 and 0900 UTC respectively. But when these MP schemes are coupled with BMJ scheme, the landfall time are 0900, 0900, 0000, 0600, 0700 and 0900 UTC respectively. It suggests that

the model simulated landfall times are close to the observation with the delayed initial condition.

4.2.4 Track Error of TC Mala

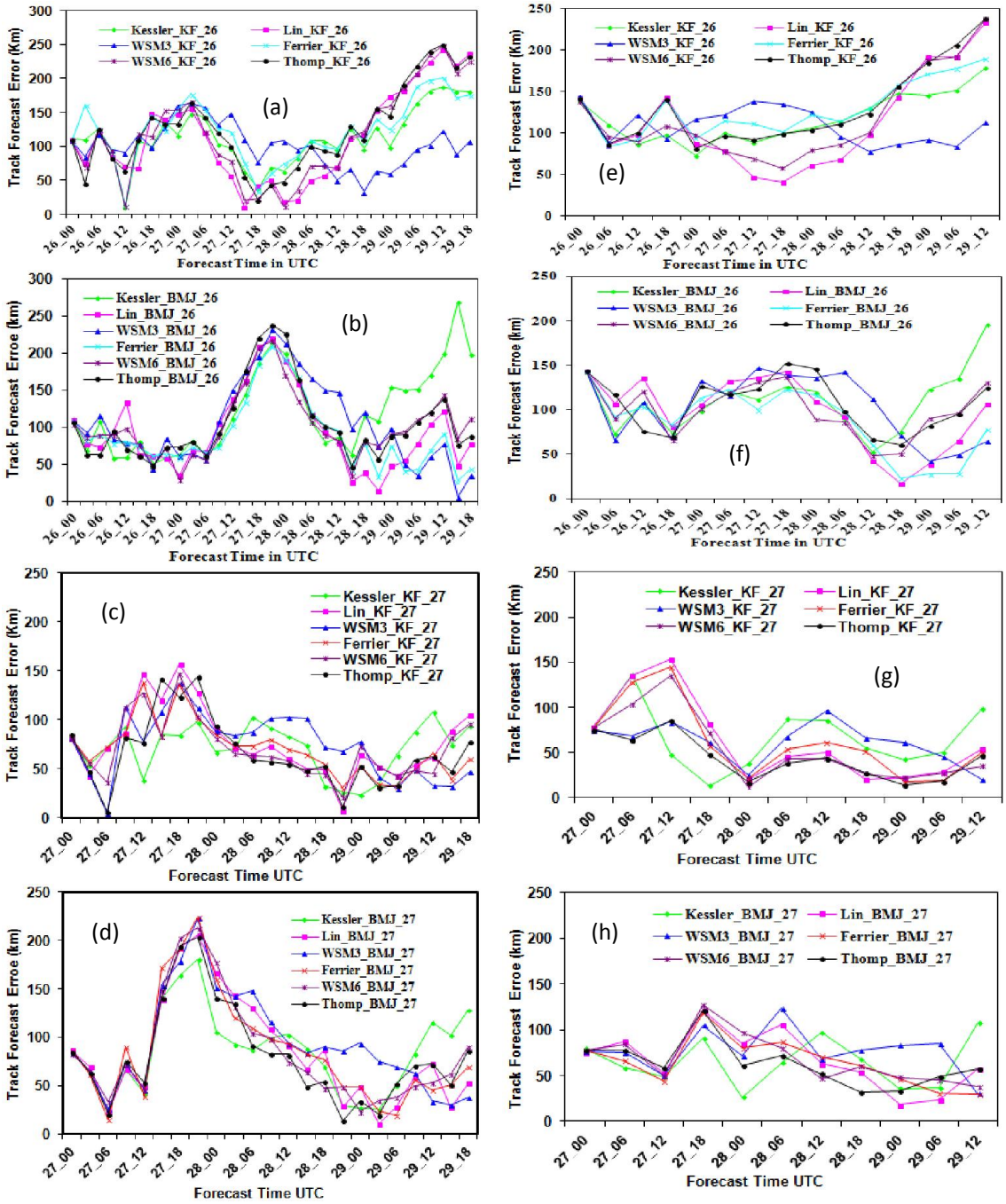

Fig. 15: Model simulated track error of TC Mala with respect to (a-d) IMD and (e-h) JTWC observed track using six different MP schemes coupling with KF and BMJ schemes with the initial conditions of 0000 UTC of 26 and 27 April 2006.

The track error has been calculated on the basis of IMD observed track and JTWC track. The track error with respect to IMD track and JTWC observed tracks are presented in Figs. 15(a-d) and 15(e-h) respectively. The error was not systematic for JTWC and IMD track by using. KF and BMJ schemes with the initial conditions at 0000 UTC of 26 and 27 April but the track error on 27 April was very much less compared to the initial condition of 26 April. Thompson-KF combination simulated most deviated track and Ferrier-BMJ simulated less deviated track with respect to IMD and JTWC track with the initial condition at 0000 UTC of 26 April. Again Thompson-KF combination simulated less deviated track and WSM3-BMJ simulated most deviated track with respect to IMD and JTWC track with the initial condition at 0000 UTC of 27 April. The track error was less in comparison with JTWC track at the time of landfall using Ferrier and Thompson schemes coupling with KF scheme and Ferrier-BMJ in comparison with IMD observed track with the initial condition at 0000 UTC of 27 April 2006. At the time of landfall the track error almost equal was using Ferrier and Thompson schemes coupling with BMJ scheme. The average track error using 0000 UTC of 26 initial conditions was higher than that of 0000 UTC of 27 April initial condition as presented in Fig. 15(a-b). KF scheme gives the less track error than that of BMJ scheme for all MPs with the initial condition at 0000 UTC of 27 April. The minimum average track error was found 44 km and 66 km for Thompson–KF with respect to JTWC and IMD observed result. The average track error was minimum using WSM6-KF combination.

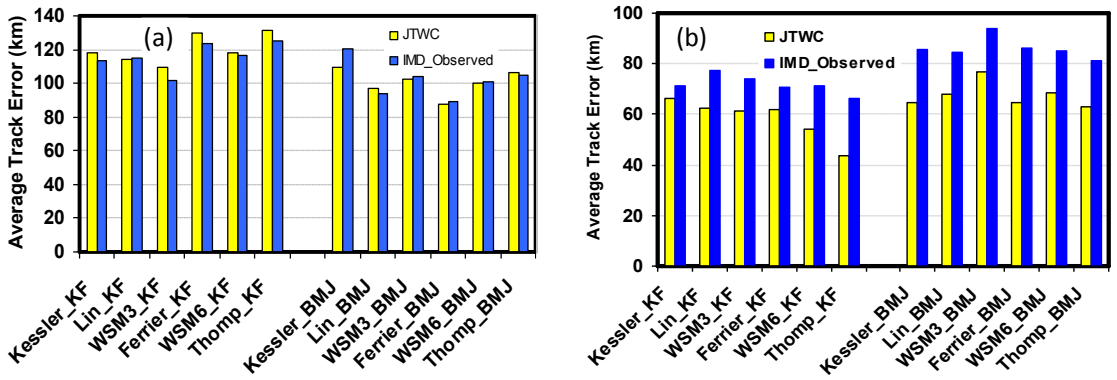

Fig. 16: Model simulated average track error of TC Mala with respect to IMD and JTWC observed track with the initial conditions of 0000 UTC of (a) 26 and (b) 27 April 2006 using six different MP schemes coupling with KF and BMJ schemes.

4.2.5 Convective Available Potential Energy (CAPE)

The vertically integrated space averaged CAPE has been simulated in R1, R2, R3, R4 and R5 using six different MP schemes in combination with KF and BMJ schemes and is presented in Figs. 17(a-j). Kessler scheme has simulated minimum CAPE coupling with KF and BMJ schemes in R1, R2, R3, R4 and R5 and decreased with the progression of time. In R1, the CAPE is found to decrease continuously (Fig. 17a) in KF scheme coupling with all MPs up to 0000 UTC of 28 April and after that the simulated CAPE is found to increase at 0600 UTC of 28 April becoming zero afterwards. The CAPE is found to increase up to 0900 UTC of 26 April and again from 1200 UTC of 26 April to 0300 UTC of 27 April after that it has decreased continuously in R1 for all MPs coupling with BMJ scheme. The WSM3 and Kessler schemes coupling with BMJ scheme have simulated maximum and minimum amount of CAPE since 1800 UTC of 27 April up to the time of landfall of TC Mala. The vertically integrated space averaged CAPE in R2 (Fig. 17c) is decreased since 0600 UTC of 26 April to 0900 UTC of 28 April and after that it has irregular trend. The CAPE is found significantly higher and almost constant and in oscillatory in nature for BMJ scheme coupling with all MPs except Kessler scheme up to 1200 UTC of 28 April and after that it is found to increase in R2 (Fig. 17d). The vertically integrated space averaged CAPE is found to decrease continuously for Kessler scheme coupling with BMJ scheme from 0600 UTC of 26 April up to 1200 UTC of 29 April in R2. The CAPE has increased in R3 (Fig. 17e) up to 0600 UTC of 28 April in Thompson scheme and up to 2100 UTC of 28 April for all other MP schemes coupling with KF scheme. The CAPE is found oscillatory in nature after 0600 UTC of 28 for Thompson-KF combination and after 0600 UTC of 29 April for Lin-KF and WSM6-KF combinations. The simulated CAPE is found to increase up to 2100 UTC of 28 April for Lin, WSM3, WSM6 and Thompson schemes coupling with BMJ scheme in R3 (Fig. 17f) and decrease continuously for Kessler-BMJ and Ferrier-BMJ combinations.

The space averaged CAPE is almost constant in R4 (Figs. 17(g-h)) up to 0000 UTC of 28 April for all MPs in combination with KF and BMJ scheme and after that it has increased for all combinations in the oceanic region. In R4, Thompson and Kessler schemes coupling with KF and BMJ schemes have simulated maximum and minimum CAPE during the period. The space averaged CAPE has been decreased in R5 (Fig. 17i) up to 2100 UTC of 26 April and then increased up to 0900 UTC of 27 April for all MPs in combination with KF scheme. After 0900 UTC the CAPE has decreased continuously for all MPs in combination with KF

scheme. The CAPE has been simulated minimum in R5 (Fig. 17j) for all MPs coupling with BMJ scheme and decreased continuously all through the simulation time.

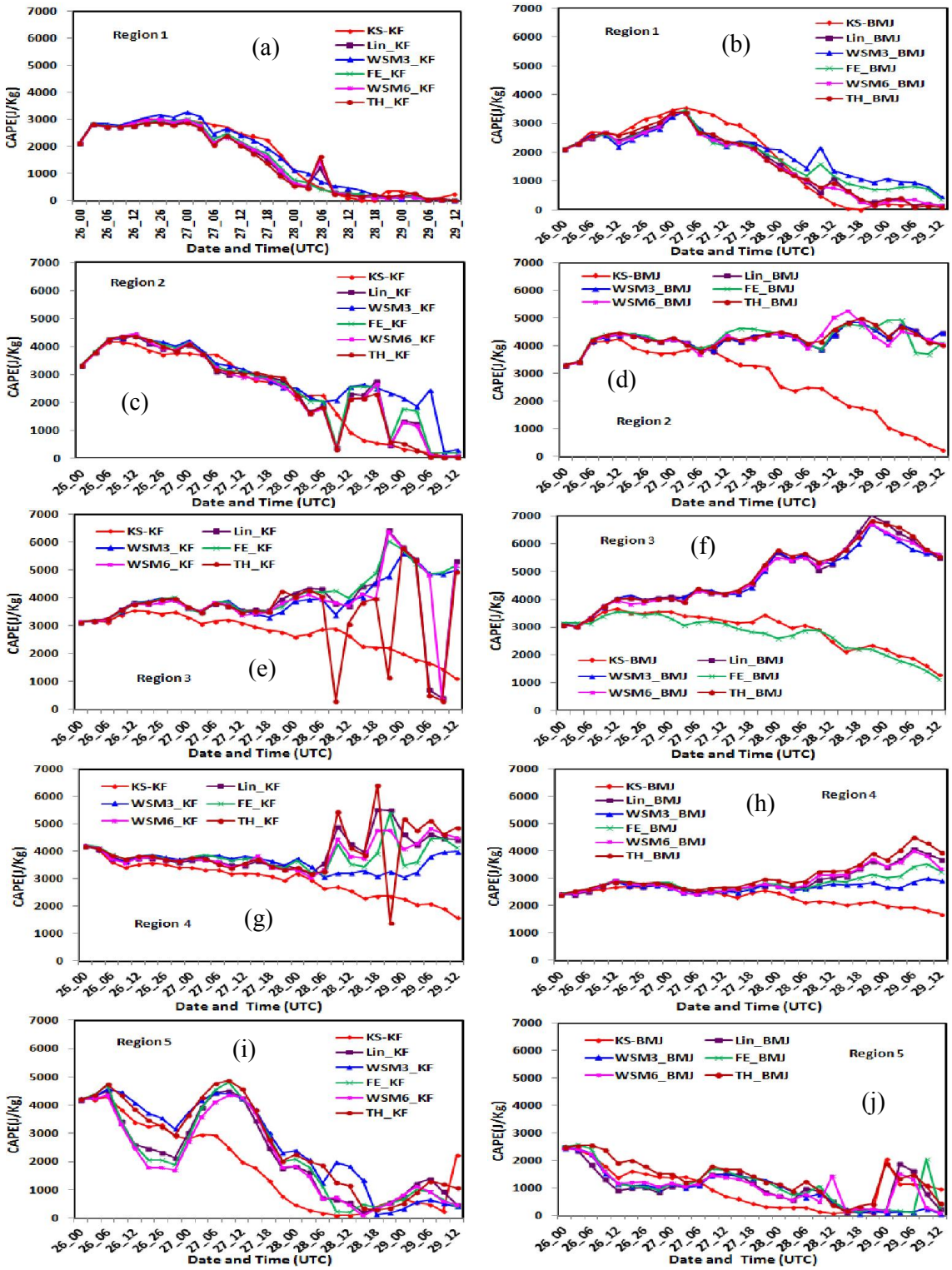

Fig. 17: Model simulated CAPE of TC Mala in regions (a-b) R1, (c-d) R2, (e-f) R3, (g-h) R4 and (i-j) R5 by six different MP schemes coupling with KF and BMJ schemes respectively.

4.2.6 Convective Inhibition Energy (CIN)

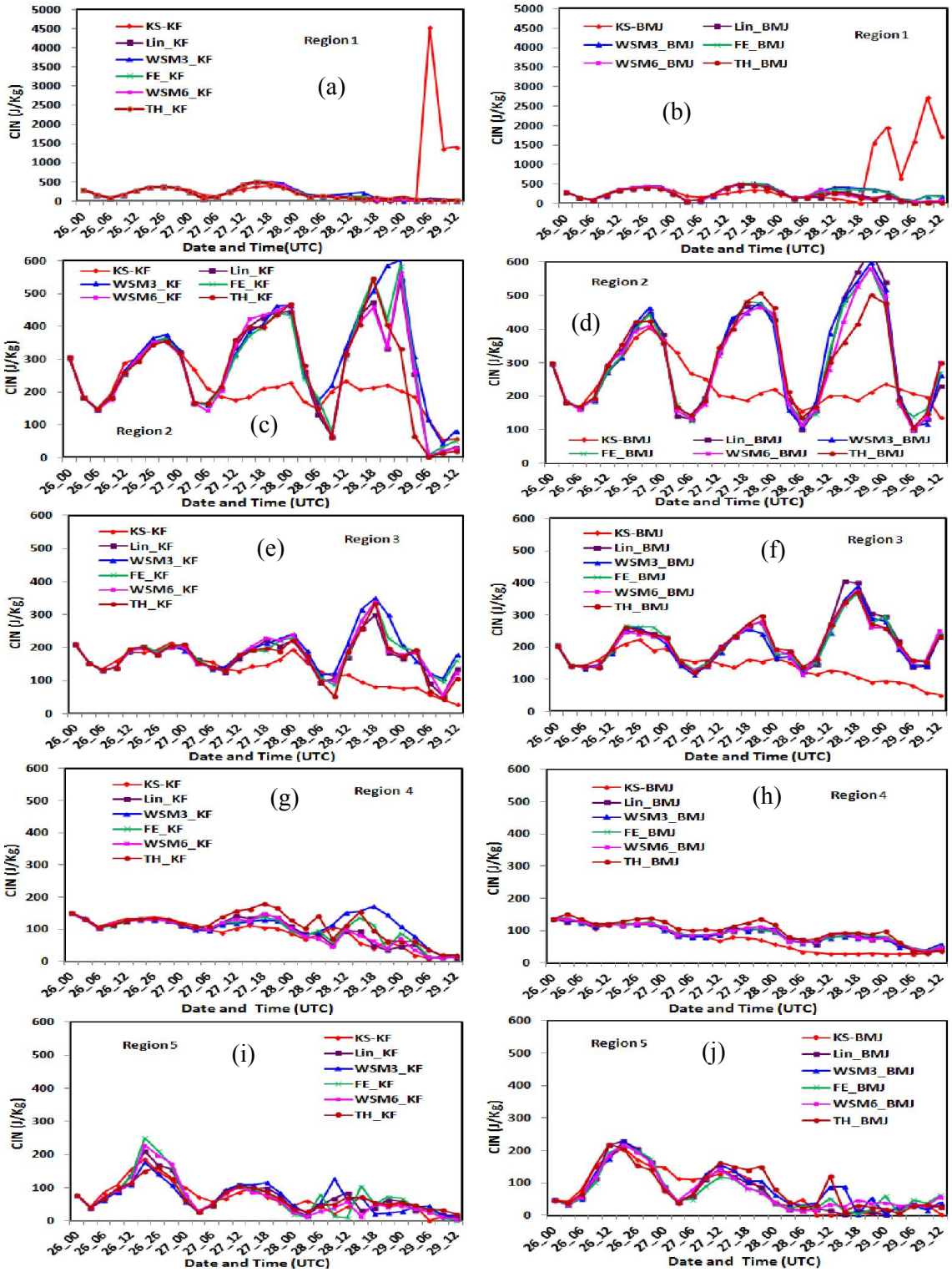

Fig. 18: Vertically integrated space averaged CIN of TC Mala in (a-b) R1, (c-d) R2, (e-f) R3, (g-h) R4 and (i-j) R5 by six different MP schemes coupling with KF and BMJ schemes respectively.

The vertically integrated space averaged CIN have been simulated in R1, R2, R3, R4 and R5 using six different MP schemes in combination with KF and BMJ schemes and is presented in Figs. 18(a-j). Kessler scheme has simulated minimum CIN coupling with KF and BMJ schemes in R1, R2, R3, R4 and R5 and CIN is decreased with the progression of time. The significant amount of CIN is found in R1 for all MPs coupling with KF scheme. The CIN in R1 is in oscillatory in nature for all MP schemes coupling with KF (Fig. 18a) and BMJ (Fig. 18b) schemes and crest is found at 1800 UTC and trough at 0600 UTC on 26 and 27 April for KF combination and 26-28 April for BMJ combination. The CIN is almost zero after 0300 UTC of 28 April in R1. The space averaged CIN is found an oscillatory pattern in R2 (Fig. 18(c-d)) and maximum crests are found at 0000 UTC of 27, 28 and 29 April for all MPs in combination with KF and BMJ schemes. The amplitude of oscillation is found to increase with the progression of time in R2. The space averaged CIN is found an oscillatory pattern in R3 (Fig. 18(e-f)) and maximum crest are found at 1800 UTC of 27, 28 and 29 April for all MPs in combination with KF and BMJ schemes. The amplitude of oscillation is found to increase with the progression of time in R3. The space averaged CIN is found almost constant with little oscillation in R4 (Figs. 18(g-h)) for all MPs coupling with KF and BMJ schemes and is found to decreased continuously in the oceanic region i.e. R4. In R5, the area averaged CIN is found an oscillatory for all MPs in combination with KF and BMJ schemes and crest is found at 1800 UTC of 26 and 27 April (Figs. 18(i-j)) with decreasing amplitude. After 0000 UTC of 28 April the CIN is found almost zero for all MPs coupling with KF and BMJ schemes in R5. This decreasing tendency of CIN in R5 indicates the movement of TC Roanu towards this region.

4.2.7 Downward Long Wave Heat Flux (DLHF)

The vertically integrated space averaged DLHFs for six different MP schemes coupling with KF and BMJ schemes in different regions R1, R2, R3, R4 and R5 are presented in Figs. 19(a-j) respectively. The space averaged DLHFs are oscillatory in nature and maximum amplitude of oscillation is found at day time in different regions during the simulation period. Kessler scheme has simulated minimum DLHF in all regions and DLHF is found to decrease continuously during the simulation period. The crest and trough of DLHF in R1 (Figs. 19(a-b)) are decreasing in nature, and maximum and minimum DLHF have been simulated during 0600–1200 and 1800-0000 UTC respectively. The crest of oscillation is found to decrease on 29 April for all MPs coupling with KF and BMJ schemes.

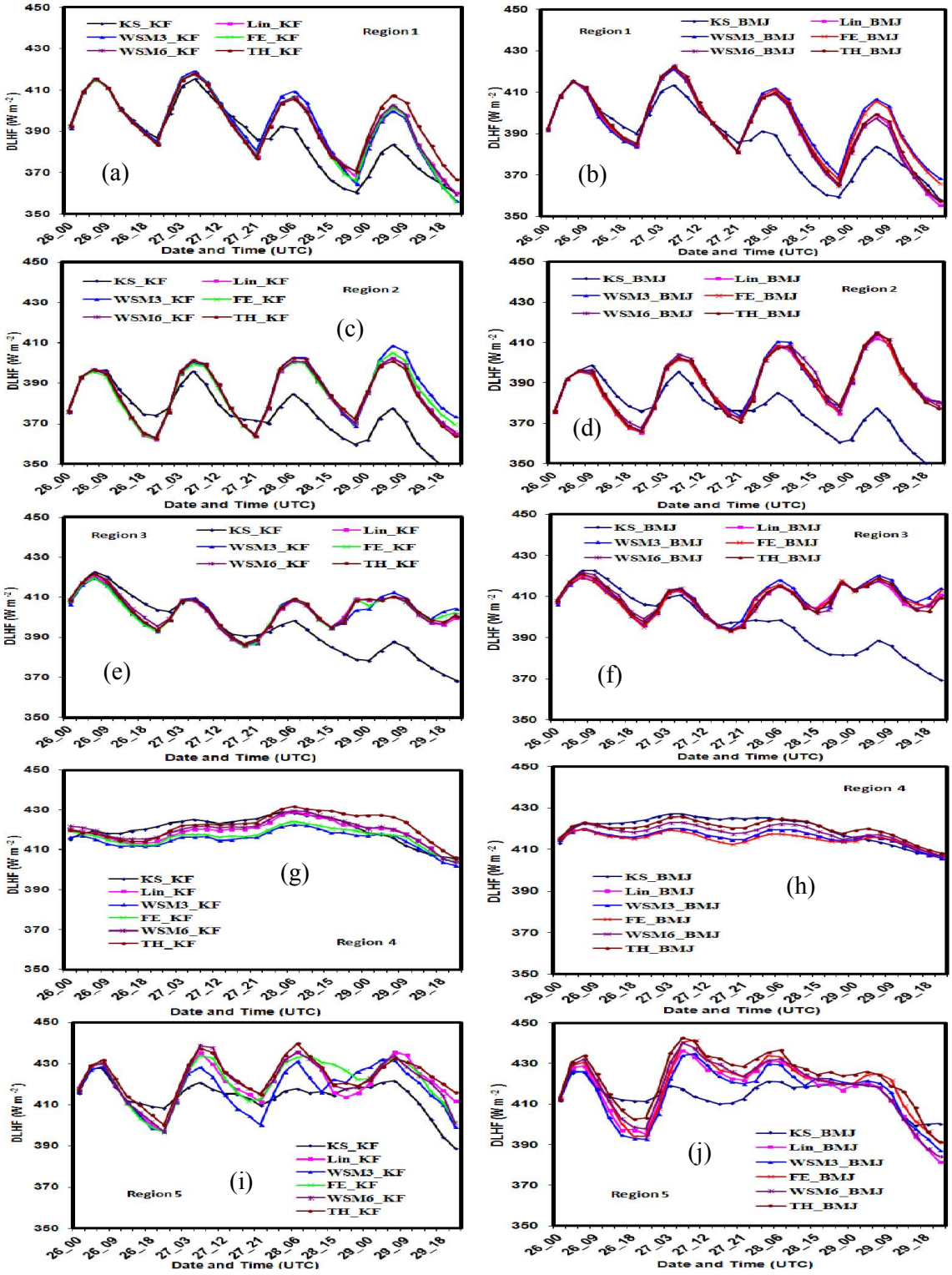

Fig. 19: Model simulated DLHF of TC Mala simulated in (a-b) R1, (c-d) R2, (e-f) R3, (g-h) R4 and (i-j) R5 by six different MP schemes coupling with KF and BMJ schemes respectively.

The crest and trough of area averaged DLHF in R2 (Figs. 19(c-d)) are almost similar but increasing in nature for all MP schemes in combination with KF and BMJ schemes. The crest and trough of area averaged DLHF in R3 (Figs. 19(e-f)) are found to decrease up to 1800 UTC of 27 April and after that it is found to increase in R3 for all MP schemes in combination with KF and BMJ schemes. In the oceanic region i.e. R4, the DLHF is almost constant during the simulated time for all MP schemes in combination with KF and BMJ schemes. Oscillation at day and night of DLHF is not found in the oceanic region. WSM3-KF and FE-BMJ combinations have simulated minimum DLHF during the study period. The crest and trough of DLHF in R5 (Figs. 19(i-j)) are almost similar during 26, 27 and 28 April. The oscillation has not been seen for all MPs coupling with BMJ scheme after 0000 UTC of 28 April in R5.

4.2.8 Downward Short Wave Heat Flux (DSHF)

The area averaged DSHFs for six different MP schemes coupling with KF and BMJ schemes in R1, R2, R3, R4 and R5 are presented in Figs. 20(a-j). The space averaged DSHFs are oscillatory in nature and maximum amplitude of oscillation has found at day time and zero at night time. The oscillatory pattern is similar in nature for all MP schemes in combination with KF and BMJ schemes in R1, R2, R3, R4 and R5. The amplitude of oscillation in R5 is decreased continuously (Figs. 20(i-j)) with the progress of time and minimum peak is found on 0600 UTC of 29 April for all MP schemes in combination with KF and BMJ schemes. The TC Mala moved towards R5 and DSHF is also decreased in R5. This suggests that the DSHF has been decreased in R5 due to the movement of TC in this region.

4.2.9 Upward Moisture Heat Flux (QFX)

The vertically integrated space averaged QFXs for six different MP schemes coupling with KF and BMJ schemes in R1, R2, R3, R4 and R5 are presented in Figs. 21(a-j) and found oscillatory in nature. The crest and trough of oscillation are found at day time and at night time respectively in R1, R2, R3 and R5 and for all combination of MPs and CPs. The crest of oscillation in R1 (Figs. 21(a-b)), R2 (Figs. 21(c-d)) and R3 (Figs. 21(e-f)) is almost constant in Nature but the amplitude is decreasing in R1, R2 and R3 respectively for all MP schemes in combination with KF and BMJ schemes.

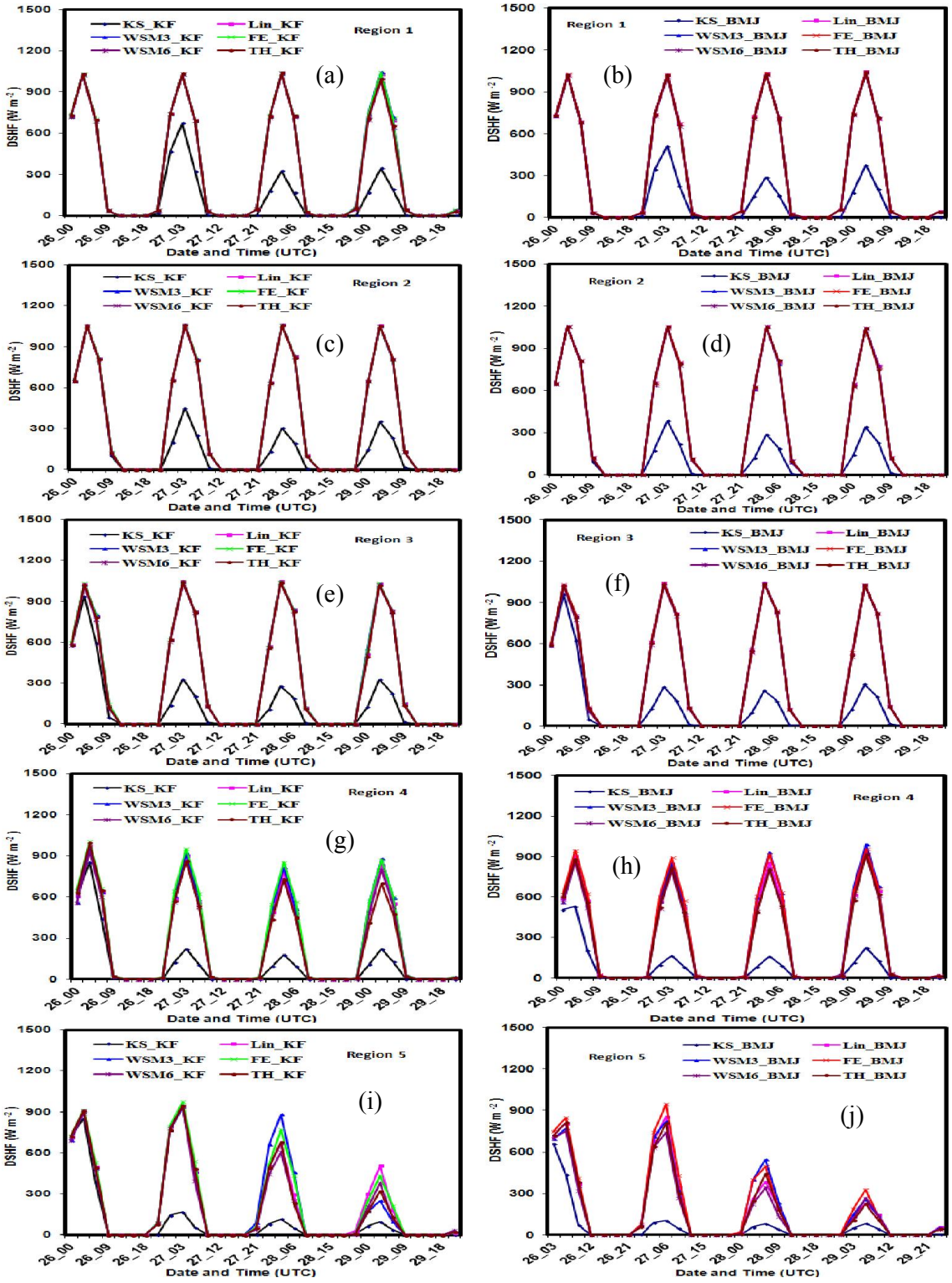

Fig. 20: Model simulated DSHF of TC Mala simulated in (a-b) R1, (c-d) R2, (e-f) R3, (g-h) R4 and (i-j) R5 by six different MP schemes coupling with KF and BMJ schemes respectively.

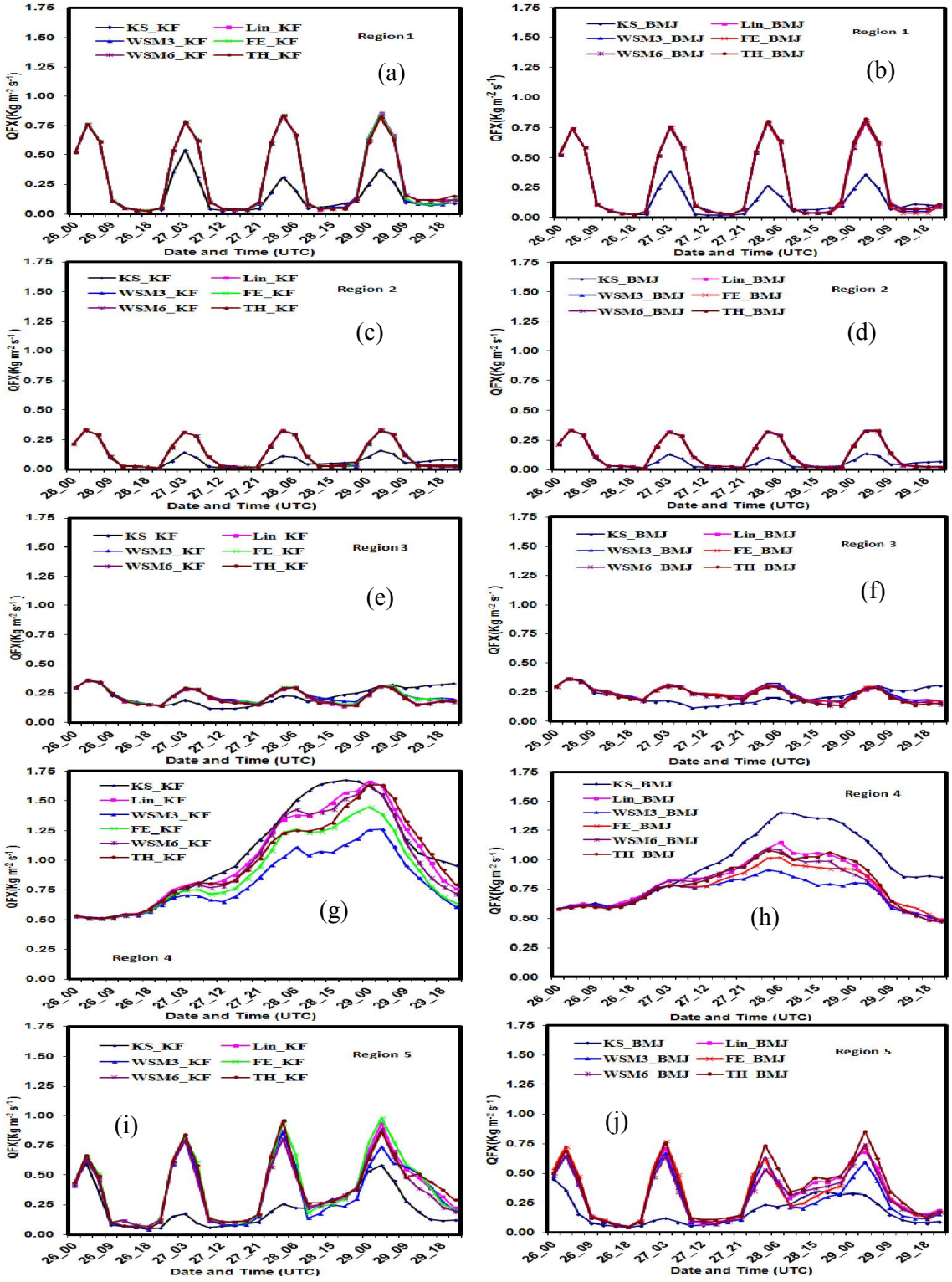

Fig. 21: Vertically integrated space averaged QFX of TC Mala at (a-b) R1, (c-d) R2, (e-f) R3, (g-h) R4 and (i-j) R5 simulated for different MP schemes coupling with KF and BMJ schemes.

The space averaged QFX has increased continuously up to 0000 UTC of 29 April for KF combination and 0300 UTC of 28 April for BMJ combination after that it has decreased (Figs. 21(g-h)). The intensity of cyclone increased due to the increase of QFX in the oceanic region. The amplitude of oscillation of QFX is found to increase in R5 as the cyclone moves towards land in R5. This increase is significant for KF scheme. It is also observed that the distribution pattern of area averaged upward moisture heat flux and latent heat flux is similar in R1, R2, R3, R4 and R5 but the latent heat flux is 250 times greater than that of upward moisture heat flux.

4.2.10 Outgoing long wave radiation (OLR)

The area averaged OLRs for six different MP schemes coupling with KF and BMJ schemes in R1, R2, R3, R4 and R5 are presented in Figs. 22(a-j). The Kessler scheme in combination with KF and BMJ schemes have simulated almost constant and minimum amount of OLR in R1, R2, R3, R4 and R5. The OLR is found oscillatory and its amplitude is almost constant with little anomalies in R1 (Figs. 22(a-b)) and R2 (Figs. 22(c-d)) for all MPs coupling with KF and BMJ schemes. After 0000 UTC of 28 April, WSM3 and WSM6 schemes have simulated maximum and minimum OLR in R1. The OLR is found oscillatory in R3 (Figs. 22(e-f)) for all MPs coupling with KF and BMJ schemes and the amplitude is found maximum for WSM3 and Ferrier schemes and minimum for Thompson scheme after 1800 UTC of 27 April.

The area averaged OLR in R4 (Fig. 22g) has decreased up to 1200 UTC of 28 April for all MPs coupling with KF scheme and after that the OLR has been increased in the oceanic region. The OLR has started to increase after 1200 UTC of 27 April (Fig. 22h) for all MPs coupling with BMJ scheme in the oceanic region. It is also observed that the significant differences exist among the MP schemes for the simulation of OLR in the oceanic region. Significantly higher amount of OLR has been simulated by WSM3 scheme than that of Thompson scheme coupling with KF and BMJ schemes. The OLR is found to decrease (Figs. 22(i-j)) significantly during 0000 UTC of 27 to 1200 UTC of 29 April and after that it has increased for all MPs in combination with KF and BMJ scheme in R5. The TC Mala crossed the Myanmar coast i.e. R5. Therefore, it is apparent that OLR decreases in a region where tropical cyclone moves.

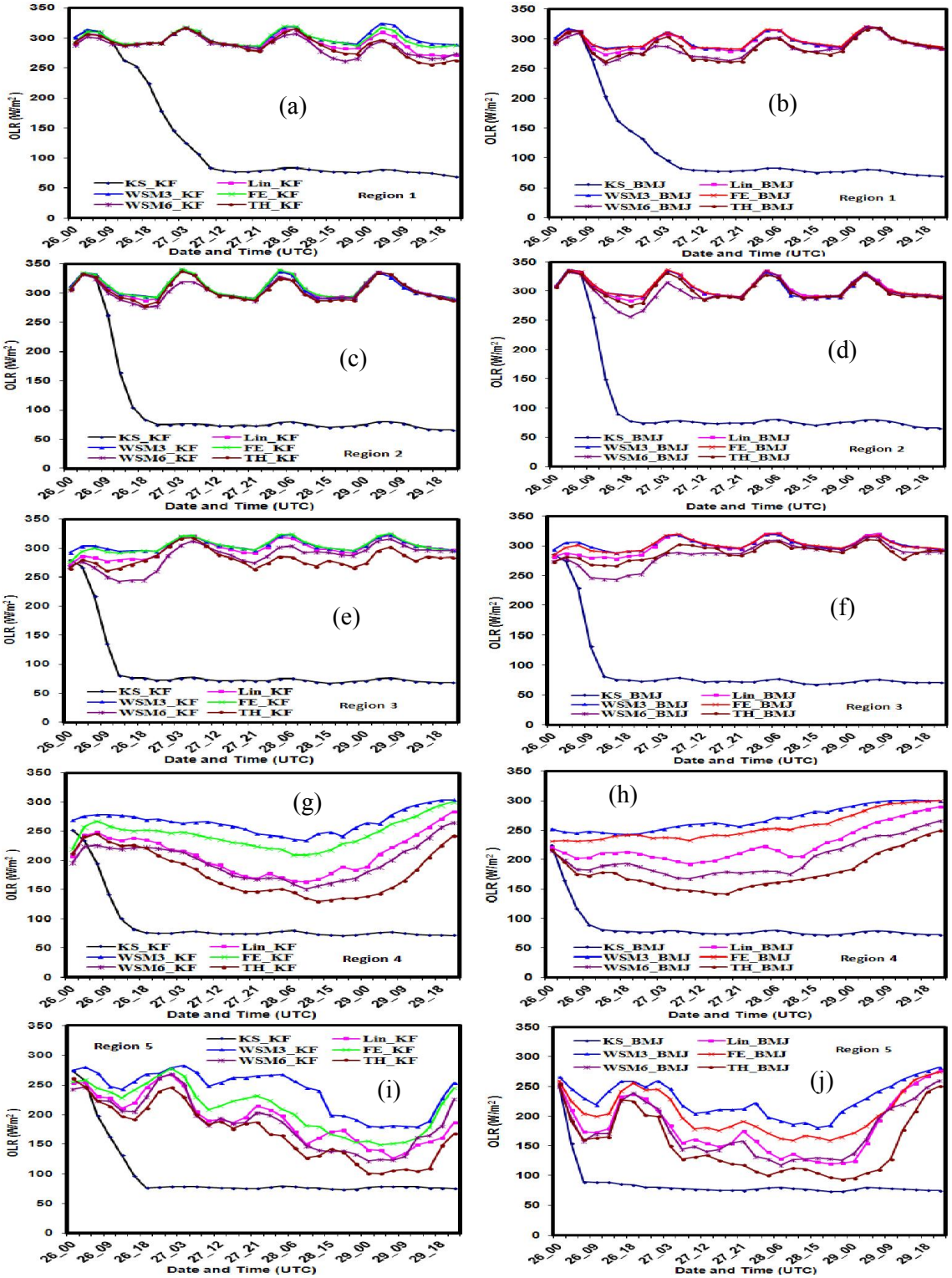

Fig. 22: Simulated OLR of TC Mala at (a-b) R1, (c-d) R2, (e-f) R3, (g-h) R4 and (i-j) R5 for six different MP schemes coupling with KF and BMJ schemes respectively.

4.2.11 Ground Heat Flux (GHF)

The vertically integrated space averaged GHFs for six different MP schemes coupling with KF and BMJ schemes are presented for R1, R2, R3, R4 and R5 as in Figs. 23(a-j). The space averaged GHFs are found to be oscillatory in nature and crest of oscillation is found at night time and trough at day time. The GHF is found to be negative in R1, R2, R3, R4 and R5 during the day time at 0000 to 1200 UTC and positive during the night time at 1500 to 0000 UTC. Kessler scheme coupling with KF and BMJ schemes have simulated minimum GHF in R1, R2, R3, R4 and R5. The crest and trough of oscillation in R1 (Fig. 23(a-b)), R2 (Figs. 23(c-d)) and R3 (Figs. 23(e-f)) are almost in constant in nature for all MP schemes in combination with KF and BMJ schemes. But the amplitude of trough is maximum in R2 and minimum in R3. The amplitude of oscillation of GHF is almost zero for all MPs coupling with KF and BMJ schemes in the oceanic region i.e. R4 (Figs. 23(g-h)). It is observed that the vertically integrated space averaged GHF has decreased at night time and increased during day time i.e. positive and negative values are decreased at night and day respectively in R5 (Figs. 23(i-j)) during the simulation time for all MPs coupling with KF and BMJ schemes. This suggests that the amplitude of oscillation of GHF has decreased as the TC Mala moves towards R5. The TC Mala moves in R5 where the GHF has been decreasing during the simulation period. It suggests that the cyclone moves in a direction where the GHF has decreased.

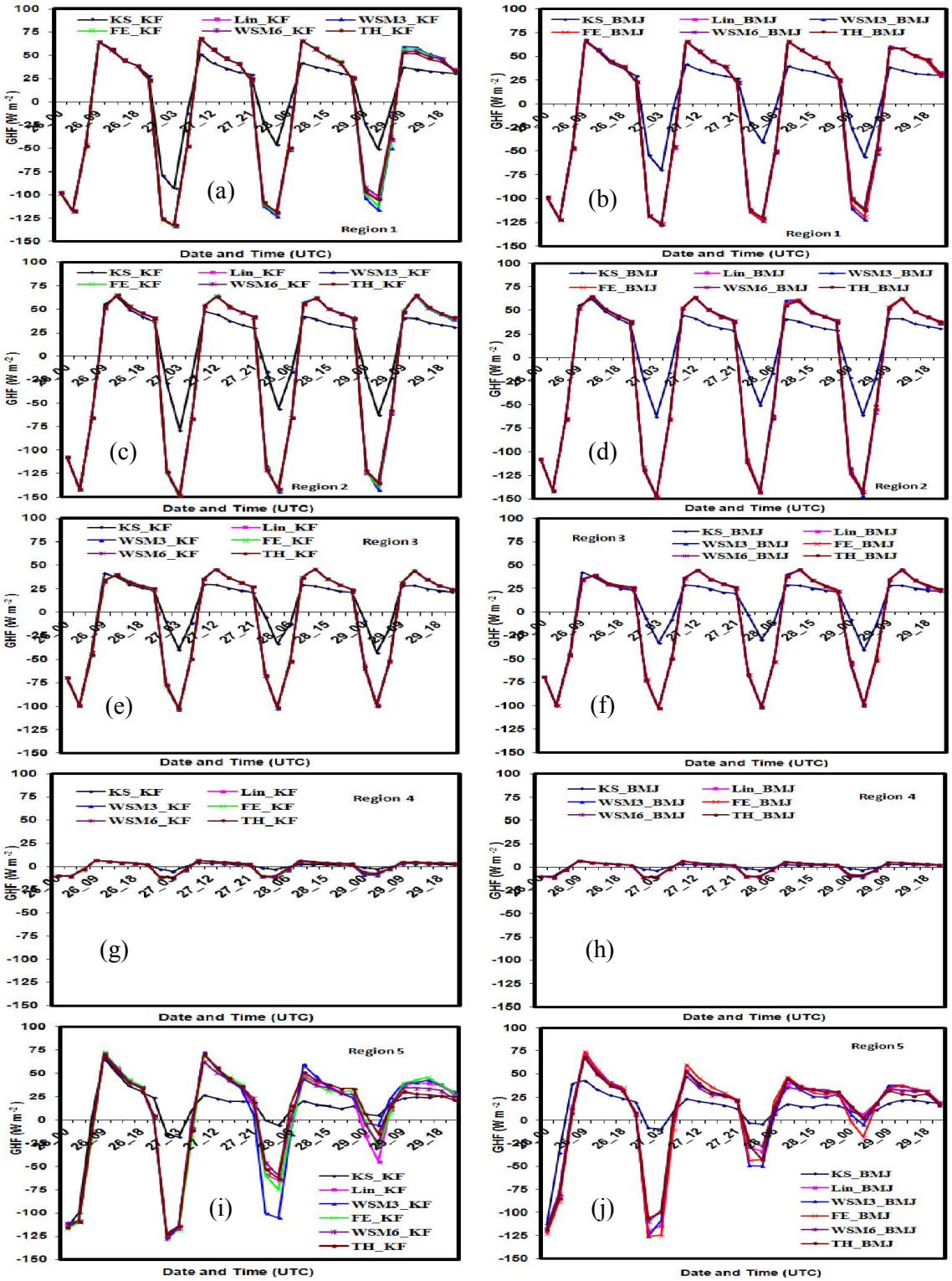

Fig. 23: Model simulated GHF of TC Mala for six different MP schemes at (a-b) R1, (c-d) R2, (e-f) R3, (g-h) R4 and (i-j) R5 coupling with KF and BMJ schemes respectively.

4.2. 12 Upward Heat Flux

The vertically integrated space averaged upward heat fluxes for six different MP schemes coupling with KF and BMJ schemes for R1, R2, R3, R4 and R5 are presented as in Figs. 24(a-j). Kessler MP Scheme has simulated minimum upward heat flux out of all MP schemes in all regions except R4, but the pattern is similar. The space averaged upward heat flux is oscillatory in nature and maximum amplitude of oscillation is found at day time and minimum at night time. The oscillatory pattern is similar in nature for all MP schemes in combination with KF and BMJ schemes in all the regions except oceanic region i.e. R4. The crest of oscillations of space averaged upward heat flux in R1 (Figs. 24(a-b)), R2 (Figs. 24(c-d)) and R3 (Figs. 24(e-f)) is almost constant for KF and BMJ schemes during the cyclonic period. But the amplitude is maximum in R2 and minimum in R3. The space averaged HFX has increased continuously up to 0300 UTC of 29 April by KF scheme and 0300 UTC of 28 April by BMJ scheme in the oceanic region i.e. R4 (Figs. 24(g-h)). The intensity of cyclone increased due to the increase of HFX in the oceanic region. Vertically integrated space averaged upward heat flux in R5 (Figs. 24(i-j)) has decreased continuously for all MPs in combination with KF and BMJ schemes and reached minimum on 0300 UTC of 29 April. The TC Mala moves in R5 where the upward heat flux has decreasing tendency during the simulation period. It suggests that the cyclone moves in a direction where the upward heat flux is decreases.

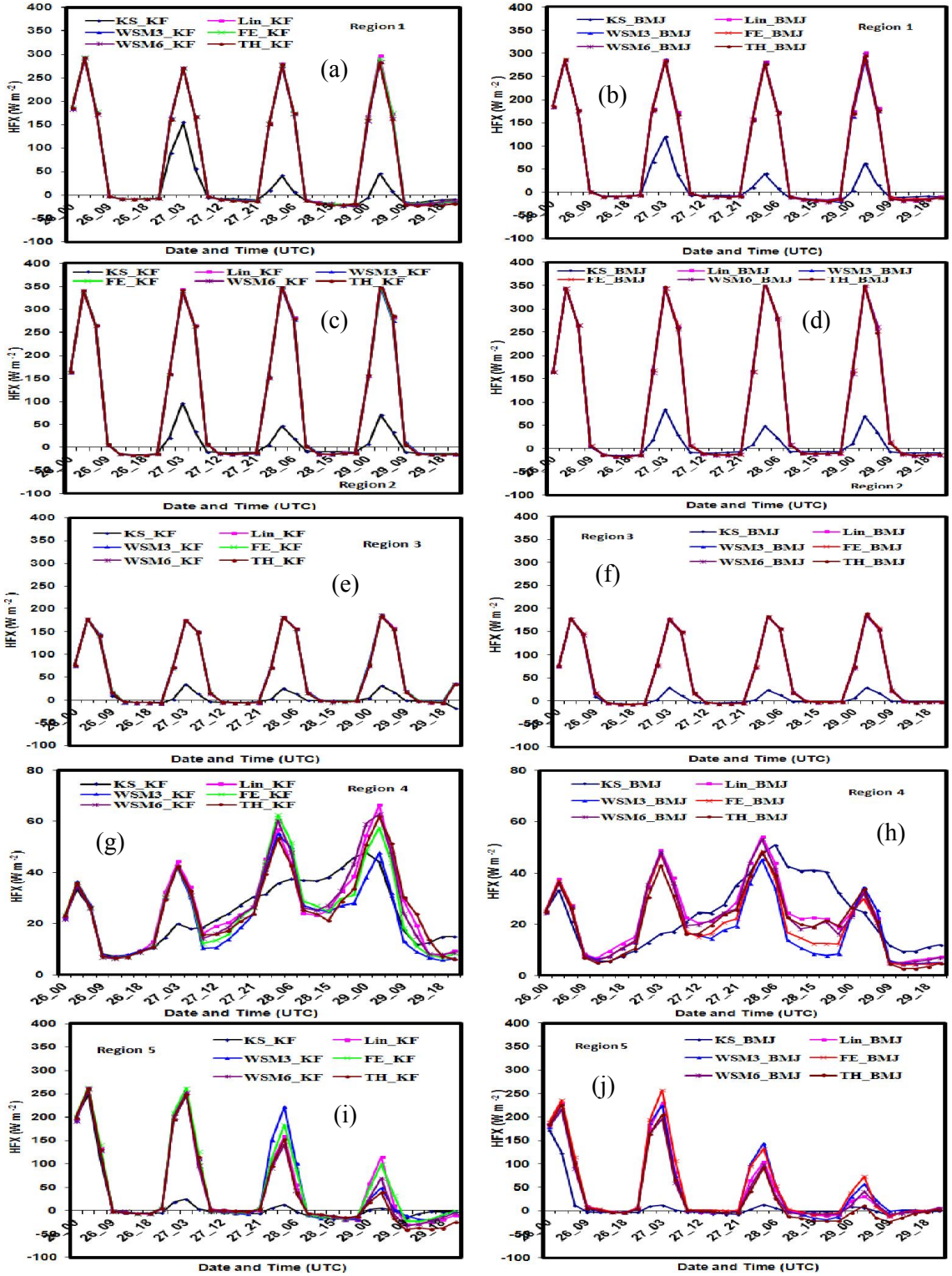

Fig. 24: Vertically integrated space averaged upward heat flux of TC Mala simulated for six different MPs at (a-b) R1, (c-d) R2, (e-f) R3, (g-h) R4 and (i-j) R5 coupling with KF and BMJ schemes respectively.

4.3 Tropical Cyclone Hudhud

4.3.1 Synoptic situation of Tropical Cyclone Hudhud

The Very Severe Cyclonic Storm 'Hudhud' developed from a low pressure area which lay over Tenasserim coast and adjoining North Andaman Sea in the morning of 6 October 2014. It concentrated into a Depression in the morning of the 7 October over the North Andaman Sea. Moving west-northwestwards it intensified into a Cyclonic Storm (CS) in 8 October and crossed Andaman Islands close to Long Island between 0300 and 0430 UTC of 8 October. It then emerged into Southeast Bay of Bengal and continued to move west-northwestwards. It intensified into a Severe Cyclonic Storm (SCS) at 9 October and further into a Very Severe Cyclonic Storm (VSCS) in the afternoon of 10 October. It continued to intensify further while moving northwestwards and reached maximum intensity in the early morning of 12 October with a maximum sustained wind speed (MSW) of 180 kmph over the West Central Bay of Bengal off Andhra Pradesh coast. The VSCS 'Hudhud' crossed north Andhra Pradesh coast over Visakhapatnam between 0630 and 0730 UTC of 12 October with the same wind speed. After landfall, it continued to move northwestwards for some time and weakened gradually into SCS in the evening and further into a CS in the midnight of same day. It then, weakened further into a DD in the early morning of 13 and weakened into a depression in the evening of 13.

4.3.2 Intensity of TC Hudhud

The intensity prediction of TC Hudhud considering 3-hourly central sea level pressure (CSLP) and associated MWS at 10 m level using different MP schemes coupling with CP schemes and two different initial conditions at 0000 UTC of 08 and 09 October 2014 are presented in Fig. 25(a-h). The simulated intensity in terms of CSLP for all MP schemes in combination with KF scheme with the initial conditions at 0000 UTC of 08 and 09 October are much higher than that of IMD observed pressure fall. The simulated CSLP for all MP schemes in combination with BMJ scheme with the initial condition at 0000 UTC of 08 are almost equal and is less than that of 09 October initial condition with IMD observed pressure fall. The simulated 10m maximum sustained wind speed for all MPs coupling with KF scheme is almost equal and less for BMJ combination with the initial conditions at 0000 UTC of 08 and 09 October IMD observed 10m sustained wind speed. The pressure departure is found maximum for Thompson scheme and minimum for WSM3 and Kessler schemes

coupling with KF and BMJ schemes during the simulation period. The simulated pressure fall and 10m sustained wind speed for all MPs in combination with KF and BMJ schemes indicate that the system attained severe cyclonic storm with core of hurricane intensity but the observation indicates that the system attained the intensity of cyclonic storm (950 hPa, 51 m s^{-1}). Among the MP schemes Thompson scheme has simulated minimum pressure departure and WSM6 has simulated maximum pressure drop.

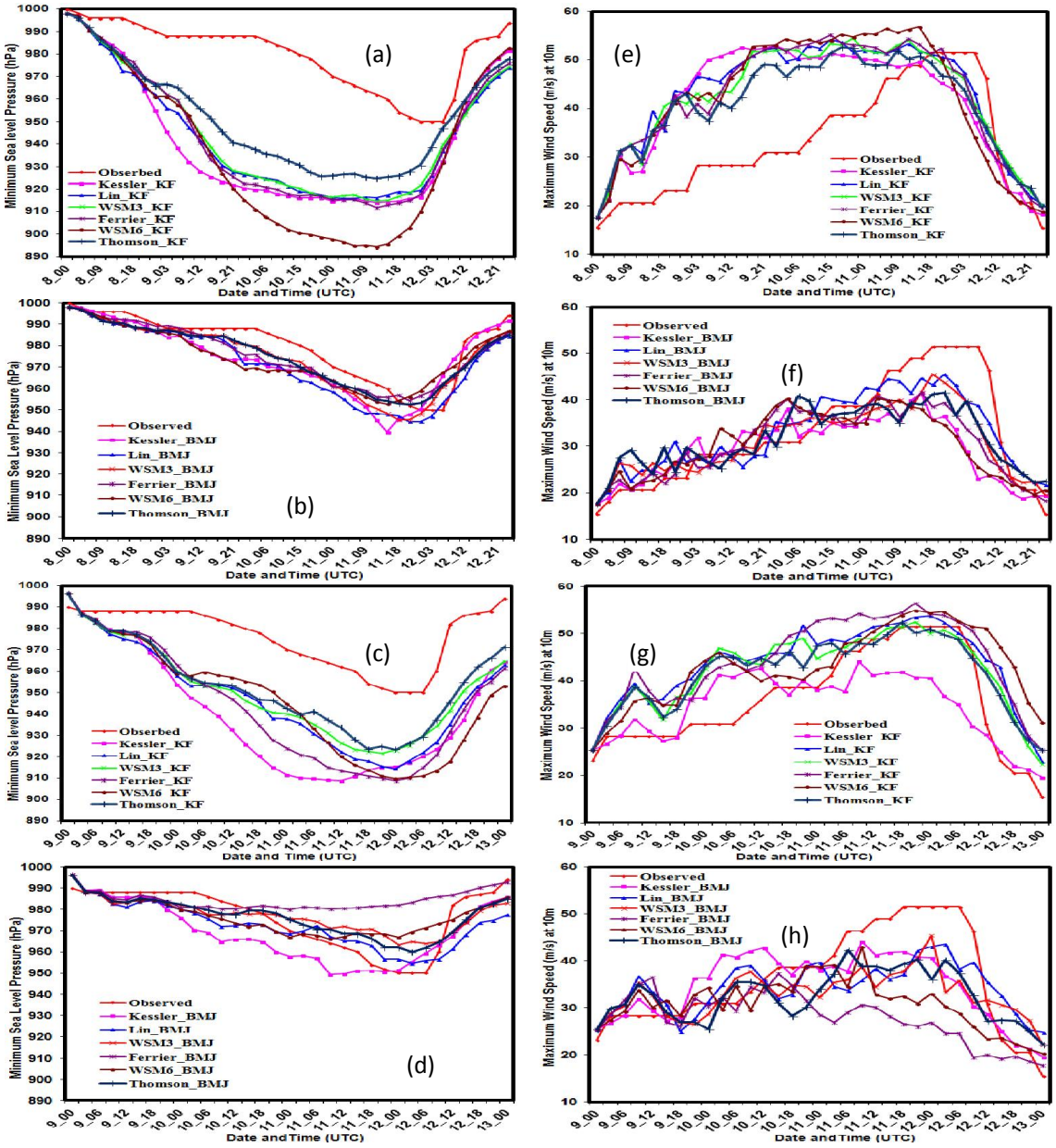

Fig. 25: Model simulated (a-d) MSLP (hPa) and (e-h) MWS at 10m level of TC Hudhud using six different MP schemes coupling with KF and BMJ schemes with 0000 UTC of 08 and 09 October 2014 initial conditions.

The simulated intensity at different combination of MPs and CPs with the initial condition of 0000 UTC of 18 May are (914 hPa, 52 m s^{-1}) for Kessler-KF, (915 hPa, 54 m s^{-1}) for Lin *et al*-KF, (914 hPa, 54 m s^{-1}) for WSM3-KF, (911 hPa, 54 m s^{-1}) for Ferrier-KF, (894 hPa, 56 m s^{-1}) for WSM6-KF and (924 hPa, 52 m s^{-1}) for Thompson-KF respectively.

4.3.3 Track of TC Hudhud

The 84 and 60-h model simulated tracks and IMD observed track of TC Hudhud for different MP schemes are displayed in Fig. 26(a-d). The landfall time as on 0630 and 0730 UTC of 12th October 2014,

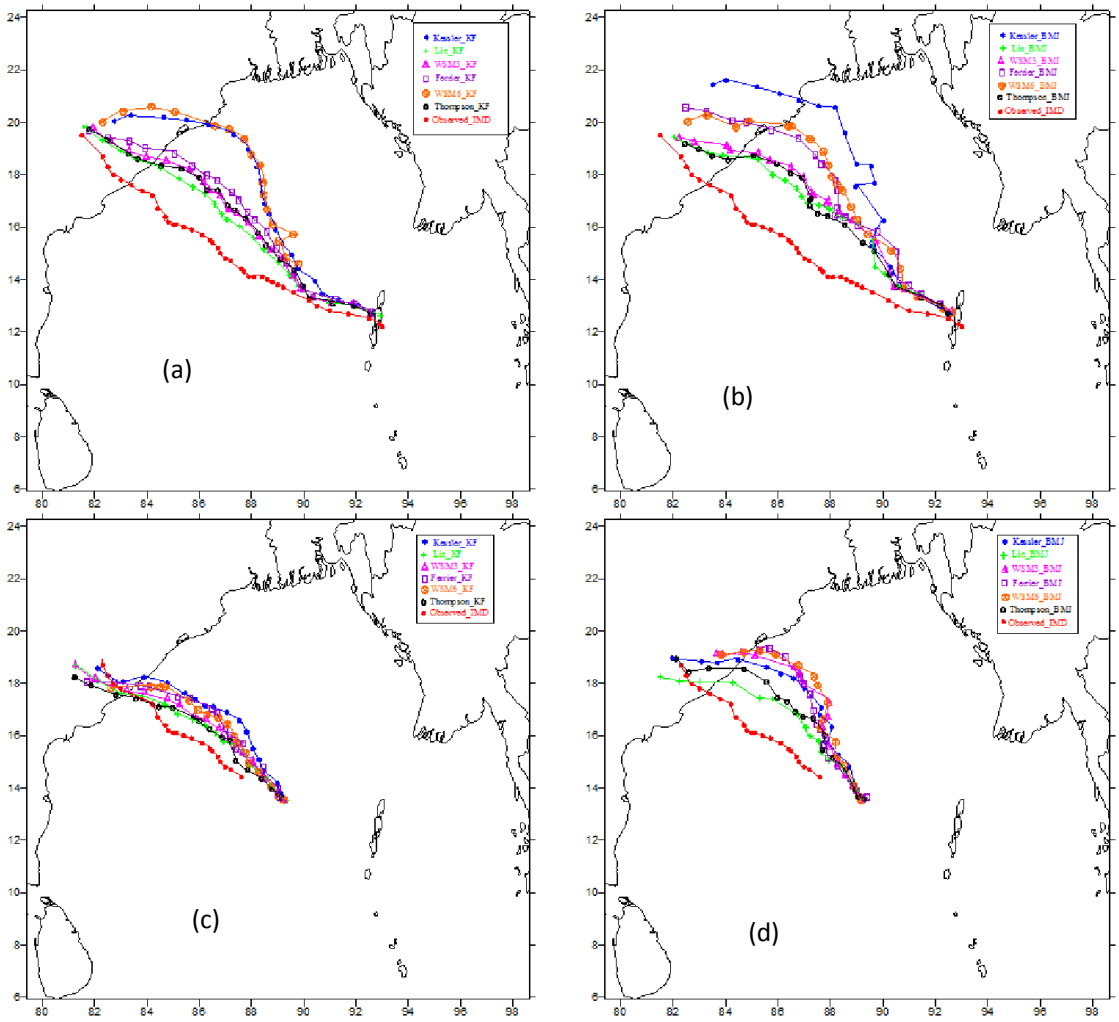

Fig. 26: Model simulated and IMD Observed tracks of TC Hudhud using six different MP schemes coupling with KF and BMJ schemes with the initial conditions at (a-b) 0000 UTC of 08 and (c-d) 09 October 2014.

The track forecasts for different sensitivity experiments have shown reasonably accurate prediction. All the simulations have captured the north-northwestward movement of TC Hudhud with the initial conditions at 0000 UTC of 08 and 09 October 2014. The sensitivity test has shown significant difference in track among the different microphysical schemes in combination with KF and BMJ schemes with the initial condition at 0000 UTC of 08 October. Lin-KF, WSM3-KF, Ferrier-KF and Thompson-KF combinations have simulated less deviated track and Kessler-KF and WSM6-KF combinations have simulated most deviated track with the initial condition at 0000 UTC of 08 October 2014. The simulated track is deviated towards left for all MPs coupling with KF and BMJ schemes with the initial condition at 0000 UTC of 08 October 2014. At the time of landfall, Lin and Thompson schemes in combination with KF and BMJ schemes has simulated less deviated track with the initial condition of 0000 UTC of 08 October.

The track deviation is less for all MP schemes coupling with KF and BMJ scheme with the initial conditions at 0000 UTC of 09 October although coupled with BMJ scheme the track is found to deviate towards left for all MPs. The simulated landfall position for different MP schemes is very near to the observed landfall position with the initial condition of 0000 UTC of 09 October. The observed landfall time for all MP schemes is almost matched with the model simulated landfall time at the initial condition of 0000 UTC of 09 October. The landfall time is most deviated by Kessler, WSM3, Ferrier, and WSM6 in combination with BMJ scheme and Lin-BMJ and Thomson-BMJ combinations have simulated less deviated track with the initial condition of 0000 UTC of 09 October.

4.3.4 Track Error of TC Hudhud

The tracks errors have been estimated on the basis of IMD observed track and are presented in Figs. 27 (a-d) respectively. The error is not systematic by using KF and BMJ schemes with the initial conditions at 0000 UTC of 08 and 09 October 2014. The track error with the 0000 UTC of 09 October initial conditions is very much less compared to the initial condition of 08 October. WSM6-KF combination simulated has most deviated track and Thompson-BMJ simulated less deviated track with respect to observed track of IMD with the initial conditions at 0000 UTC of 08 October. Again Kessler-KF combination has simulated most deviated track and Thompson-KF has simulated less deviated track with the initial condition at 0000 UTC of 09 October. The track error is minimum in comparison with IMD observed track at the time of landfall using Lin scheme coupling with KF scheme with the initial conditions at

0000 UTC of 08 and 09 October 2014. The average track error (Fig. 27e) using 0000 UTC of 08 October initial conditions is much higher than that of 0000 UTC of 09 October initial conditions. KF scheme has given less track error than that of BMJ scheme for all MPs with the initial conditions at 0000 UTC of 09 October. The minimum average track error has been found for Thompson-KF and Lin-KF combinations were 60 and 70 km respectively with the initial conditions at 0000 UTC of 09 October. The average track error is found maximum using Kessler-BMJ schemes for all MPs with the initial condition at 0000 UTC of 08 October.

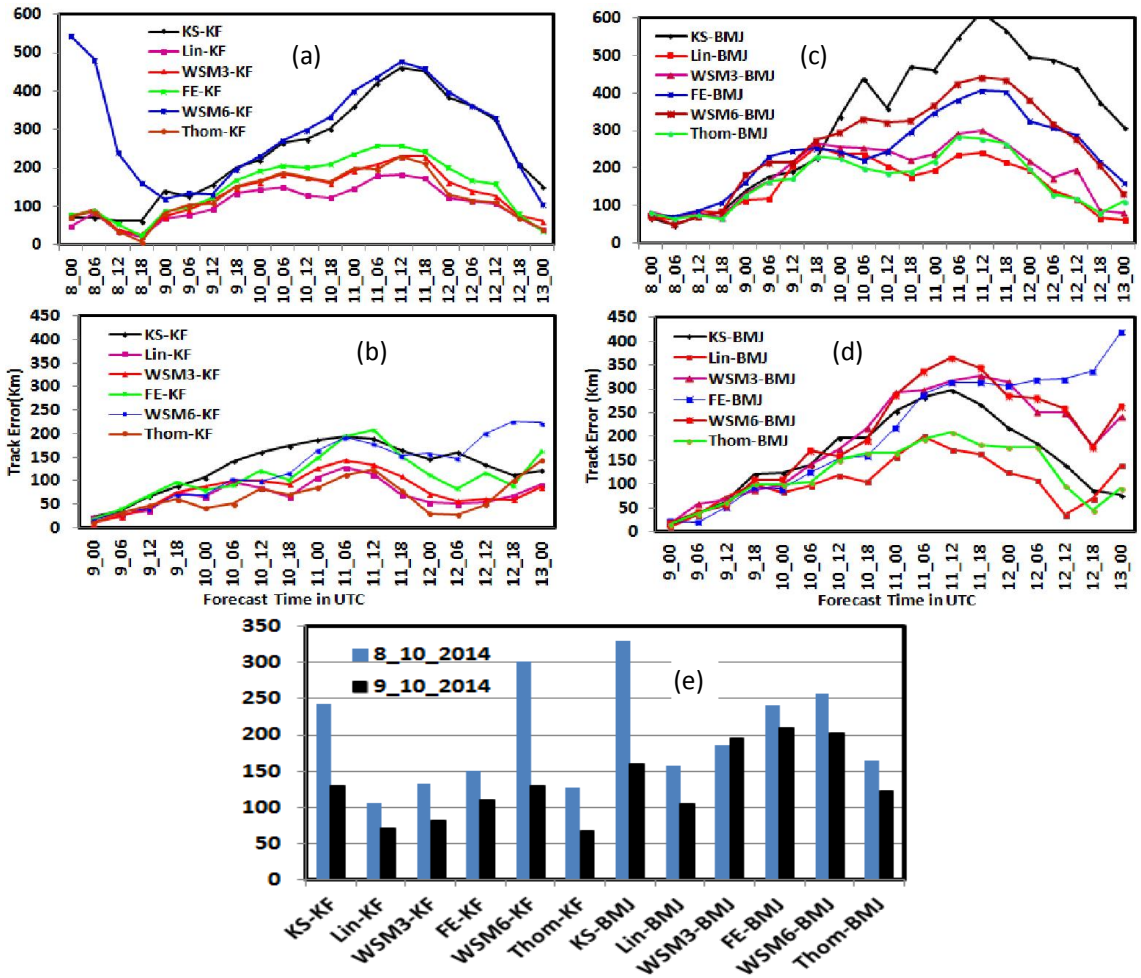

Fig. 27: Model simulated and IMD observed track error of TC 'Hudhud' using six different MP schemes coupling with (a-b) KF and (c-d) BMJ schemes and (e) average track error with the initial conditions at 0000 UTC of 08 and 09 October in 2014.

4.3.5 Convective Available Potential Energy

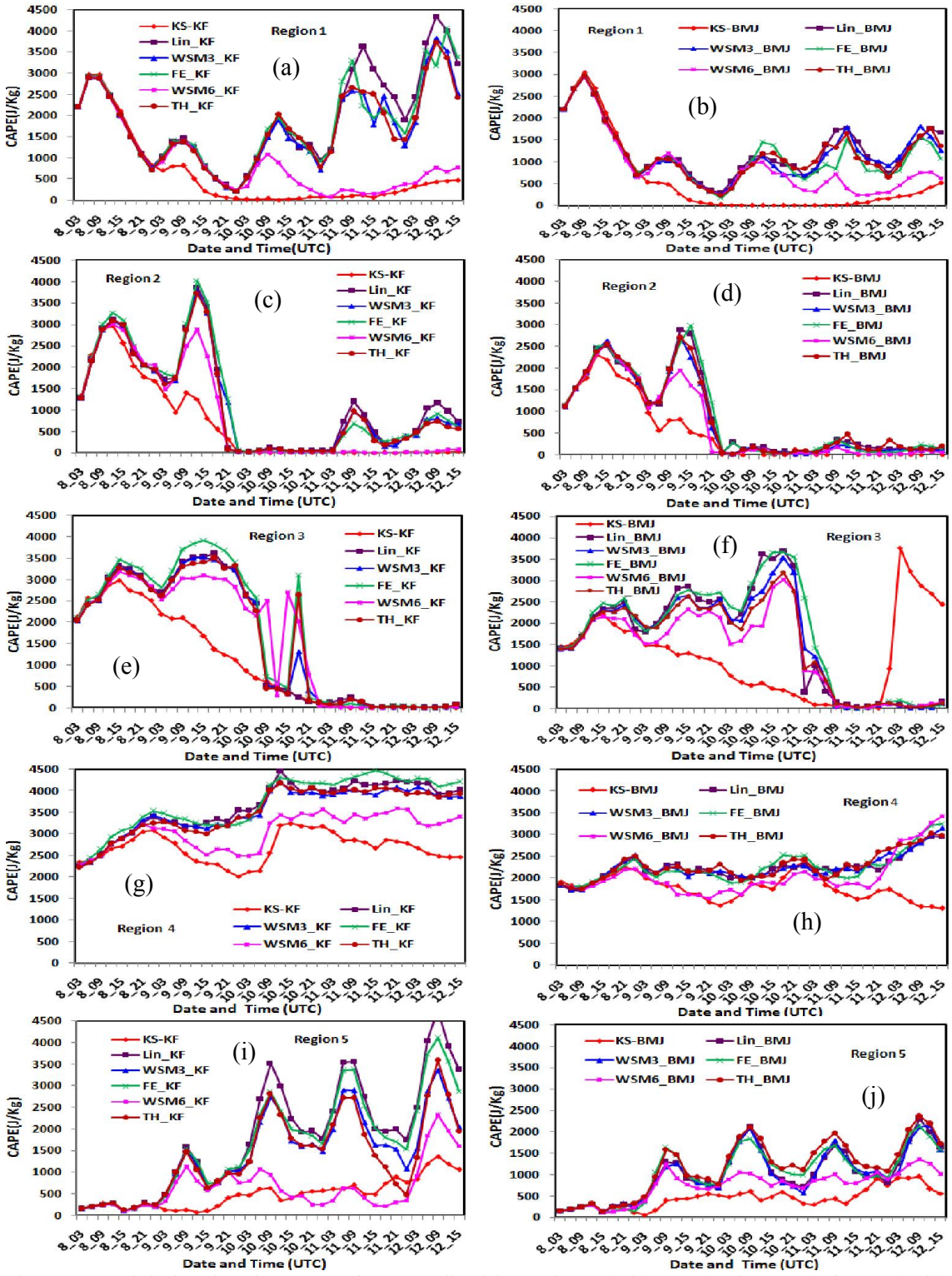

Fig. 28: Model simulated CAPE of TC Hudhud in regions (a-b) R1, (c-d) R2, (e-f) R3, (g-h) R4 and (i-j) R5 by six different MP schemes coupling with KF and BMJ schemes respectively.

The vertically integrated space averaged CAPE has been simulated in R1, R2, R3, R4 and R5 using six different MP schemes in combination with KF and BMJ schemes and the results are presented in Figs. 28(a-j). Kessler and WSM6 scheme has simulated minimum CAPE coupling with KF and BMJ schemes in R1, R2, R3, R4 and R5 and CAPE is found to decrease with the progression of time. In R1, the CAPE has been decreased for all MPs coupling with KF and BMJ schemes up to 0000 UTC of 10 October and after that it is found to increase (Figs. 28(a-b)). This increase is significant for all MPs coupling with KF scheme. The vertically integrated space averaged CAPE in R2 (Figs. 28(c-d) is found to increase up to 1500 UTC of 09 October and suddenly fall down and has reached minimum to zero at 0000 UTC of 10 October for all MPs coupling with KF and BMJ Scheme. In R1 and R2, CAPE is found to increase and decrease for all MPs coupling with KF and BMJ schemes after 0000 UTC of 10 October respectively. This suggests that the TC moves towards R2 not in R1. The vertically integrated space averaged CAPE is found to increase continuously and has reached maximum at 1800 UTC of 9 and 10 October for KF and BMJ scheme respectively and after that it has suddenly become zero for all MPs (Fig. 28(e-f)). The space averaged CAPE has increased up to 1200 UTC of 11 October and 0000 UTC of 9 October for KF and BMJ scheme respectively and after that it is almost constant in the oceanic region R4 (Fig. 28 (g-h)) for all MPs. In R4, Ferrier and Kessler schemes coupling with KF and BMJ schemes have simulated maximum and minimum CAPE during the period. The space averaged CAPE is found oscillatory and increased continuously in R5 (Fig. 28i), having maximum at 1200 UTC of 12 October for all MPs in combination with KF and BMJ scheme. The crest and trough are found at day and night time respectively. The vertically integrated space averaged CAPE is found to decrease after 1500 and 0900 UTC of 09 and 10 October and suddenly it is found to fall down and become zero in R2 and R3 respectively for all MPs coupling with KF and BMJ Scheme. The TC Hudhud moves in R2 and CAPE has decreased in this region, which also suggests that the TC moves in a direction where CAPE is decreases.

4.3.6 Convective Inhibition Energy (CIN)

The vertically integrated space averaged CIN has been simulated in R1, R2, R3, R4 and R5 using six different MP schemes in combination with KF and BMJ schemes and the results are presented in Figs. 29(a-j). Kessler and WSM6 scheme has simulated minimum CIN coupling with KF and BMJ schemes in R1, R2, R3, R4 and R5 and CIN is found to decrease with the progression of time. The space averaged CIN has been simulated at an oscillatory pattern in R1.

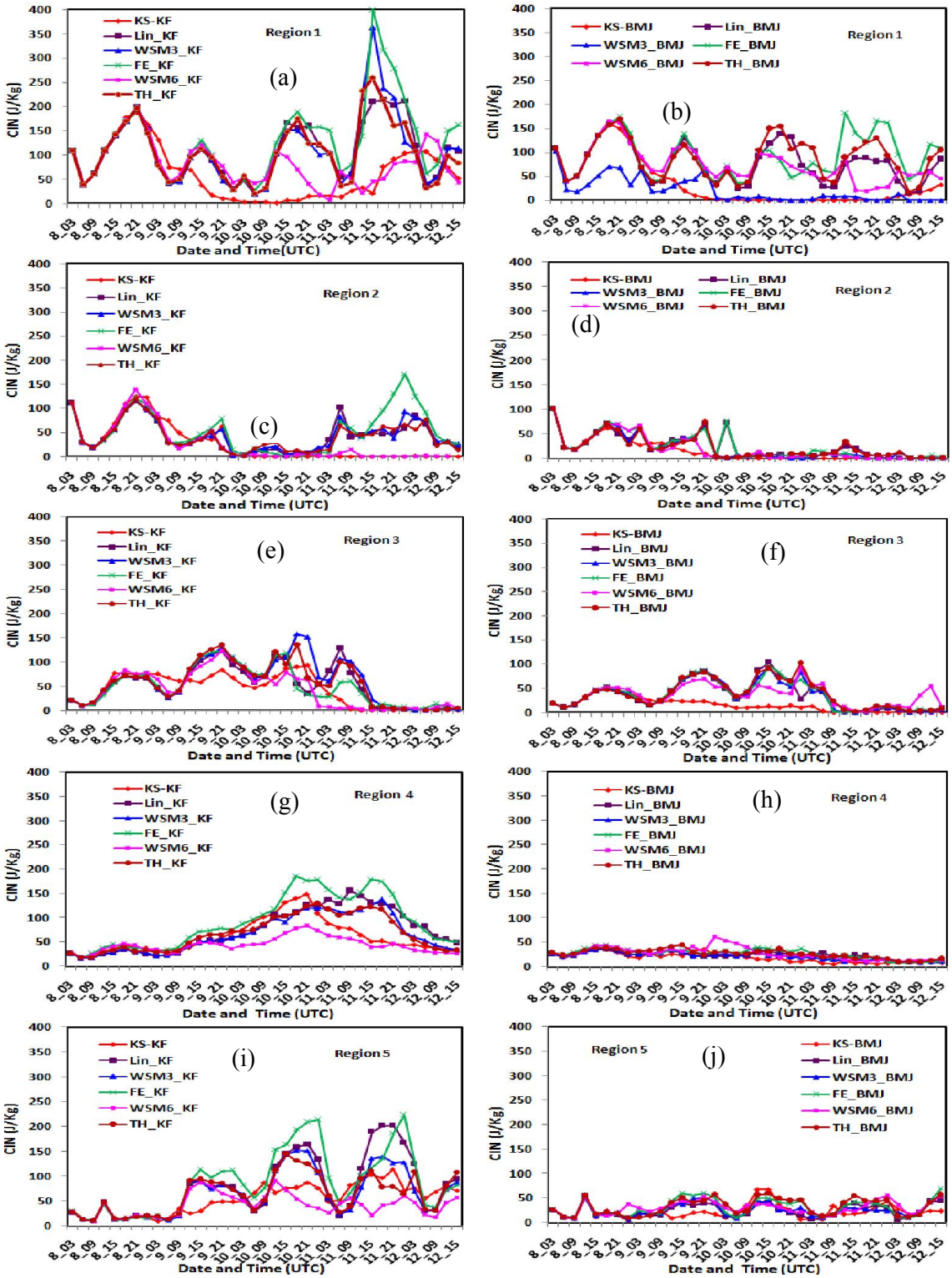

Fig. 29: Vertically integrated space averaged CIN of TC Hudhud in (a-b) R1, (c-d) R2, (e-f) R3, (g-h) R4 and (i-j) R5 by six different MP schemes coupling with KF and BMJ schemes respectively.

The crest of oscillation is found at night time and trough is found at day time for all MPs coupling with KF and BMJ schemes. The crest of oscillation is found minimum at 1200 UTC of 9 October and maximum 1500 UTC of 11 October (Fig. 29a) for all MPs coupling with KF scheme. The height of crest and trough is almost constant for all MPs coupling with BMJ scheme (Fig 29b). The space averaged CIN in R2 is simulated at an oscillatory pattern (Fig. 29(c) and CIN is seen to decrease to zero at 0000 UTC of 10 October and it continues until 0000 UTC of 11 October and after that the CIN has been raised for all MPs coupling with KF scheme. The simulated CIN is found minimum up to 0000 UTC of 10 October and after that it becomes almost zero for all MPs coupling with BMJ scheme in R2 (Fig. 29d). The minimum CIN in R2 on 10 October suggests that the region vulnerable for cyclone movement

The vertically integrated space averaged CIN in region R3 has simulated at an oscillatory pattern (Figs. 29 (e-f)) and significant amount of CIN has seen in R3 during 0600 UTC of 8 October to 1200 UTC of 11 October for all MPs coupling with KF and BMJ schemes. After that the CIN has found to zero for all MPs coupling with KF and BMJ schemes in R3 when the TC Hudhud in nearby to R2 and R3. The CIN is found to increase and in slightly oscillatory for all MPs coupling with KF scheme up to 1800 UTC of 11 October (Fig. 29g) and after that it has decreased continuously in the oceanic region i.e. R4. In BMJ scheme the simulated CIN is almost constant and minimum for all MPs (Figs. 29h).

In R5 the area averaged CIN has been simulated an oscillatory pattern from 0900 UTC of 9 October for all MPs in combination with KF (Fig. 29i) and BMJ schemes. The CIN is almost constant and zero up to 0900 UTC of 9 October for KF scheme and although the simulation for BMJ (Fig. 29j) scheme. The CIN is almost zero up to 0900 UTC of 9 October suggests that the cyclone moves initially towards R5 but due to the increase of CIN the TC moves far away from R5. The TC Hudhud moves in a direction in which region the CIN gas simulated almost zero.

4.3.7 Downward Long Wave Heat Flux (DLHF)

The vertically integrated space averaged DLHFs for six different MP schemes coupling with KF and BMJ schemes in different regions R1, R2, R3, R4 and R5 are presented in Figs. 30(a-j) respectively. The space averaged DLHFs are oscillatory in nature and maximum and minimum amplitude of oscillations are found at day time (0600–1200 UTC) and night time

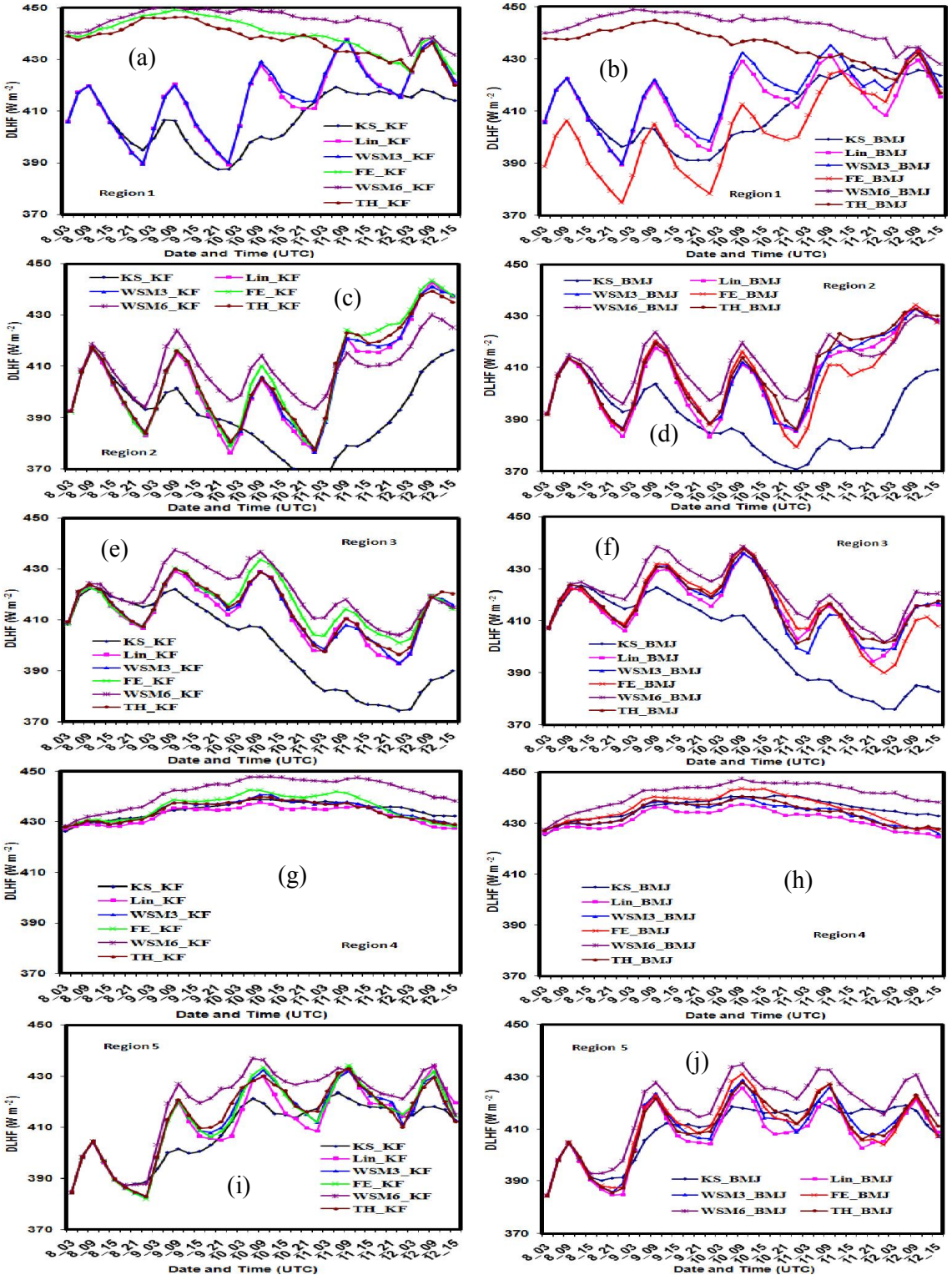

Fig. 30: Model simulated DLHF of TC Hudhud simulated in (a-b) R1, (c-d) R2, (e-f) R3, (g-h) R4 and (i-j) R5 by six different MP schemes coupling with KF and BMJ schemes respectively.

(1800-0000 UTC) respectively in different regions during the simulation period. Kessler and WSM6 schemes have been simulated minimum and maximum DLHFs in all regions. The crest and trough of DLHFs in R1 (Figs. 30 (a-b)) has almost constant up to 0000 UTC of 10 October and after that it has increased continuously for all MPs coupling with KF and BMJ schemes except Ferrier-KF, WSM6-KF, WSM6-BMJ, Thompson-KF and Thompson-BMJ.

The area averaged DLHFs in R2 (Figs. 30(c-d)) is almost similar for all MP schemes in combination with KF and BMJ schemes. DLHFs has slightly decreased up to 0000 UTC of 11 October and after that it has increased significantly for all MPs and CPs. The area averaged DLHFs in R3 (Figs. 30 (e-f)) is almost similar and increasing tendency up to 1500 UTC of 10 October and after that it is found to decrease for all MP schemes in combination with KF and BMJ schemes.

In the oceanic region i.e. R4, the DLHFs is almost constant for all MP schemes in combination with KF and BMJ schemes during the simulated period. Oscillation at day and night of DLHFs is not significant in the oceanic region. The crest and trough of DLHFs in R5 (Figs. 30(i-j)) has been increased continuously up to 1200 UTC of 10 October and after that it has found almost constant up to simulation for all MPs coupling with KF and BMJ scheme. The DLHFs has found to decrease initially and at the time of landfall it is increase in a region where the TC Hudhud moves.

4.3.8 Downward Short Wave Heat Flux (DSHF)

The vertically integrated space averaged DSHFs for six different MP schemes coupling with KF and BMJ schemes in R1, R2, R3, R4 and R5 are presented in Figs. 31 (a-j). Kessler scheme has been simulated minimum DSHFs and WSM6 scheme has simulated higher than that of Kessler but lower than that of other MP schemes. The space averaged DSHFs are oscillatory in nature and maximum amplitude of oscillation has found at day time and minimum at night time. The oscillatory pattern is similar in nature for all MP schemes in combination with KF and BMJ schemes in all the regions. The crest of oscillations of space averaged DSHFs in R1 (Figs. 31(a-b)), R3 (Figs. 31(e-f)), R4 (Figs. 31(g-h)) and R5 (Figs.31 (i-j) is almost constant with little anomalies for KF and BMJ schemes during the cyclonic period. The amplitude has maximum in R1, R3, R5 and minimum in R4. Vertically integrated space averaged DSHFs in R2 (Figs. 31(c-d)) has decreased continuously from 0600 UTC of 10 October and reached minimum at 0600 UTC of 12 October for all MPs in combination with KF and BMJ schemes.

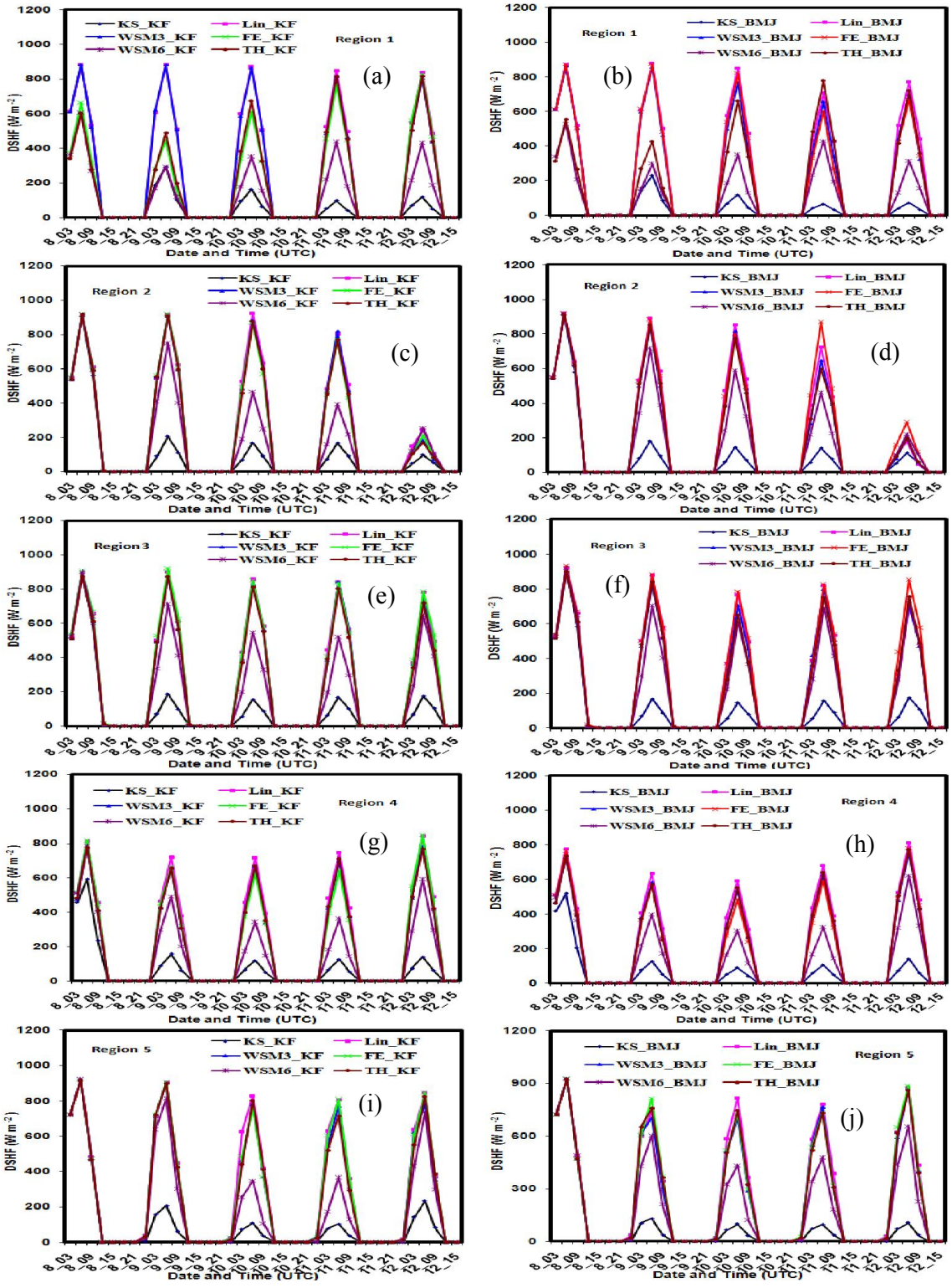

Fig. 31: Model simulated DSHF of TC Hudhud simulated in (a-b) R1, (c-d) R2, (e-f) R3, (g-h) R4 and (i-j) R5 by six different MP schemes coupling with KF and BMJ schemes respectively.

4.3.9 Upward Moisture Heat Flux (QFX)

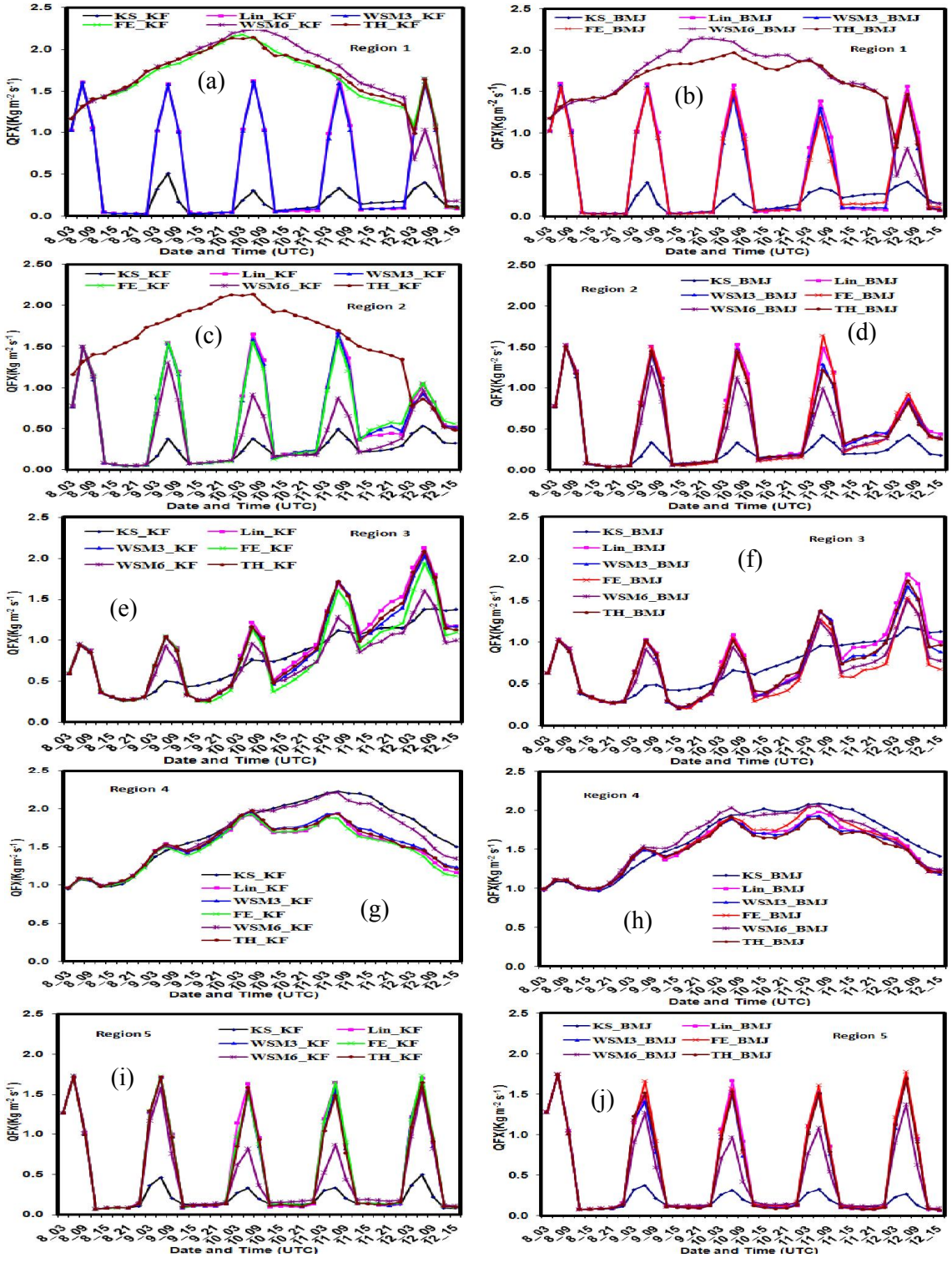

Fig. 32: Vertically integrated space averaged QFX of TC Hudhud at (a-b) R1, (c-d) R2, (e-f) R3, (g-h) R4 and (i-j) R5 simulated for different MP schemes coupling with KF and BMJ schemes.

The vertically integrated space averaged QFXs for six different MP schemes coupling with KF and BMJ schemes for R1, R2, R3, R4 and R5 are presented in Figs. 32(a-j). and found oscillatory in nature. The crest and trough of oscillation are found at day time and at night time respectively for all combination of MPs and CPs. Kessler and WSM6 schemes have been simulated minimum and maximum QFXs in all regions. The crest and trough of QFXs in R1 (Figs. 32 (a-b)) has almost constant for all MPs coupling with KF and BMJ schemes except Ferrier-KF, WSM6-KF, WSM6-BMJ, Thompson-KF and Thompson-BMJ. The amplitude of oscillation of QFXs in R2 (Figs. 32(c-d)) has almost constant up to 0600 UTC of 11 October and after that the amplitude is minimum at 0600 UTC of 12 October for all MP schemes in combination with KF and BMJ schemes except Thompson-KF.

In R3 Figs. 32(e-f) the crest is found to increase continuously for all MPs in combination with CP schemes and this increase is significant for KF cumulus parameterization scheme.
It is found in R4 that the space averaged QFXs has increased continuously up to 0000 UTC of 11 October and after that it has decreased (Figs. 32(g-h)). The intensity of cyclone increased due to the increase of QFXs in the oceanic region. When the cyclone crossed the coast the QFXs has decreased. In R5 the QFXs is found to be oscillatory and the crest of oscillation is found almost constant. It is also observed that the distribution pattern of area averaged upward moisture heat flux and latent heat flux is similar in R1, R2, R3, R4 and R5 but the latent heat flux is 250 times greater than that of upward moisture heat flux.

4.3.10 Outgoing long wave radiation (OLR)

The area averaged OLRs for six different MP schemes coupling with KF and BMJ schemes in R1, R2, R3, R4 and R5 is presented in Figs. 33(a-j). The Kessler and WSM6 scheme in combination with KF and BMJ schemes have simulated almost constant and minimum amount of OLRs and Lin scheme has simulated maximum amount of OLRs in R1, R2, R3, R4 and R5. The OLRs is found slightly oscillatory and its amplitude is almost constant with little anomalies in R1 (Figs. 33(a-b)) for Lin, WSM3, Kessler and WSM6 schemes coupling with KF scheme. Thompson-KF and Ferrier-KF are found to be decreased up to 0600 UTC of

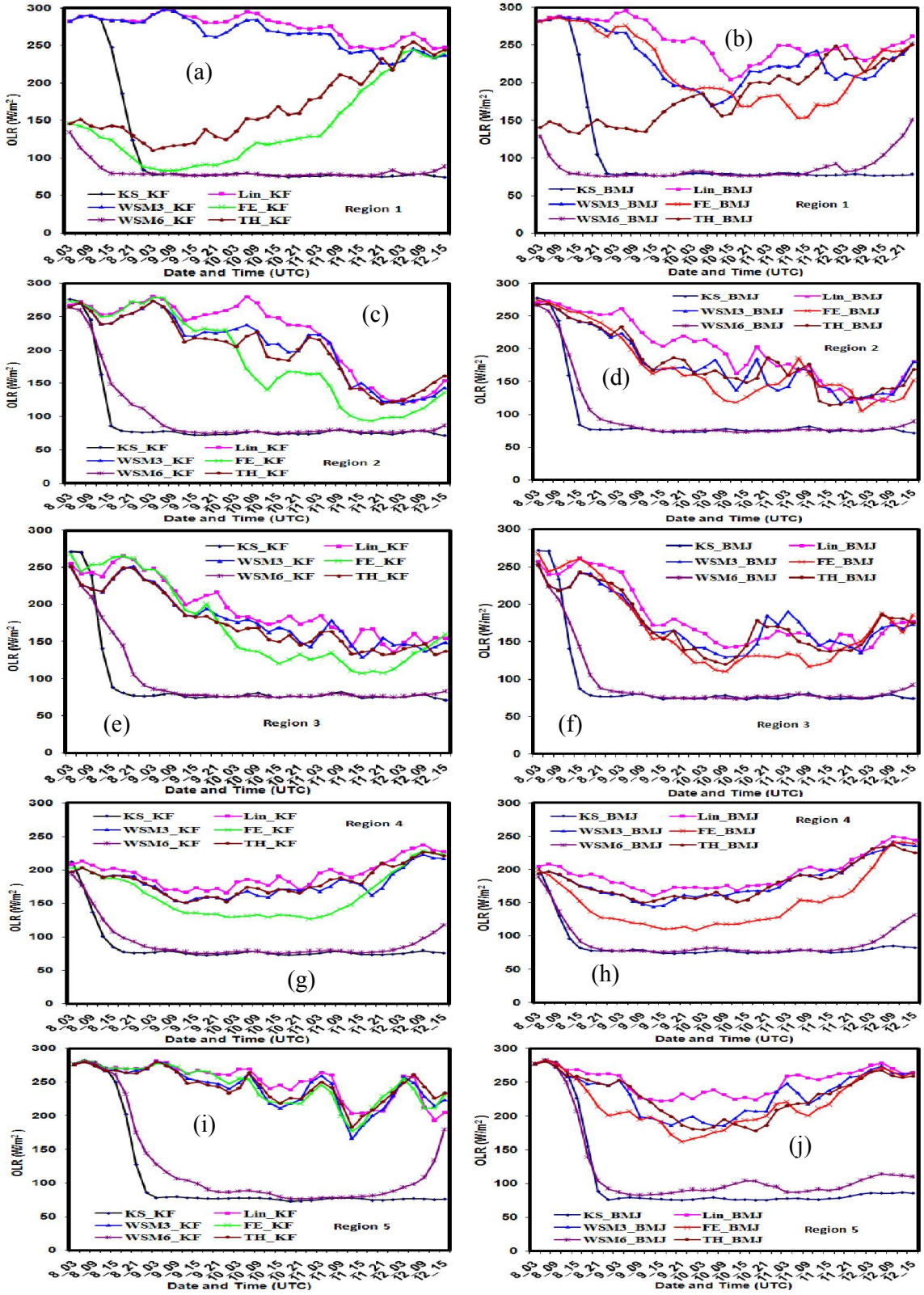

Fig. 33: Simulated OLR of TC Hudhud at (a-b) R1, (c-d) R2, (e-f) R3, (g-h) R4 and (i-j) R5 for six different MP schemes coupling with KF and BMJ schemes respectively.

9 October and after that it has increased. The OLRs in R2 is decrease up to 0600 UTC of 10 October and after that it has increase for Lin, Ferrier and WSM3 schemes coupling with BMJ scheme. It is also observed that the significant differences exist among the MP schemes for the simulation of OLRs in the R1 region. The OLRs has found to be oscillatory and amplitude is almost constant (Figs. 33(c-d)) for all MPs coupling with KF and BMJ schemes. After 0000 UTC of 11 October all MPs are decreased in R2. The OLRs in R3 (Figs. 33(e-f)) is found to decreased continuously for all MPs coupling with KF and BMJ schemes. The area averaged OLRs in R4 (Figs. 33(g-h)) has almost constant and after 0000 UTC of 11 October the OLRs is increase in the oceanic region for all MPs coupling with KF and BMJ scheme. The OLRs is found to decrease continuously and oscillatory in nature (Figs. 33(i-j)) up to 0600 UTC of 11 October after that it has increased for all MPs in combination with KF and BMJ scheme in R5. Therefore, it is apparent that OLR decreases in a region where tropical cyclone moves.

4.3.11 Ground Heat Flux (GHF)

The vertically integrated space averaged GHFs for six different MP schemes coupling with KF and BMJ schemes in R1, R2, R3, R4 and R5 are presented in Figs. 34(a-j). The space averaged GHFs are found to be oscillatory in nature and crest of oscillation has found at night time and trough at day time. The GHFs is found to be negative in R1, R2, R3, R4 and R5 during the day time at 0000 to 0900 UTC and positive during the night time at 1200 to 0000 UTC. Kessler scheme coupling with KF and BMJ schemes have been simulated minimum GHFs in R1, R2, R3, R4 and R5. The crest and trough of oscillation in R1 (Figs. 34(a-b)), R3 (Figs. 34(e-f)) and R5 (Figs. 34(i-j) is almost constant for all MP schemes in combination with KF and BMJ schemes. But the amplitude of trough is maximum in R1 and minimum in R3. The Amplitude of oscillation of GHFs has almost zero for all MPs coupling with KF and BMJ schemes in the oceanic region i.e. R4

The vertically integrated space averaged GHFs is decrease at night time and increase during day time i.e. positive and negative values is decrease at night and day respectively in R2 during the simulation time for all MPs coupling with KF and BMJ schemes. The negative GHFs at day time is increase and tends to zero at 0600 UTC of 12 October for all MPs coupling with KF and BMJ schemes.

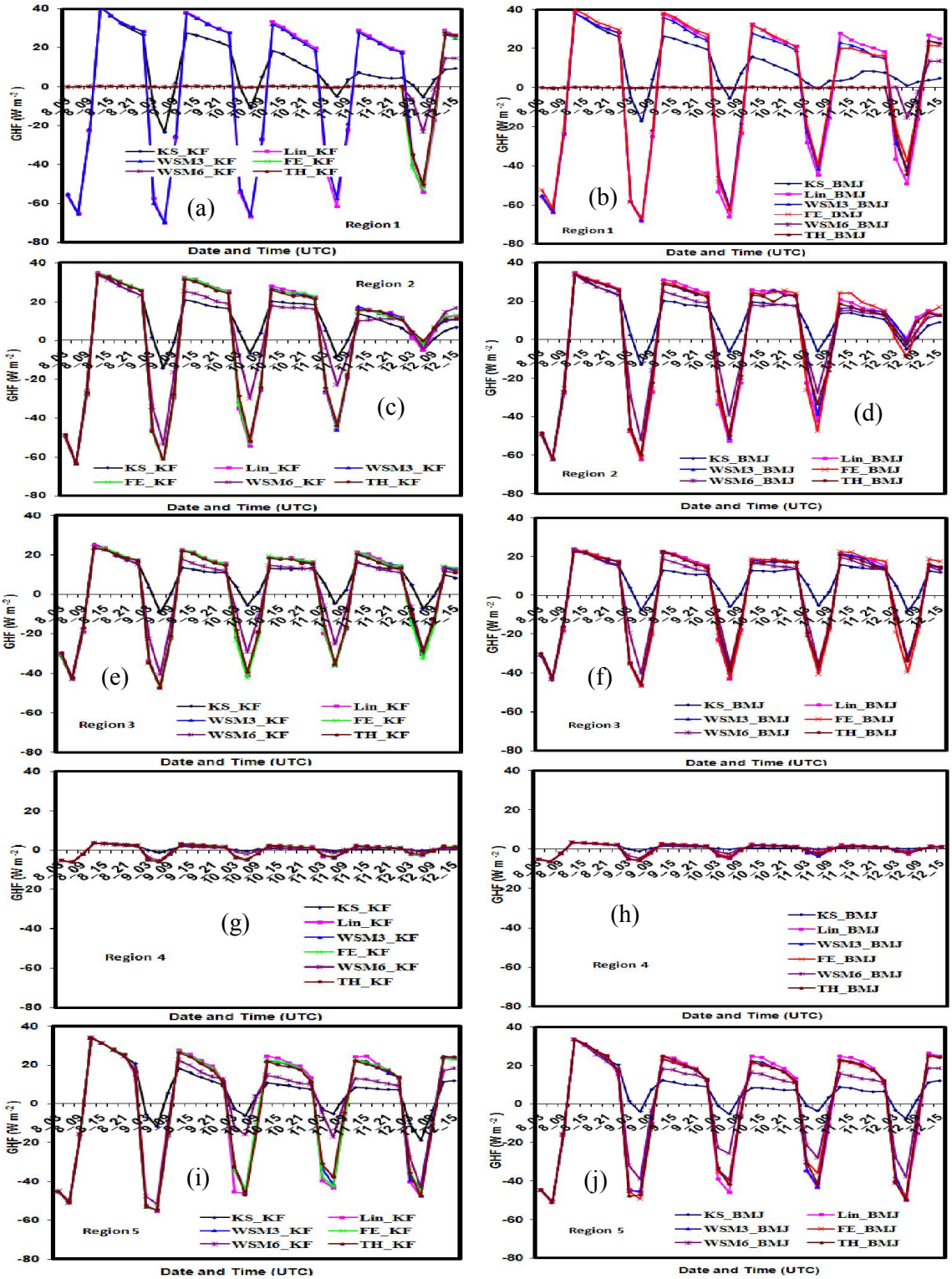

Fig. 34: Model simulated GHF of TC Hudhud for six different MP schemes at (a-b) R1, (c-d) R2, (e-f) R3, (g-h) R4 and (i-j) R5 coupling with KF and BMJ schemes respectively.

4.3. 12 Upward Heat flux (UHF)

The vertically integrated space averaged upward heat fluxes' for six different MP schemes coupling with KF and BMJ schemes in R1, R2, R3, R4 and R5 are presented in Figs. 35(a-j).Kessler scheme has simulated minimum upward heat flux out of all MP schemes in all regions except R4, but the pattern is similar. The space averaged upward heat flux is oscillatory in nature and maximum amplitude of oscillation has found at day time and minimum at night time. The crest and trough of UHF in R1 (Figs. 35 (a-b)) has almost constant for all MPs coupling with KF and BMJ schemes except Ferrier-KF, WSM6-KF, WSM6-BMJ, Thompson-KF and Thompson-BMJ.

The crest of oscillation of UHF in R2 (Figs. 35(c-d)) has almost constant and significantly higher among different regions during 9-11 October and trough of oscillation is decreasing tendency for all MPs coupling with KF and BMJ schemes at night time as the cyclone progress towards R2. At 12 October the crest and trough is also found minimum in R2 for all MPs coupling with KF and BMJ schemes. The crest is decreasing and trough is increasing continuously in R3 for all MPs coupling with KF and BMJ schemes.

The space averaged UHF is increase continuously up to 0600 UTC of 11 October and after that it is decrease for all MPs coupling with KF and BMJ schemes in the oceanic region i.e. R4 .It is also observed that crest and trough are also positive in the oceanic region. The intensity of cyclone increase due to the increase of UHF in the oceanic region. Vertically integrated space averaged upward heat flux in R5 (Fig. 35(i-j)) is almost constant for all MPs in combination with KF and BMJ schemes during the cyclonic period.

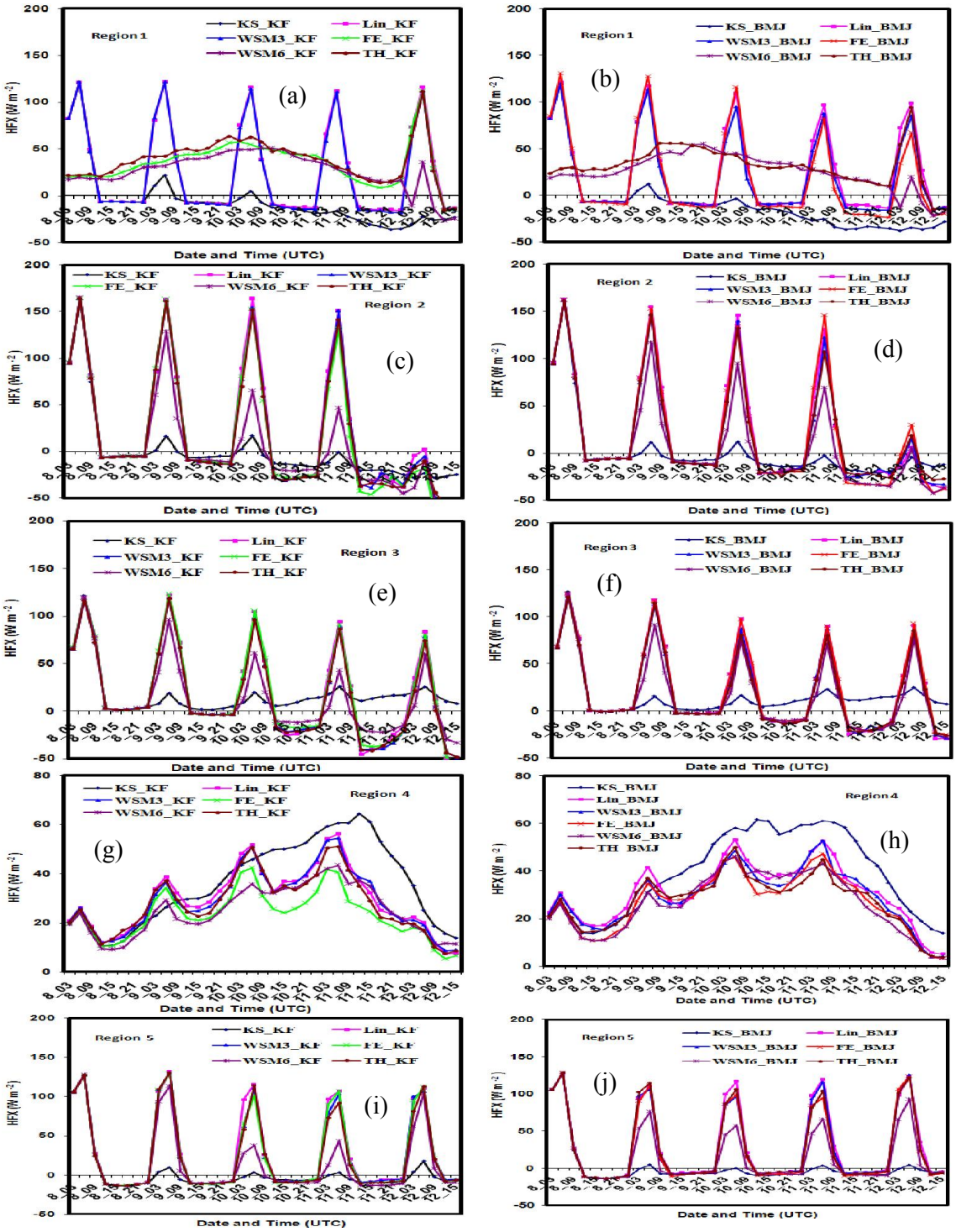

Fig. 35: Vertically integrated space averaged upward heat flux of TC Hudhud simulated for six different MPs at (a-b) R1, (c-d) R2, (e-f) R3, (g-h) R4 and (i-j) R5 coupling with KF and BMJ schemes respectively.

Chapter V

Conclusions

On the basis of the present study, the following conclusions are drawn:

In this research WRF-ARW model has been used to simulate the characteristic features of TC Roanu, Mala and Hudhud those formed in the Bay of Bengal and crossed the coasts of Bangladesh, Myanmar and Visakhapatnam of India. The NCEP FNL data is interpolated to the model horizontal and vertical grids and the model has been integrated for 96 and 72-h period for TC Roanu, Hudhud and Mala. 24 experiments have been conducted in each of TCs by using six different microphysics schemes (e.g., Kessler, Lin *et al*., WSM3-class simple ice scheme, Ferrier, WSM6-class graupel scheme and Thompson graupel) in combinations with KF and BMJ schemes with two different initial conditions. In this regard, the initial conditions of 0000 UTC of 18 and 19 May 2016 have been considered for TC Roanu, 0000 UTC of 08 and 09 October 2014 have been considered for TC Hudhud and 26 and 27 April 2006 have been considered for TC Mala. To examine the effect of energies and its fluxes for the intensity and track of tropical cyclone we have divided the model domain into five regions. The regions considered in this research are R1 (22-26^{o}N and 87-93^{o}E), R2 (18-22^{o}N and 81-85^{o}E), R3 (14-18^{o}N and 78-84^{o}E), R4 (12-22^{o}N and 85-94^{o}E) and R5 (17-22^{o}N and 94-97^{o}E).

All MPs coupling with KF and BMJ scheme with the initial conditions at 0000 UTC of 18 and 19 May 2016 have simulated much higher CSLP and 10 m level wind speed than that of IMD observed results. At the time of landfall, Lin and Ferrier schemes in combination with KF scheme and WSM6 and Thompson schemes in combination with BMJ scheme has simulated less deviated track with the initial condition of 0000 UTC of 18 May. The track deviation is increased for all MP schemes coupling with BMJ scheme with the initial condition at 0000 UTC of 19 May. KF scheme gives the less track error than that of BMJ scheme for all MPs with the initial condition at 0000 UTC of 18 May. The minimum average track error with respect to IMD observed results using Ferrier-KF and WSM6-KF combinations are 113 and 117 km respectively. The simulated intensity of TC Mala in terms of CSLP for all MP schemes in combination with KF scheme are much higher than that of BMJ scheme with the initial condition at 0000 UTC of 26 and 27 April. IMD observed intensity (954 hPa, 51.44 m s^{-1}) is much lower than that of JTWC intensity (922 hPa, 61.73 m s^{-1}) in terms of pressure fall and 10 m level sustained wind. The simulated pressure fall with

the 0000 UTC of 26 April initial condition for all MP schemes in combination with KF scheme are close to JTWC observed results but higher than that of IMD observed results. The track error with the initial condition of 27 April is very much less compared to the initial condition of 26 April. The simulated CSLP of TC Hudhud for all MPs in combination with BMJ scheme with the initial condition at 0000 UTC of 8 October are almost equal and less than that of 9 October initial condition. The simulated 10m MWS for all MPs coupling with KF scheme is almost equal and less for BMJ combination with the initial conditions at 0000 UTC of 8 and 9 October. The track error with the 0000 UTC of 9 October initial condition is very much less compared to the initial condition of 8 October. WSM6-KF combination has simulated most deviated track and Thompson-BMJ has simulated less deviated track with respect to observed track of IMD with the initial condition at 0000 UTC of 8 October. The average track error using 0000 UTC of 8 October initial condition is much higher than that of 0000 UTC of 9 October initial condition.

The vertically integrated space averaged CAPE is found to decrease continuously in a region where TC moves for all MPs in combination of KF and BMJ schemes. The TC Roanu, Hudhud and Mala moved in Bangladesh, India and Myanmar and also the cyclone moves in R1, R2 and R5 regions respectively where the cyclone moves .The TC moves in a region where the vertically integrate space averaged CIN is almost constant and towards zero. The TC Roanu, TC Hudhud and TC Mala moves in R1, R2 and R5 where CIN is decreases and tends to zero and in other regions the CIN has found to increase. The TC moved in a direction where the simulated DLHF has found to decrease and reached minimum. The DLHF has found to decrease for TC Roanu in R1 and Mala in R5 at the time of landfall whereas in case of TC Hudhud is increase in R2. It has increasing tendency or almost constant in other regions for each of TCs, where TC could not move. The cyclone moves in a direction where the DSHF is decreases in R1 for TC Roanu, in R5 for TC Mala and in R2 for TC Hudhud. In other regions DSHF has found almost constant for all the cyclones. The cyclone moves in a direction where the QFX is increases in R1 for TC Roanu, in R5 for TC Mala and in R2 for TC Hudhud. In other regions DSHF has found almost constant for all the cyclones. The TC moves in a region where the OLR has found to decrease for TC Roanu in R1, for TC Mala in R5 and TC Hudhud in R2. In other regions DSHF has found almost constant for all the cyclones. The upward heat flux and ground heat flux is decreases in a region where the TC Roanu in R1, TC Mala in R5 and TC Hudhud in R2 was crosses.

Reference

Andreas E. L., C. A. Paulson, R.W. Lindsay and J. A. Businger, 1979: The turbulent heat flux from arctic leads. Boundary Layer Meteorology, 17, 57-91.

Arakawa, A.; V. R. Lamb, 1977: Computational design of the basic dynamical processes of the UCLA general circulation mode, Methods of Computational Physics, New York: Academic Press, 17, 173–265.

Bianco, L., J.-W. Bao, C. W. Fairall, and S. A. Michelson, 2011: Impact of sea-spray on the atmospheric surface layer. Boundary Layer Meteor., 140, 361–381.

Black, P. G., 1983: Ocean temperature changes induced by tropical cyclones, Ph. D. dissertation, Pennsylvania State University, pp-278.

Bogner, P. B., G. M. Barnes, and J. L. Franklin, 1999: Conditional Instability and Shear for Six Hurricanes over the Atlantic Ocean. Amer. Meteor. Soc., 15, 192-207.

Camargo S. J., A. W. Robertson, S. J. Gaffney, P. Smyth and M. Ghil, 2007: Cluster Analysis of Typhoon Tracks. Part II: Large-Scale Circulation and ENSO. J. Climate., 20, 3654-3676.

Chang, S. W., 1979: The response of an axisymmetric model tropical cyclone to local variations of sea surface temperature. Mon. Wea. Rev., 107, 662–666.

Chang, S.W., and R.A. Anthes, 1978: Numerical simulation of the ocean's nonlinear, baroclinic response to translating hurricanes. J. Phys. Oceanogr., 8, 468-480.

Chen, S. H., and W. Y. Sun, 2002: An explicit one-dimensional time-dependent tilting cloud model. J. Atmos. Sci. 61, 23, 2797–2816.

Choi, K. S., and I. J. Moon, 2012: Changes in tropical cyclone activity that has affected Korea since 1999. Nat Hazards, 62, 971–989.

Choi, K. S., and H. Byun, 2010: Possible relationship between western North Pacific tropical cyclone activity and Arctic Oscillation, Theor. Appl. Climatol., 100, 261-274.

Colby, Jr., P. Frank 1984: Convective Inhibition as a Predictor of Convection during ave-sesame II. Mon. Wea. Rev. 112, 11, 2239–2252.

Colon-Pagan, I. C., 2009: Orographic Effects on Rainfall Induced by the Passage of Tropical Cyclones over Mountainous Islands: Part I: The Effect of Cloud Microphysics. SOARC, 1-24.

Davis, C. A., and L. F. Bosart, 2002: Numerical simulations of the genesis of Hurricane Diana (1984). Part II. Sensitivity of track and intensity prediction, Mon. Wea. Rev., 130, 1100–1124.

Deardorff, J. W., 1972: Parameterization of the planetary boundary layer for use in general circulation models, Mon. Wea. Rev., 100, 93–106.

DeCosmo, J. and E.L., Andreas, 2002: The signature of sea spray in the HEXOS turbulent heat flux data. Boundary-Layer Meteorol., 103, 303-333.

DeCosmo, J., K. B. Katsaros, S.D. Smith, R. J. Anderson, W. A. Oost, K. Bumke, and H. Chadwick, 1996: Air-sea exchange of water vapor and sensible heat: The Humidity Exchange over the Sea (HEXOS) results. Journal of Geophysical Research 101, 0148-0227.

Dudhia, J., 1989: Numerical study of convection observed during the winter monsoon experiment using mesoscale two-dimensional models, J. Atmos. Sci., 46, 3077-3107.

Ek, M. A. A., K. E. Mitchell, Y. Lin, E. Rogers, P. Grundmann, V. Koren, G. Gayno, and J. D. Tarpley, 2003: Implementation of Noah land surface model advances in the National Centers for Environmental Prediction operational mesoscale Eta model, Journal of Geophysical Research, 108, D22, 8851.

Emanuel, K.A., 1983: On assessing local Condition Symmetric in stability from atmospheric sounding Mon .Web. Rev., 111, 2016-2033.

Evans J. L., and J. J. Waters, 2012: Simulated Relationships between Sea Surface Temperatures and Tropical Convection in Climate Models and Their Implications for Tropical Cyclone Activity. J. Climate, 25, 7884–7895.

Fairal, C. W., E. F. Bradley, J. S. Godfrey, G. A. Wick, and J. B. Edson, 1996: Cool-skin and warm-layer effects on sea surface temperature. Journal of Geophysical Research, 101, 1295-1308.

Fang, J., J. P. Tang, and R. S. Wu, 2009: The effect of surface friction on the development of tropical cyclones. Adv. Atmos. Sci., 26, 6, 1146–1156.

Fovell, R.G. and Su, H., 2007: Impact of cloud microphysics on hurricane track forecasts, Geophysical Research Letters 34, 0094-8276.

Fritsch, J. M. and C. F., Chappell, 1980: Numerical Prediction of Convective Driven Mesoscale Pressure Systems, Part I: Convective Parameterization, J. Atoms. Sci. 37, 1722- 1733

Hong S.Y., Y. Noh and J., Dudhia 2006: A new vertical diffusion package with an explicit treatment of entrainment processes. Mon. Wea. Rev., 134, 2318-2341.

Hong, S. Y., and J. O. J. Lim, 2006: The WRF Single Moment 6-Class Microphysics Scheme (WSM6), J Korean Meteorol. Soc., 42, 2, 129-151.

Hong, S. Y., J. Dudhia and S. H., Chen, 2004: A Revised Approach to Ice Microphysical Processes for the Bulk Parameterization of Clouds and Precipitation, Mon. Wea. Rev., 132, 103-120.

Hong, Song-You, and Hua-Lu Pan, 1996: Nonlocal boundary layer vertical diffusion in a medium-range forecast model, Monthly weather review 124, 10, 2322-2339.

Janjic, Z. I., 1994: The step-mountain Eta coordinate model: Further developments of the convection, viscous sub layer, and turbulence closure schemes. Mon. Wea. Rev., 122, 927–945.

Janjic, Z. I., 2000: Comments on Development and Evaluation of a Convection Scheme for Use in Climate Models. J. Atmos. Sci., 57, 3686.

Kain J. S. and J. M., Fritsch 1990: A one-dimensional entraining/detraining plume model and its application in convective parameterization. J. Atmos. Sci., 47, 2684-2702.

Kain J. S., 2004: The Kain-Fritsch convective parameterization: An update. J. Appl. Meteor., 43, 170-181.

Kain, J. S., and J. M., Fritsch, 1993: Convective parameterization for mesoscale models: the Kain-Fritsch scheme, the representation of cumulus convection in numerical models, Meteo. Monogr 46, Amer. Meteor. Soc., 165–170.

Kessler, E., 1969: On the distribution and continuity of water substance on atmospheric circulation. Meteorol. Monogr., 10, 32, 84.

Lin, Y.L., R. D. Farley, and H. D., Orville, 1983: Bulk parameterization of the snow field in a cloud model, J. Climate Appl. Meteor., 22, 1065-1092.

Mlawer, E. J., S. J. Tubman, P. D. Brown, M. J. Lacono, and S. A. Clough, 1997: Radiative transfer for inhomogeneous atmosphere: RRTM, a validated correlated-k model for the longwave, J. Geophys. Res., 102(D14), 16663-16682.

Molinari, J., and D. Vollaro, 2009: notes and correspondence Distribution of Helicity, CAPE, and Shear in Tropical Cyclones. J. Atmos. Sci., 67, 274-284.

Nolan, D. S., E. D. Rappina, and K. A. Emanuel, 2007: Tropical cyclogenesis sensitivity to environmental parameters in radiative–convective equilibrium. Q. J. R. Meteorol. Soc., 133, 2085–2107.

Pattanaik D. R., and Y. V. Rama Rao, 2009: Track prediction of very severe cyclone 'Nargis' using high resolution weather research forecasting (WRF) model J. Earth Syst. Sci. 118, 4, 309–329.

Pattnaik, S. and T. N. Krishnamurti, 2007a: Impact of cloud microphysical processes on hurricane intensity, part 1: Control run, Meteorol. Atmos. Phys., 97, 117–125,

Pattnaik, S. and T. N. Krishnamurti., 2007b: Impact of cloud microphysical processes on hurricane intensity, part 2: Sensitivity experiments, Meteorol. Atmos. Phys., 97, 127–147.

Pleim, J., 2007: A combined local and non-local closure model for the atmospheric boundary layer. Part II: Application and evaluation in a mesoscale meteorological model, J. Applied Meteor. Climatology, 46, 1396–1409.

Raju, P. V. S., J. Potty, U. C. Mohanty, 2011: Sensitivity of physical parameterizations on prediction of tropical cyclone Nargis over the Bay of Bengal using WRF Model, Meteorol. Atmos. Phys. 113, 125-137.

Rosenfeld D., A. Khain, B. Lynn and W. L. Woodley, 2007: Simulation of hurricane response to suppression of warm rain by sub micron aerosols Atmos chem Phys 7, 3411-3424.

Shin, H. H., and S. Y., Hong, 2011: Inter-comparison of Planetary Boundary-Layer Parametrizations in the WRF Model for a Single Day from CASES-99, Boundary-Layer Meteorol, 139, 261–281.

Smith, R. K., and M. T. Montgomery, 2012: A Observations of the convective environment in developing and non-developing tropical disturbances. Q. J. R. Meteorol. Soc., 138, 1721-1739.

Sobel, A. H., and S. J. Camargo, 2005: Influence of Western North Pacific Tropical Cyclones on Their Large-Scale Environment. J. Atmos. Sci., 62, 3396-3407.

Tao, W. K., J. Simpson, S. Lang, M. McCumber, R. Adler and R. Penc, 1990: An algorithm to estimate the heating budget from vertical hydrometeor profiles. J. Appl. Meteor., 29, 1232-1244.

Tarakanov, G.G., 1982: Tropical Meteorology, Mir Publishers, Moscow, 206pp.

Thompson, A. M., R. B., Chatfield, H. G. Hguan, J., and Smit, 2007: Mechanisms for the intrapersonal variability of ozone during the India winter monsoon, J. Geophys. Res., 112, D10303.

Tuleya, R. E., and Y. Kurihara, 1982: A note on the sea surface temperature sensitivity of a numerical model of tropical storm genesis. Mon. Wea. Rev., 110, 2063–2068.

Wang, Y., 2001: An explicit simulation of tropical cyclones with a triply nested movable mesh primitive equation model—TCM3. Part I: Description of the model and control experiment. Mon. Wea. Rev., 129, 1270–1294.

Wang, Y., 2002: An explicit simulation of tropical cyclones with a triply nested movable mesh primitive equations model-TCM3. Part II: Model refinements and sensitivity to cloud microphysics parameterization. Mon. Wea. Rev., 130, 3022-3036.

Willoughby, H. J., S. Lord, and J. Piotrowicz, 1984: Hurricane structure and evolution as simulated by an axisymmetric non hydrostatic numerical model. J. Atmos. Sci., 41, 1169–1186.

Xu, J., and Y. Wang, 2010: Sensitivity of Tropical Cyclone Inner-Core Size and Intensity to the Radial Distribution of Surface Entropy Flux Journal of the Atmospheric Sciences. j. Atmos. Sci., 67, 6, 1831-1852.

Yuan J. P., and J. Cao, 2013: North Indian Ocean tropical cyclone activities influenced by the Indian Ocean Dipole mode. Science China: Earth Sciences 56: 855–865, doi: 10.1007/s11430-012-4559-0.

Zhu Z. and H. Zhang, 2006: Spatial sampling designs under in fill Asymptotic Framework a Environmetrics, 17, 323-337.

Conference Presentation

1) **Kaniz Fatema, H. R. Khan, M. M. Alam, 2016:** Effect of Upward Fluxes of different Microphysics on the Track of Tropical Cyclone in the Bay of Bengal, Presented at International Conference on Physics-2016, Bangladesh Physical Society, Dhaka, 10-12 March 2016.
2) **Kaniz Fatema and M. M. Alam 2016**: Effect of Upward Fluxes of Different Microphysics on the Track of Tropical Cyclone in the Bay of Bengal, Presented on the Conference on Weather Forecasting and Advances in Physics: Bangladesh Perspective, Khulna University of Engineering & Technology, Khulna, 20 May 2016.
3) **Kaniz Fatema and M. M. Alam 2017:** Impact of Energy Fluxes of different MP Schemes on the Track and Intensity of TC ROANU in the Bay of Bengal, Presented at national Conference on Physics-2017, Bangladesh Physical Society, Dhaka, 5-7 January 2017.